GROWTH, CHARACTERIZATION AND THERMAL STABILITY OF UNDOPED AND IN-SITU DOPED SILICON-GERMANIUM HETEROEPITAXIAL LAYERS

by

Syun-Ming Jang

B. S., National Tsing Hua University
(1985)

M.S., National Tsing Hua University
(1987)

Submitted to the Department of
Materials Science and Engineering
in Partial Fulfillment of the Requirements
For the Degree of

DOCTOR OF PHILOSOPHY

at the

MASSACHUSETTS INSTITUTE OF TECHNOLOGY

June 1993

© Massachusetts Institute of Technology 1993

Signature of Author__________________________

Department of Materials Science and Engineering
April 30, 1993

Certified by____

Rafael Reif, Thesis Supervisor
Professor, Department of Electrical Engineering and Computer Science
Director, Microsystems Technology Laboratories

Accepted by____

Linn W. Hobbs
John F. Elliott Professor of Materials
Chair, Departmental Committee on Graduate Students

ARCHIVES
MASSACHUSETTS INSTITUTE
OF TECHNOLOGY

JUL 30 1993

LIBRARIES

GROWTH, CHARACTERIZATION, AND THERMAL STABILITY OF UNDOPED AND IN-SITU DOPED SILICON-GERMANIUM HETEROEPITAXIAL LAYERS

by
Syun-Ming Jang
Submitted to the Department of Materials Science and Engineering
on April 30, 1993, in partial fulfillment of the requirements
for the degree of Doctor of Philosophy in Materials Science and Engineering

Abstract

This thesis work involves the deposition and characterization of undoped and *in situ* doped $Si_{1-x}Ge_x$ layers as well as the studies of $Si_{1-x}Ge_x$ growth kinetics and thermal stability.

A procedure has been developed and optimized for the deposition of high quality heteroepitaxial $Si_{1-x}Ge_x$ layers at temperatures from 570 to 750°C using a very low pressure (3 – 10 mTorr) chemical vapor deposition (VLPCVD) reactor with silane and germane as source gases with or without plasma enhancement. The surface morphology, crystalline perfection and purity of the deposited films were characterized by Nomarski microscopy, ion channeling/Rutherford backscattering spectrometry, scanning electron microscopy, transmission electron microscopy, double-crystal X-ray diffractometry, Raman scattering spectroscopy, and secondary ion mass spectrometry. The temperature and germanium dependencies of $Si_{1-x}Ge_x$ growth modes, i.e., two- and three-dimensional growth, at temperatures 570 – 750°C were investigated, and the range for smooth morphology has been mapped out for VLPCVD $Si_{1-x}Ge_x$ heteroepitaxy. It was demonstrated that high quality strained layers of $Si_{1-x}Ge_x$, including single layers, sandwiched layers, and multiple layers, with germanium contents of ≤ 0.25 could be grown on non-patterned and oxide patterned silicon substrates at temperatures ≥ 620°C. At deposition temperatures below 620°C, the film quality is severely degraded by carbon and oxygen contamination. The examination of growth mode and film purity indicates the fundamental limits of low-temperature $Si_{1-x}Ge_x$ heteroepitaxy in VLPCVD.

A sublinear relationship was observed between germanium incorporation and germane fraction. The amount of incorporated germanium slightly increases with increasing temperature, but decreases by raising the flow rates of source gases and hydrogen carrier gas. The $Si_{1-x}Ge_x$ deposition rate measured in the temperature range from 570 – 700°C exhibits different dependencies on germanium content at different temperatures. The growth rate decreases with increasing germanium content at 700°C, but increases monotonically with germanium at 570°C; exhibiting a peak in growth rate at intermediate temperatures. The measured activation

energy in $Si_{1-x}Ge_x$ deposition rate was found to decrease by the addition of germanium, suggesting that the rate-limiting step was modified by germanium. By varying temperature and gas flow rates, we have examined the $Si_{1-x}Ge_x$ deposition process, and a model is proposed to account for the observed growth behaviors.

In situ doping of $Si_{1-x}Ge_x$ layers was carried out by using diborane, arsine, and phosphine as dopant sources. Very high boron (2×10^{20} cm^{-3}) and arsenic (5×10^{19} cm^{-3}) concentrations have been achieved in $Si_{0.87}Ge_{0.13}$ using 1000 ppm diborane and arsine without degrading film quality. The amount of boron atoms incorporated into $Si_{1-x}Ge_x$ layer is independent of germanium composition. No change in $Si_{1-x}Ge_x$ growth rate due to boron incorporation was measured. It was observed that, for n-type doping, the germanium incorporation is independent of phosphine. However, the phosphorus incorporation appears to be enhanced by the addition of germanium. Moreover, a dramatic improvement of phosphorus depth profile was observed and the magnitude of growth rate inhibition due to n-type doping was found to decrease with increasing germanium content. The observed germanium enhanced phosphorus doping process is thought to be a result of reduced surface passivation of phosphorus dopants. We speculate that germanium might have two important effects on the doping process: the disruption of P-P dimerization and the enhancement of phosphorus desorption. A model is proposed to explain the experimental data.

The critical thickness of VLPCVD $Si_{1-x}Ge_x$ strained layers grown at 750 and 620°C has been measured, and the thermal stability of $Si_{1-x}Ge_x$ strained layers was investigated. We have measured the dislocation density in uncapped 1240Å-thick $Si_{0.92}Ge_{0.08}$ and 600Å-thick $Si_{0.87}Ge_{0.13}$ after 30 min annealing at 750 – 950°C and found that the misfit dislocations in these structures increased rapidly at 750 – 800°C and became saturated at temperatures of 850°C – 950°C. Strain relief in annealed ~1400Å Si/520-700Å $Si_{1-x}Ge_x$/Si heterostructures (x=0.09 – 0.16) has been quantitatively measured and it was found that the strain relaxed gradually at temperatures < 950°C but relaxed rapidly at temperatures > 950°C, showing a transition point and different mechanisms in the relaxation process. The possible mechanisms, involving the generation of misfit dislocation and Si-Ge interdiffusion, have been studied to explain the relaxation behaviors. Finally, a thermal budget has been mapped out for strained-layer growth (temperature ≤ 750°C and time < 10 min) and for thermal annealing (temperature ≥ 750°C and time = 30 min) without strain relaxation.

Thesis Supervisor: Professor L. Rafael Reif
Title: Professor of Electrical Engineering
Director, Microsystems Technology Laboratories

Acknowledgments

Many people have made great contributions to this thesis. The foremost, is my advisor, Prof. Rafael Reif, who provided a creative, interdisciplinary atmosphere and offered me continued guidance, encouragement, and support. He has my greatest admiration as a person of understanding, patience, insight, and motivation.

I would like to thank IBM and SRC for providing funding for this work. I am grateful to Prof. Harry Tuller and Prof. Lionel Kimerling for reviewing this thesis and providing very helpful suggestions.

I thank Dr. Curtis Tsai, Hyoun-Woo Kim, Julie Tsai, Dr. Noboro Nakano, Ken Liao, and Dr. Toshihiro Miyata for wonderful collaborations on the $Si_{1-x}Ge_x$ projects. I give my appreciation to Dr. Tsai for training me on the VLPCVD reactor, to Ken Liao for providing mask, to Hyoun-Woo Kim and Dr. Miyata for help with DCD measurement, to Dr. Nakano for providing Raman data, and to Julie Tsai for proof-reading part of my writings. Besides, they all have done great job at keeping the reactor working.

My gratitude also goes to Dr. Tri-Rung Yew for teaching me XTEM sample preparation, to Dr. Richard Singer for training me on DCD, to Mr. Mike Frongillo for training me on TEM and ion mill, and to Mr. John Chervinski for training me on RBS at Harvard. I am grateful to the staff in Microsystems Technology Laboratories: Octavio Hurtado, Paul Mcgrath, and Joe DiMaria for their helps with the reactor, Paul Tierney and Jim Carter for training me on SEM, and the rest of the staff for training me on the processing facilities. I also like to thank Fuzhong Yu, Zhen-Hong Zhou, Isabel Yang, Dr. Zhizen Ye, Danny Reif, Yih-Feng Chyan, and Dr. Shoushan Fan for their support and discussions. A very special thank-you goes to Carolyn Zaccaria for great help when I needed. Assistances from Sam Crooks, Kate Peterson and Christian Gordy for paper work in the research project are highly appreciated. I also thank the friendship from Lung-Han Peng, Vei-Han Chan, Paul Yu, Charles Hsu, Chock Gan, Albert Hu, and Andy Guo, among others associated with MTL.

Many people in my country deserve my appreciation. I would like to thank my master thesis advisor, Prof. Sanboh Lee, who has encouraged me to come to the U.S. to pursue my Ph.D. degree. My family has provided love and emotional support throughout my life. They always do their best from far away. I also appreciate the encouragement and devotion from my wife's family. Finally, I specially thank my wife, Chia-Ming Chu, for her love, support, and consideration. Without her this work is almost impossible. I also thank my lovable daughter, Erica Jang, who has joined us for sixteen months and has been bringing the most unforgettable experiences to my life in MIT. She is a chapter in this work.

Contents

Title 0

Abstract 1

Acknowledgements 2

Table of Contents 3

Acronym in This Thesis 14

1 Introduction 15
- 1.1 Introduction 15
- 1.2 Literature Review 18
  - 1.2.1 Growth Principles 18
  - 1.2.2 CVD Techniques for $Si_{1-x}Ge_x$ Deposition 23
  - 1.2.3 Thermal Stability 30
  - 1.2.4 $Si_{1-x}Ge_x$ Heteroepitaxy Applications 32
- 1.3 Goal of This Thesis 41

2 Experimental 43
- 2.1 Introduction 43
- 2.2 $Si_{1-x}Ge_x$ Heteroepitaxy and Annealing 43
  - 2.2.1 Wafer Patterning 43
  - 2.2.2 Ex-situ Surface Cleaning 45
  - 2.2.3 In-Situ Surface Cleaning 45
  - 2.2.4 Very Low Pressure Chemical Vapor Deposition 47
  - 2.2.5 Thermal Annealing 47
- 2.3 Materials Characterization 48
  - 2.3.1 Nomarski Optical Microscopy and Schimmel Etch 48
  - 2.3.2 Scanning Electron Microscopy 49

2.3.3 Ion Channeling/Rutherford Backscattering Spectrometry . . 49
2.3.4 Secondary Ion Mass Spectrometry 50
2.3.5 Transmission Electron Microscopy 50
2.3.6 Double-Crystal X-ray Diffractometry 51
2.3.7 Raman Scattering Spectrometry 51

3 VLPCVD/PECVD of $Si_{1-x}Ge_x$ at 750°C **52**
3.1 Introduction 52
3.2 Experiments 53
3.3 Results 55
3.3.1 VLPCVD 55
3.3.2 PECVD 63
3.4 Discussion 66
3.5 Conclusion 70

4 VLPCVD of $Si_{1-x}Ge_x$ at 570 – 700°C **71**
4.1 Introduction 71
4.2 Experiments 72
4.3 Results 74
4.3.1 $Si_{1-x}Ge_x$ Deposition on Blanket Wafers 74
4.3.2 $Si_{1-x}Ge_x$ Deposition on Patterned Wafers 79
4.4 Discussion 83
4.4.1 $Si_{1-x}Ge_x$ Deposition on Blanket Wafers 83
4.4.2 $Si_{1-x}Ge_x$ Deposition on Patterned Wafers 89
4.5 Conclusion 91

5 Growth Kinetics of $Si_{1-x}Ge_x$ **93**
5.1 Introduction 93
5.2 Experiments 95
5.3 Results 97
5.3.1 Germanium Incorporation 97
5.3.2 $Si_{1-x}Ge_x$ Growth Rate 99
5.4 Discussion 103
5.4.1 Kinetic Model 103
5.4.2 Germanium Incorporation 106
5.4.3 $Si_{1-x}Ge_x$ Growth Rate 108
5.5 Conclusion 115

6 In-Situ Doping of $Si_{1-x}Ge_x$ **117**

6.1 Introduction 117
6.2 Experiments 118
6.3 Results 120
6.4 Discussion 129
6.4.1 Boron Doping 129
6.4.2 Arsenic and Phosphorus Doping 131
6.5 Conclusion 141

7 Critical Thickness and Thermal Stability of $Si_{1-x}Ge_x$ 143
7.1 Introduction 143
7.2 Experiments 144
7.3 Critical Thickness of $Si_{1-x}Ge_x$ 145
7.4 Thermal Stability of $Si_{1-x}Ge_x$ 153
7.4.1 Misfit Dislocation 153
7.4.2 Ge Diffusion 168
7.4.3 Dopant Effects 172
7.5 Thermal Budget for VLPCVD $Si_{1-x}Ge_x$ Deposition and Annealing . 174
7.6 Conclusion 175

8 Summary and Suggestions 177
8.1 Summary 177
8.1.1 Deposition of $Si_{1-x}Ge_x$ 177
8.1.2 Growth Kinetics of $Si_{1-x}Ge_x$ 178
8.1.3 In-Situ Doping of $Si_{1-x}Ge_x$ 179
8.1.4 Thermal Stability of $Si_{1-x}Ge_x$ 180
8.2 Suggestions 181
8.2.1 Deposition of $Si_{1-x}Ge_x$ 181
8.2.2 Growth Kinetics of $Si_{1-x}Ge_x$ 182
8.2.3 In-Situ Doping of $Si_{1-x}Ge_x$ 183
8.2.4 Thermal Stability of $Si_{1-x}Ge_x$ 184

Bibliography 186

Appendix A 197

Appendix B 198

List of Figures

1.1 Band gap of semiconducting materials as a function of lattice constant [4]. 16
1.2 Possible growth modes of $Si_{1-x}Ge_x$ heteroepitaxial growth on silicon 19
1.3 Schematic illustration of epitaxial strained layer and unstrained layer. 20
1.4 Plot of $Si_{1-x}Ge_x$ growth mode with respect to Ge composition and growth temperature [13]. 21
1.5 Open circles and solid line are experimental single layer critical thicknesses and their empirical expression reported by People and Bean [25]. Lowered dashed curve - van der Merwe (theory); middle dot-dashed - Matthews and Blakeslee (theory). 22
1.6 Schematic of the Stanford LRP reactor [39]. 25
1.7 Schematic of the AT&T RTCVD reactor [42]. 26
1.8 Schematic of the IBM UHVCVD reactor [43]. 27
1.9 Schematic of the ASM Epsilon One APCVD reactor [44]. 28
1.10 Forces on electrons and holes. In a uniform-gap semiconductor (a) the two forces are equal and opposite to each other, and equal to electrostatic force. In a graded-gap structure (b), the forces in electrons and holes may be in the same direction [66]. 34
1.11 The band diagrams of npn homojunction and heterojunction transistors [66]. 35
1.12 Band alignments for (a) $Si_{0.80}Ge_{0.20}/Si$ heterojunctions on (001) Si substrates, (b) $Si_{0.50}Ge_{0.50}/Si$ on (001)-$Si_{0.75}Ge_{0.25}$, and (c) $Si_{0.50}Ge_{0.50}/Si$ heterojunctions on (001)-Si [7]. 39
1.13 Modulation-doping of a $Si_{1-x}Ge_x/Si$ heterostructure grown on (100) Si. (a) n-type modulation doping requires donor localization in $Si_{1-x}Ge_x$, and a two-dimensional electron gas is formed in Si. (b) p-type modulation doping requires acceptor localization in Si, and the two-dimensional hole gas is formed in $Si_{1-x}Ge_x$ [75]. 40

2.1 Schematic of VLPCVD system. 46

3.1 XTEM bright field images of 750°C smooth and commensurate $Si_{1-x}Ge_x$ films formed by two-dimensional growth: (a) x=0.08 and (b) x=0.13. 57
3.2 XTEM bright field images of 750°C rough $Si_{1-x}Ge_x$ islands formed by three-dimensional growth: (a) x=0.15 and (b) x=0.35, measured. 58
3.3 The measured ratios of height to radius of three-dimensional $Si_{1-x}Ge_x$ islands. The actual value of islanding height is also shown. 59
3.4 Germanium content as a function of GeH_4:SiH_4 input ratio by VLPCVD. 60
3.5 SIMS depth profile of germanium incorporation: (a) without growth interruption (b) with growth interruption between the deposition of $Si_{1-x}Ge_x$ and Si capped layer. 61
3.6 $Si_{1-x}Ge_x$ growth rate as a function of Ge content by VLPCVD. . . 63
3.7 XTEM bright field images of 750°C $Si_{1-x}Ge_x$ grown by PECVD: (a) x=0.16 (two-dimensional growth) and (b) x=0.35 (three-dimensional growth). 64
3.8 Ge content as a function of GeH_4:SiH_4input ratio by VLPCVD and PECVD. SiH_4 = 20 sccm. 65
3.9 $Si_{1-x}Ge_x$ growth rate as a function of Ge content by VLPCVD and PECVD. SiH_4 = 20 sccm. 65

4.1 XTEM micrographs of (a) Si/$Si_{0.87}Ge_{0.13}$/Si and (b) Si/$Si_{0.84}Ge_{0.16}$/Si deposited at 620°C. SiH_4=20sccm, H_2=80scm, and GeH_4=0.75 and 1.00 sccm, respectively, for (a) and (b). 75
4.2 (a) XTEM and (b) SEM micrographes of Si/$Si_{0.81}Ge_{0.19}$/Si deposited at 570°C. SiH_4=20sccm, H_2=80scm, and GeH_4=1.00 sccm. 76
4.3 (a) XTEM and (b) SEM micrographs of $Si_{0.84}Ge_{0.26}$ deposited on Si substrate. 78
4.4 Ge content as a function of GeH_4/SiH_4 ratio at 620 and 570°C measured from Si/$Si_{1-x}Ge_x$/Si sandwiched structures. 79
4.5 Measured thickness of $Si_{1-x}Ge_x$ deposited at 620°C and at 570 °C for various deposition time. In all cases, $Si_{1-x}Ge_x$ was capped with a Si film. Also indicated is the misfit-dislocation density in Si/$Si_{1-x}Ge_x$/Si (x=0.156) structures with varied $Si_{1-x}Ge_x$ thickness observed by Normaski micrograph after 1 min Schimmel etching. . . 80
4.6 $Si_{1-x}Ge_x$ epitaxial growth rate as a function of Ge composition at 620 and 570°C. 80
4.7 XTEM micrographs of $Si_{1-x}Ge_x$ layer grown on LOCOS patterned substrates: (a) deposition time = 5 min, (b) deposition time = 30 min. 81

4.8 XTEM micrographs of $Si_{1-x}Ge_x$ layer grown on plasma-etch oxide patterned substrates: (a) deposition time = 5 min, (b) deposition time = 30 min. 82
4.9 XTEM micrographs of $Si_{1-x}Ge_x$/Si multilayer structures grown on oxide pattered substrates prepared by chemical etching. $Si_{1-x}Ge_x$ and Si layers were grown on 10 × 10 μm and 5 × 5 mm as indicated. 84
4.10 SIMS depth profile of 625°C multilayer structure. All layers had a 5 min deposition time. 85
4.11 (a) SIMS data of oxygen and carbon recontamination at the interface of $Si_{1-x}Ge_x$ and Si buffer layer when system was cooled from 775°C, at which Si buffer layer was deposited, to the $Si_{1-x}Ge_x$ growth temperatures (570 - 700°C). Also exhibited is the system cooling times. (b) Oxygen and carbon concentrations in VLPCVD Si and $Si_{1-x}Ge_x$ films and in RTCVD Si films grown at 550 - 800°C. In both cases, SiH_4 and GeH_4 were used as source gases in H_2 carrier gas. 86

5.1 Germanium composition in $Si_{1-x}Ge_x$ as a function of deposition temperature; silane flow = 40 sccm and hydrogen flow = 80 sccm. . 97
5.2 Atomic germanium fraction as a function of hydrogen flow rate at 620°C; silane flow = 40 sccm. 98
5.3 Atomic germanium fraction as a function of silane flow rate at 620°C; no hydrogen flow. 98
5.4 Growth rate of $Si_{1-x}Ge_x$ measured at different germanium content; silane flow = 40 sccm, hydrogen flow = 80 sccm 99
5.5 Arrhenius plots for the growth rate of $Si_{1-x}Ge_x$ shown in Fig. x in the temperature range of 570 - 700°C. 100
5.6 Measured $Si_{1-x}Ge_x$ growth rate expressed as a function of germanium incorporation. Layers were grown at 620°C at different deposition pressures with silane flow rate = 20, 40, 50, 60, and 80 sccm; no hydrogen flow. 100
5.7 $Si_{1-x}Ge_x$ growth rate versus hydrogen flow rate at 620°C. silane flow rate was kept at 40 sccm. The germanium content that gives maximum growth rate for varied hydrogen flow is also indicated. . . 101
5.8 Comparisons of germanium incorporation versus germane fraction for different reactors. 106
5.9 $Si_{1-x}Ge_x$ growth rate expressed as a function of silane flow rate. Growth rates for $x = 0$ and 0.05 were fit using equations (19) and (23), and equation (29) was used for $x = 0.15$ and 0.20. 113

5.10 Germanium dependency of the extracted $k_{2,Si}k_{1f,Si}/(k_{1r,Si}+k_{2,Si})$ from Fig. 9. 114

6.1 Cross-sectional transmission electron microscopy images of Si/boron-doped $Si_{1-x}Ge_x$/Si heterostructures with (a) $x = 0.13$, 25 ppm diborane in silane, and (b) $x = 0.13$, 1000 ppm diborane in silane; silane flow = 20 sccm, germane flow = 0.75 sccm, and hydrogen flow = 80 sccm. 121
6.2 Cross-sectional transmission electron microscopy images of Si/arsenic-doped $Si_{0.87}Ge_{0.13}$/Si heterostructures with (a) 100 ppm arsine in silane, and (b) 1000 ppm arsine in silane; silane flow = 20 sccm, germane flow = 0.75 sccm, and hydrogen flow = 80 sccm. 122
6.3 Secondary ion mass spectrometry depth profiles of dopant and germanium in (a) Si/boron-doped $Si_{0.89}Ge_{0.13}$/Si shown in Fig. 6.1 (b), and (b) Si/arsenic-doped $Si_{0.89}Ge_{0.13}$/Si shown in Fig. 6.2 (b). . . . 123
6.4 Cross-sectional transmission electron microscopy images of phosphorus-doped $Si_{0.88}Ge_{0.12}$/Si multilayer structures; silane flow = 50 sccm, germane flow = 0.75 sccm, and phosphine fractions are 0, 3, 10, 30, and 100 ppm in silane. 124
6.5 Secondary ion mass spectrometry depth profiles of germanium and/or phosphorus in (a) phosphorus-doped Si/Si, and (b) phosphorus-doped $Si_{0.88}Ge_{0.12}$/Si multilayer structures shown in Fig. 6.4. 125
6.6 Boron and Arsenic incorporation as a function of gas-phase dopant fraction for varied germanium contents. 126
6.7 Phosphorus incorporation as a function of gas-phase dopant fraction for varied germanium contents. 127
6.8 Growth rate as a function of gas-phase diborane and arsine fraction for varied germanium content. 128
6.9 Growth rate as a function of gas-phase phosphine fraction for varied germanium content. 129
6.10 Comparison of boron and phosphorus incorporation in VLPCVD at 620°C and UHVCVD at 600°C. 130
6.11 Comparison of phosphorus-doped silicon growth rate in VLPCVD at 620°C and UHVCVD at 600°C. 133
6.12 $Si_{1-x}Ge_x$ growth expressed as a function of germanium composition for varied phosphine gas-phase fraction. The position of growth-rate peak changes with phosphine fraction. 138
6.13 The exponent factors of a and b in Eq. (6.1) and (6.2) expressed as functions of germanium composition for phosphorus doping. 140

7.1 Comparisons of growth mode of $Si_{1-x}Ge_x$ heteroepitaxy in VLPCVD and MBE. 145
7.2 Critical thickness of VLPCVD $Si_{1-x}Ge_x$ grown at 750 and 620°C. . 149
7.3 Comparison of critical thickness of VLPCVD, LRP, and UHVCVD $Si_{1-x}Ge_x$ strained layers. 150
7.4 Raman spectra of $Si_{0.80}Ge_{0.20}$ on Si as a function of layer thickness. 151
7.5 Plan-view TEM micrographs of 1240 Å $Si_{0.92}Ge_{0.08}$ (as-grown sample shown in (a)) annealed for 30 min at (b) 750°C, (c) 800°C, (d) 850°C, and (e) 900°C. (f) 950°C. (12,000X) 155
7.6 Plan-view TEM micrographs of 1240 Å $Si_{0.87}Ge_{0.13}$ (as-grown sample shown in (a)) annealed for 30 min at (b) 750°C, (c) 800°C, (d) 850°C, and (e) 900°C. (f) 950°C. (14,000X) 157
7.7 Schematic of the Hagen-strunk dislocation multiplication mechanism [141]. 158
7.8 Measured spacing between misfit dislocations in relaxed 1240Å $Si_{0.92}Ge_{0.08}$ and 600Å $Si_{0.87}Ge_{0.13}$ annealed at 750 - 950°C for 30 min. 159
7.9 Perpendicular mismatch of $Si_{1-x}Ge_x$ in $Si/Si_{1-x}Ge_x/Si$ heterostructures (x=0.09, 0.13, and 0.16) annealed at 800 - 1100°C for 30 min in a N_2 flow. 162
7.10 Plan-view TEM micrographs of Si/700 Å $Si_{0.91}Ge_{0.09}$/Si annealed for 30 min at (a) 900°C, (b) 1000°C, and (c) 1100°C. (11,000X) . . 163
7.11 Plan-view TEM micrographs of Si/550 Å $Si_{0.87}Ge_{0.13}$/Si annealed for 30 min at (a) 800°C, (b) 900°C, and (c) 1000°C, and (d) 1100°C. (11,000X) 164
7.12 Plan-view TEM micrographs of Si/550 Å $Si_{0.84}Ge_{0.16}$/Si annealed for 30 min at (a) 800°C, (b) 900°C, (c) 1000°C, and (d) 1100°C. (13,000X) 165
7.13 Ge diffusion profiles in a $Si_{0.80}Ge_{0.20}$/Si structure after 30 min annealing at 900 - 1100°C. 169
7.14 Ge diffusion profiles in a $Si/Si_{0.84}Ge_{0.16}/Si$ structures after 30 min annealing at 900 - 1100°C. 170
7.15 The measured Ge diffusivity as a function of temperature. 171
7.16 Measured strain in Si/B-doped $Si_{0.88}Ge_{0.12}$/Si heterostructures for various B dopant concentration: 0, 10^{18}, and 10^{20} cm^{-3}. 172
7.17 TEM micrographs of (a) undoped $Si_{0.80}Ge_{0.20}$, and (b) B doped (2×10^{19} cm^{-3}) $Si_{0.80}Ge_{0.20}$, after receiving 30 min anneals at 900°C. (9,200X) 173

7.18 Thermal budget for the deposition and annealing of VLPCVD $Si_{1-x}Ge_x$ layers. 174

List of Tables

1.1 CVD techniques demonstrated for $Si_{1-x}Ge_x$/Si heteroepitaxy: LRP:limited reaction processing, UHVCVD:ultrahigh Vacuum CVD, LPCVD:low pressure CVD, RTCVD:rapid thermal CVD, APCVD:atmospheric pressure CVD, VLPCVD:very low pressure CVD [26]-[38]. 24

3.1 Growth conditions for $Si_{1-x}Ge_x$ growth at 750°C. Results obtained by SIMS and TEM are also shown. 55

4.1 Summary of SIMS data for the concentrations of carbon and oxygen impurities existing at the Si/Si-substrate interface and within $Si_{1-x}Ge_x$ layer for varied surface cleaning conditions and $Si_{1-x}Ge_x$ deposition temperatures. 74

Acronyms in This Thesis

APCVD —— atmospheric pressure chemical vapor deposition

CVD —— chemical vapor deposition

DCD —- double-crystal X-ray diffractometry

HBT —— heterojunction bipolar transistor

LOCOS —— localized oxidation on silicon

LPCVD —— very low pressure chemical vapor deposition

LRP —— limited reaction processing

MBE —— molecular beam epitaxy

MODFET —— modulation-doped field-effect transistor

MOSFET —— metal-oxide-semiconductor field effect transistor

PECVD —— plasma-enhanced chemical vapor deposition

RBS —— Rutherford backscattering spectrometry

RTCVD —— rapid thermal chemical vapor deposition

SEM —— scanning electron microscopy

SIMS —— secondary ion mass spectrometry

TEM —— transmission electron microscopy

UHVCVD —— ultrahigh vacuum chemical vapor deposition

VLPCVD —— very low pressure chemical vapor deposition

XTEM —— cross-sectional transmission electron microscopy

Chapter 1

Introduction

1.1 Introduction

Although many elements and intermetallic compound exhibit semiconducting properties, silicon is presently the most important semiconductor for the electronics industry, with VLSI technologies relying almost entirely on silicon. The dominant position of silicon can be attributed to a number of factors: silicon is the second element in abundance only to oxygen on earth and can be refined to ultrahigh purity and grown into nearly perfect crystals, silicon oxide provides the superb properties for planar processing technologies, and silicon has unique etching properties and excellent mechanical properties [1, 2]. However, on its electronic merits alone, silicon is not an optimum choice. For example, silicon has only average high-field breakdown characteristics, free carrier mobility, and carrier saturation velocity. Moreover, the high minority-carrier lifetimes of silicon are offset by its indirect bandgap. As a consequence, many important electro-optical applications are not possible with silicon devices or microcircuits [3].

Since silicon-based technology is used almost exclusively in the fabrication of modern integrated circuit, new options and impacts would be possible for the huge and fast-growing integrated-circuit market if we can combine silicon fwith other semiconducting materials which provide the unique properties allowing functions

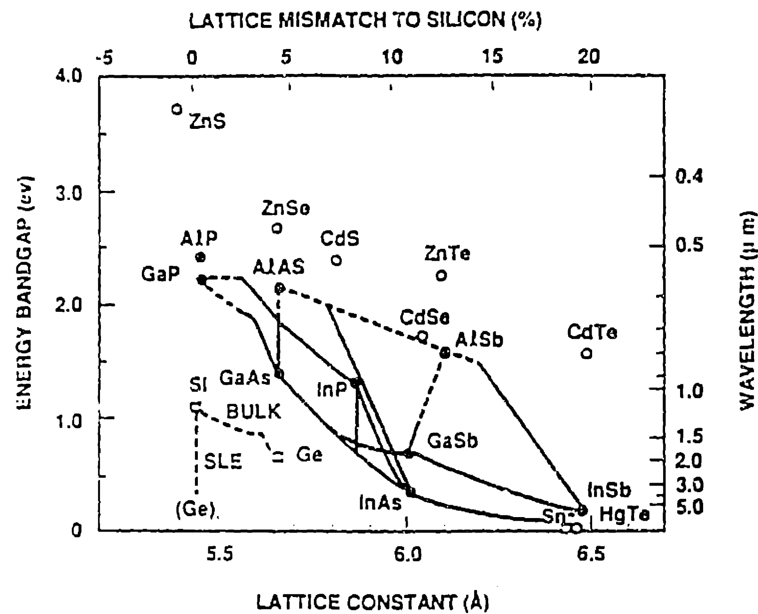

Figure 1.1: Band gap of semiconducting materials as a function of lattice constant [4].

that cannot be performed by silicon alone. Furthermore, it may even become possible to custom design novel artificial structures, such as strained-layer superlattices and quantum well structures, using silicon processing for specific applications. To date, most approaches to this technological challenge are based on growing epitaxial layers of novel materials on the silicon substrate. These intense efforts have in fact opened an exciting area in both fundamental studies and device applications: *heteroepitaxial growth on silicon.*

Because most semiconductor devices depend on crystalline perfection and excess lattice mismatch can lead to strain relief via the generation of defects, one must use the materials with similar crystal structures and nearly identical lattice constants to achieve high-quality heteroepitaxial growth on silicon substrate. Figure 1.1 compares the lattice constant of silicon with a number of semiconductors [4]. Relatively few semiconductor lattices match to silicon except GaP, AlP, and ZnS.

1.2 Literature Review

1.2.1 Growth Principles

Starting from metallic systems, heteroepitaxial growth has been studied as a fundamental problem for over six decades. Only in the past two decades, however, has there existed a practical interest in understanding the phenomena more completely. This recent practical interest has arisen from the great need of the semiconductor industry for high-quality thin films. As the use of electronic devices became more demanding and sophisticated, the need for films free of defects has increased. This section will discuss two major problems associated with heteroepitaxial growth: two/three dimensional growth and coherent/incoherent growth.

Two/Three Dimensional Growth

On the basis of thermodynamics, the epitaxial growth can be classified as (i) Frank and van der Merwe growth (monolayer-by-monolayer, two-dimensional growth), (ii) Volmer-Weber growth (island, three-dimensional growth), and (iii) Stranski-Krastanov growth (island on top of a few monolayers, growth mode changes from two-dimensional to three dimensional), as illustrated in Fig. 1.2 [9]-[12]. If epitaxial growth occurs via the Frank and van der Merwe mode, the two-dimensional growth by the motion of mono-atomic steps yield smooth layers. Furthermore, in absence of diffusion or exchange effects, one can expect an atomically abrupt interface. While island growth and coalescence of islands take place, the surface will become rough and defects may form during island coalescence. Since the formation of smooth and planar interfaces and of uniform epilayers are required for heterostructure devices, particularly for devices based on superlattices, two-dimensional growth is highly desirable. Unfortunately, in lattice mismatched systems, where high interfacial energy and strain energy are expected, island formation is energetically favored. This would be the situation if there were a high

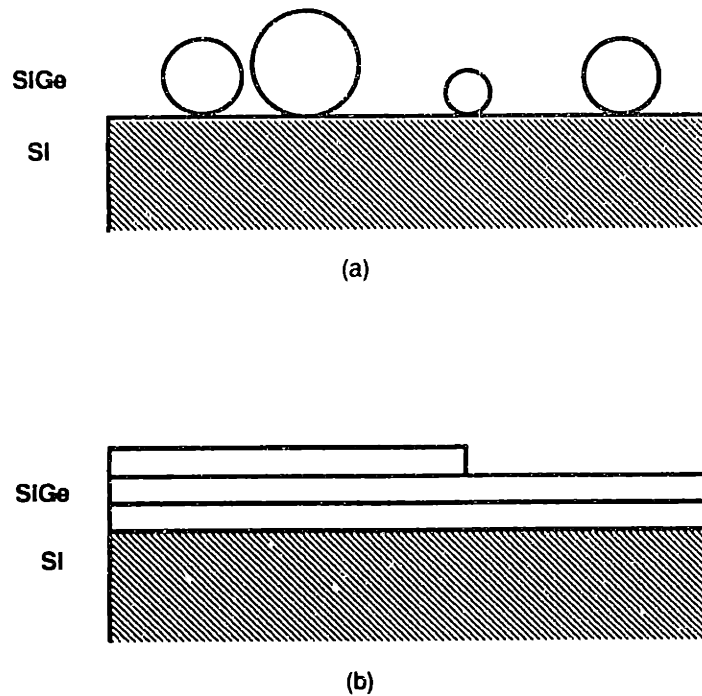

Figure 1.2: Possible growth modes of $Si_{1-x}Ge_x$ heteroepitaxial growth on silicon

energy associated with the hetero-interface which affects the wetting angle of epilayer and substrate or if islanding facilitated relaxation of the strain energy within the epilayer [13, 14]. The strong tendency towards three-dimensional growth due to lattice mismatch in the Ge/Si systems had been shown by Cullis and Booker [15].

Coherent/Incoherent Growth

In addition to island formation, another fundamental problem associated with heteroepitaxial growth is the limit of layer thickness. It has long been recognized that in lattice-mismatched heteroepitaxy, there exists a characteristic thickness h_c only below which lattice mismatch between substrate and epilayer can be accommodated entirely by layer strain. The epilayer is strained such that the lattice parameters parallel to the hetero-interface are identical and and the growth is

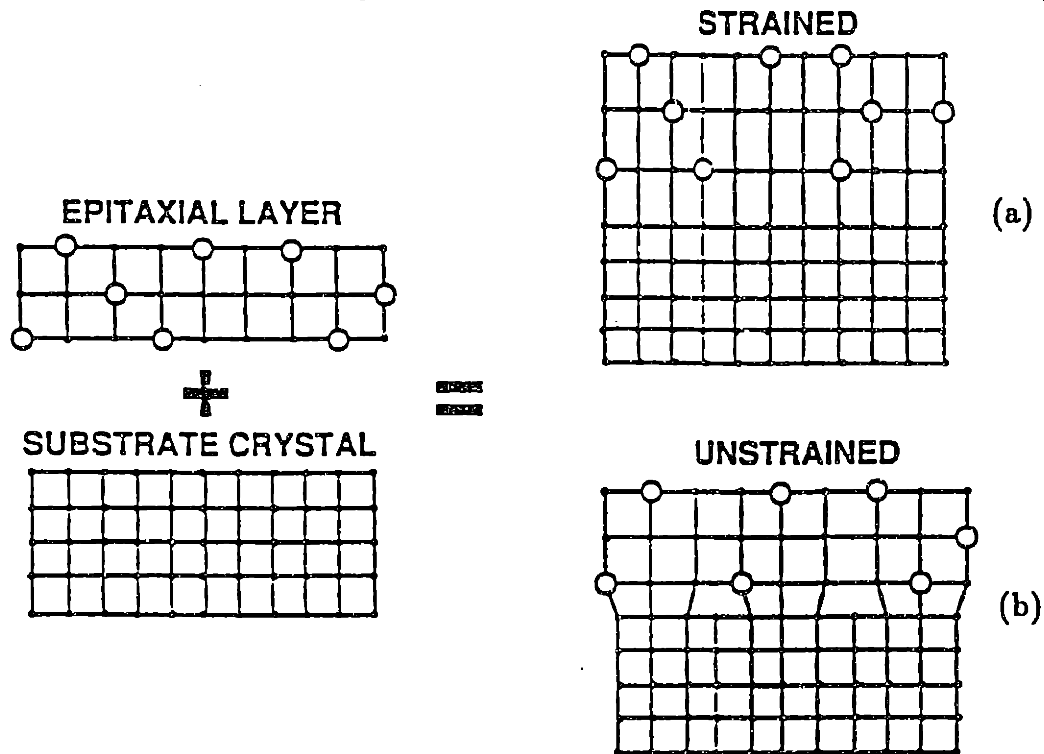

Figure 1.3: Schematic illustration of epitaxial strained layer and unstrained layer.

described as pseudomorphic or commensurate. Figure 1.3 shows a schematic illustration of heteroepitaxial growth on a Si substrate. When the thickness is under h_c, the deposited heteroepitaxial layer can be strained under biaxial stress to match the substrate and a defect-free interface will be formed, as shown schematically in Figure 1.3 (a). This result gives elastic strain energy stored in the epilayer. If the thickness of the growing layer exceeds h_c, it becomes energetically favorable for misfit dislocations to relieve elastic strain energy and the lattice parameter of epilayer will relax toward its own free value, as depicted in Figure 1.3 (b). The modeling of critical thickness for heteroepitaxy began as early as 1949 with the pioneering work of Frank and van der Merwe [16]-[18] and was extended by Matthew in the 1960's [19]-[21]. Although these models based on thermodynamic equilibrium and mechanical equilibrium theories were original developed for metals, they can be applied to the Ge-Si system as reported by Kasper et al. [22]. In

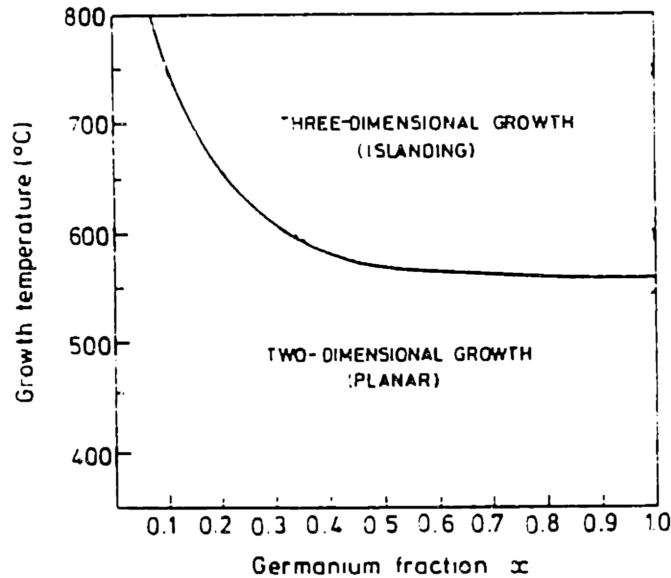

Figure 1.4: Plot of $Si_{1-x}Ge_x$ growth mode with respect to Ge composition and growth temperature [13].

their early experimental studies, Kasper et al. indicated that the critical thickness of $Si_{1-x}Ge_x$ strained layers grown on Si was in approximate agreement with the theories suggested by Matthews [19]-[21] though small discrepancies were noted. Also, they found $Si_{1-x}Ge_x$ islanding on Si could be eliminated at 750°C. Unfortunately, the smooth layer could only be grown for alloys with Ge fractions less than 15-20% and the measured critical thicknesses were quite small that would be of little use in current devices. Encouraged by Manasevit et al.'s work in 1982 [23] describing the anomalous carrier mobility in $Si_{1-x}Ge_x$/Si superlattices in which strained layer heteropeitaxy was not claimed, Bean et al. gave $Si_{1-x}Ge_x$ another try by refining state-of-the-art MBE and sample preparation. From the growth of $Si_{1-x}Ge_x$ on Si for all compositions (x = 0-1) over a wide range of deposition temperatures (400–750°C), Bean et al. demonstrated in 1984 that: (1) Pseudomorphic growth of $Si_{1-x}Ge_x$ on Si was confirmed with Ge composition up to 50%. (2) Pseudomorphic growth was maintained for layer thicknesses up to 0.25μm. (Such

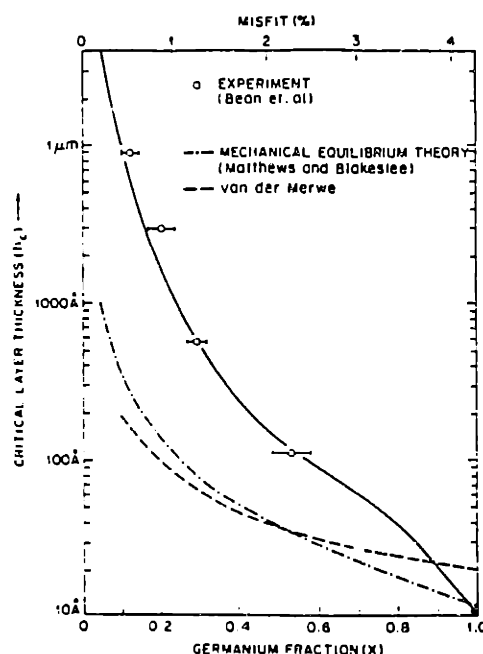

Figure 1.5: Open circles and solid line are experimental single layer critical thicknesses and their empirical expression reported by People and Bean [25]. Lowered dashed curve – van der Merwe (theory); middle dot-dashed – Matthews and Blakeslee (theory).

thicknesses are approximately an order of magnitude larger than those predicted by equilibrium theories.), and (3) A $Si_{1-x}Ge_x$/Si strained-layer superlattice was grown [13, 14, 24]. The exciting results showed that, although island formation is energetically favored in $Si_{1-x}Ge_x$ growth on Si, three-dimensional growth can be avoided by lower temperature deposition where atomic surface migration lengths are so short that macroscopic islands cannot form. In other word, the smooth growth was achieved by incorporation of "frozen-out" surface atoms. Figure 1.4 indicates the transition from two-dimensional to three-dimensional growth as functions of growth temperature and Ge fraction. Note that the limited surface migration can reduce the crystal quality at lower temperature. Thus the deposition temperature for $Si_{1-x}Ge_x$ growth should be optimized to maintain both two-dimensional growth and high-quality epitaxy. Another important conclusion from Bean et al.'s study is that, at low temperature, the $Si_{1-x}Ge_x$ strained layer can be grown up to

the thickness well beyond the predicted equilibrium limits, as shown in Figure 1.5 [25]. The discrepancy suggests the existence of a kinetic barrier to the formation or motion of misfit dislocations which allows the growth of metastable $Si_{1-x}Ge_x$ layer in excess of equilibrium h_c. Further, interdiffusion can also be minimized at low temperatures.

The enhancement of two-dimensional growth and the increase of strained-layer thickness by low-temperature deposition is very encouraging and allows fabrication of $Si_{1-x}Ge_x/Si$ heterostructures for practical applications. Since then, the $Si_{1-x}Ge_x$-Si system has drawn much attention for its great potential. The following section will summarize the state-of-the-art low-temperature growth techniques that have been applied in recent years to the growth of $Si_{1-x}Ge_x$ on Si.

1.2.2 CVD Techniques for $Si_{1-x}Ge_x$ Deposition

Although initiated by MBE, recent progress with the heteroepitaxial growth of $Si_{1-x}Ge_x$ on Si using CVD has been reported. Compared with MBE, which is much more expensive and complicated, CVD is of great interest since this technique appears to be compatible with manufacturing requirements such as high throughput, conformal coverage, and low cost. Table 1.1 summarizes the CVD-related techniques that have been employed for $Si_{1-x}Ge_x$ growth on Si [26]-[38]. The source gases and deposition temperatures for different technique are also indicated.

Among these demonstrated CVD reactors for $Si_{1-x}Ge_x$ heteroepitaxial growth, limited reaction processing (LRP) is one of the first CVD-related techniques that demonstrated a rapid thermal processing for strained layer $Si_{1-x}Ge_x$ growth. In this system (Fig. 1.6 [39]), the substrate is supported by three quartz pins and the substrate temperature can be rapidly changed at the heat up and cool down rates of 1-5 ms°C^{-1} by two banks of six air-cooled 1.2 kW tungsten halogen lamps activated by a microprocessor that provides a desired temperature versus time profile

Research Group	Technique	Process Gases	Carrier gas	Temperature	Reference
Stanford	LRP	SiH_2Cl_2, GeH_4	H_2	625°C, 900°C	[26]
IBM	UHVCVD	SiH_4, GeH_4	no	550°C	[27]
NTT	LPCVD	Si_2H_6, GeH_4	H_2	550-700°C	[28]
Princeton	RTCVD	SiH_2Cl_2, GeH_4	H_2	625°C	[29]
CMU	UHVCVD	SiH_4, GeH_4	H_2	577-665°C	[30]
UT, Austin	RTCVD	SiH_2Cl_2, GeH_4	H_2	1000°C	[31]
IBM	APCVD	SiH_2Cl_2, GeH_4	H_2	625°C	[32]
NCSU	RTCVD	SiH_2Cl_2, GeH_4	H_2	500–800°C	[33]
Spire	APCVD	SiH_4, $SiHCl_3$, $GeCl_4$	H_2	800–1000	[34]
AT&T	RTCVD	SiH_2Cl_2, GeH_4	H_2	900°C	[35]
RSRT	LPCVD	SiH_4, GeH_4	H_2	610–750°C	[36]
Philips & ASM	APCVD	SiH_2Cl_2, GeH_4	H_2	625°C	[37]
HP & ASM	APCVD	SiH_2Cl_2, GeH_4	H_2	600–900°C	[38]

Table 1.1: CVD techniques demonstrated for $Si_{1-x}Ge_x/Si$ heteroepitaxy: LRP:limited reaction processing, UHVCVD:ultrahigh Vacuum CVD, LPCVD:low pressure CVD, RTCVD:rapid thermal CVD, APCVD:atmospheric pressure CVD, VLPCVD:very low pressure CVD [26]-[38].

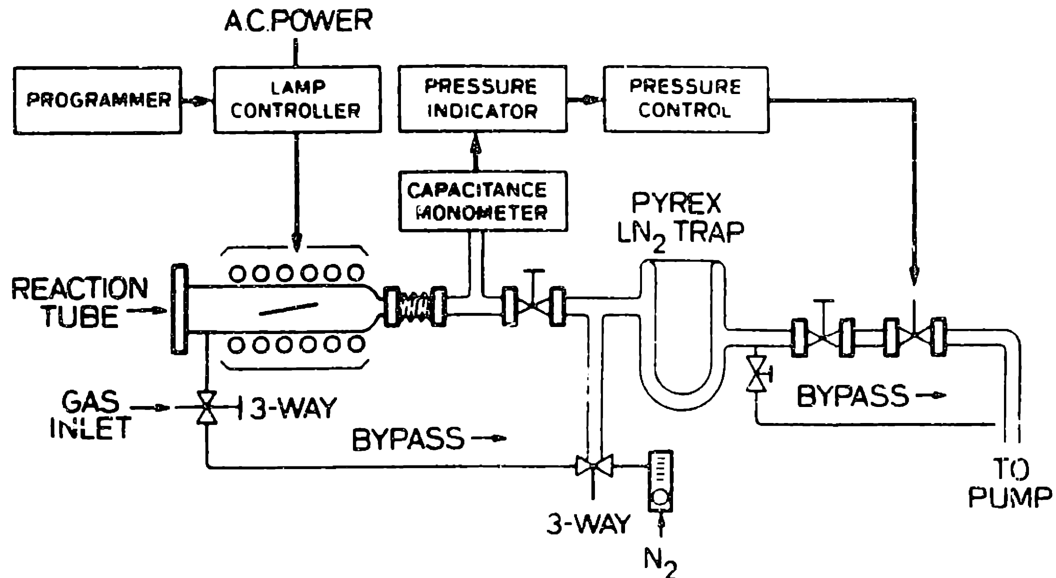

Figure 1.6: Schematic of the Stanford LRP reactor [39].

[26]. This reactor design is very similar to that used by Tedrow et al. for the growth of silicide layers [40]. Such tight temperature control translates to precise control over a thermally driven surface reaction, such as chemical vapor deposition, and epitaxial growth occurs and stops when the lamps are on and off. Thus, this technique is also referred to as limited reaction processing. In LRP, gas is introduced into the chamber while the substrate is cool, in between two high temperature cycles. By changing the gas flows between high-temperature cycles, layers of different compositions can be produced. (This idea is very similar to that proposed by Reif and Fonstad for using a plasma as an on/off switch for heteroepitaxial depositions [41]). As a result of rapid temperature changes that turn a surface reaction on and off, $Si_{1-x}Ge_x/Si$ interfaces are abrupt to within approximately 20Å. Based on a similar configuration, another type of rapid thermal process, RTCVD, was developed to deposit thin films at low temperatures.

Rapid thermal chemical vapor deposition (RTCVD) also uses two banks

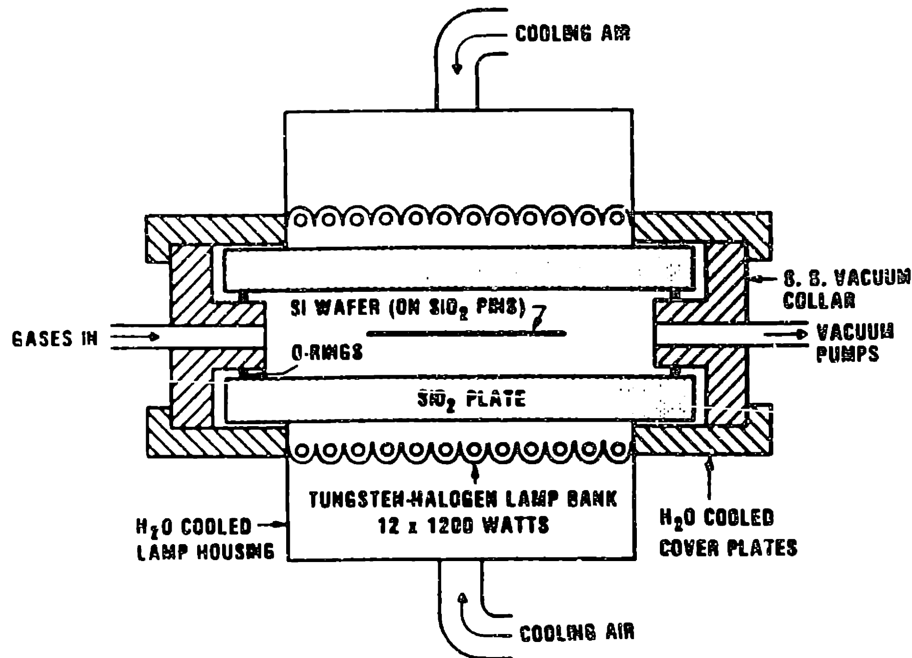

Figure 1.7: Schematic of the AT&T RTCVD reactor [42].

of six 1.2 kW tungsten lamps with substrate mounting on three quartz pins, as shown in Fig. 1.7 [42]. However, unlike LRP, the films are grown by means of gas switching and the lamps are not turned off between the two deposition steps. In both systems, native oxide is removed by a H_2 bake or HCl/H_2 etch in a short time above 1000°C, followed by rapid cooling of substrate before epitaxial growth begins. By allowing brief excursions to higher deposition temperatures, thermal budget is minimized and autodoping and dopant distribution are suppressed. Processing gases used are SiH_2Cl_2 and GeH_4 in a H_2 carrier gas.

Taking advantage of hydrogen passivation by HF pretreatment and thermal desorption of oxide in ultrahigh vacuum, UHVCVD makes $Si_{1-x}Ge_x$ epitaxial growth possible at $425 \leq T \leq 650°C$ and $T > 750°C$. Fig 1.8 shows the schematic of the IBM UHVCVD reactor [43]. Before loading, substrates were subjected to a 45 sec, 10:1 HF dip, and then mounted on a substrate carrier placed coaxial with the tube centerline. A loadlock is utilized to eliminate contamination upon load-

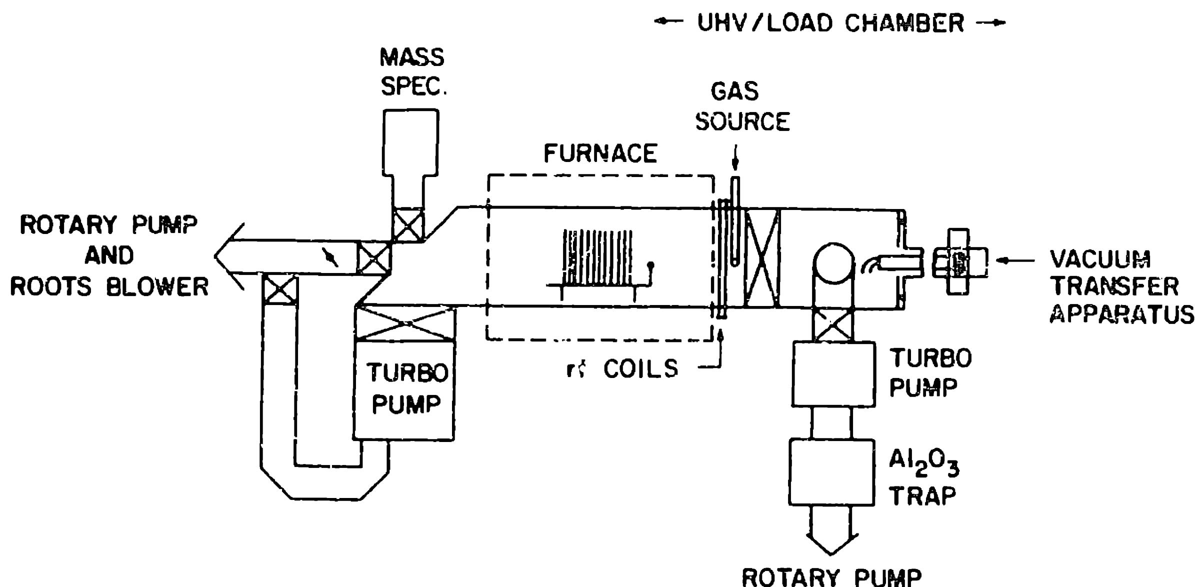

Figure 1.8: Schematic of the IBM UHVCVD reactor [43].

ing. The substrate carrier received a 30 min prebake at 100°C prior to its transfer into the ultrahigh vacuum chamber. A 5 min purge with 600 sccm H_2 hydrogen was then carried out, followed by the deposition cycle. No *in situ* surface clean is employed and the epitaxial growth relies upon stringent adherence to ultrapure environment to maintain an atomically bare silicon surface before deposition begins. The high-purity environment during growth ensures minimal contamination. Typical deposition temperature for $Si_{1-x}Ge_x$ growth is 550°C with SiH_4 and GeH_4 as processing gases. Abrupt interfaces and excellent thickness and composition uniformity have been achieved [27].

Low pressure chemical vapor deposition (LPCVD) has also been investigated for $Si_{1-x}Ge_x$ growth [36]. The proposed epitaxial process was carried out in a UHV compatible cold-wall reactor and the substrate is radiantly heated by a graphite filament in close proximity to the back surface of the substrate. The surface oxide is desorbed at 900°C in H_2 immediatedly prior to epitaxy. The reactant

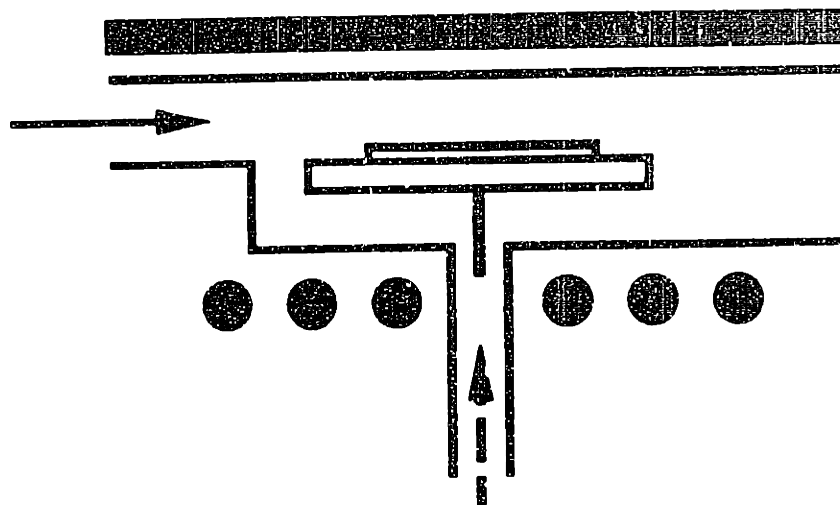

Figure 1.9: Schematic of the ASM Epsilon One APCVD reactor [44].

gas is a H_2-GeH_4- SiH_4 mixture at a constant pressure of about 1 Torr. Just like in VLPCVD, the combination of a cold-wall reaction chamber and low pressure favor heterogeneous reaction kinetics.

APCVD is by far the reactor holding greatest promise for widespread commercial use of $Si_{1-x}Ge_x$ heteroepitaxy because it is available commercially and it is relatively simple. In the commercially available reactor, the Epsilon One reactor of ASM Epitaxy (Fig. 1.9 [44]), the bake conditions are similar to what is used for conventional high-temperature CVD: 3 min 1180°C in H_2 and 30 sec in HCl [38]. Following surface clean, the susceptor takes a few minutes to cool before the temperature stabilizes. The deposition is initiated and terminated by switching the silicon and germanium source gases into and out of the reactor chamber while the substrate temperature remains essentially constant. SiH_2Cl_2, GeH_4, and H_2 are routinely employed in APCVD. Since deposition is carried out at atmospheric pressure, gas purification, load lock, and rigorously clean operating procedures are

utilized to insure low levels of oxygen and moisture contamination. The substrate resides on a SiC coated graphite susceptor and heated radiantly. Native oxide may also be removed in a prebake before deposition at 850°C for 10 min in hydrogen [45]. Using APCVD, epitaxial $Si_{1-x}Ge_x$ growth temperatures as low as 550°C has been reported. In addition, $Si_{1-x}Ge_x$ exhibits good turn-on and turn-off transients.

Although high quality films can be obtained using CVD. The kinetic processes in $Si_{1-x}Ge_x$ growth is still not clear. Moreover, confusing results have been reported in the literature. For example, the first cooperative phenomenon was observed by Meyerson et al. where the addition of GeH_4 to the gas source was found to enhance the $Si_{1-x}Ge_x$ growth rate at 550°C in SiH_4 and GeH_4 reactant gases [27]. Using more recent ultrahigh vacuum chemical vapor deposition (UHV/CVD) with H_2-SiH_4-GeH_4 mixtures in the temperature range of 577°C – 665°C, another study showed a peak of growth rate as a function of GeH_4/H_2 flow rate [30]. The same behavior has also been reported later by Robbins et al. using LPCVD at 750°C with H_2-SiH_4-GeH_4 mixtures [36]. In that paper, the temperature dependencies of $Si_{1-x}Ge_x$ growth rates at 650°C and 610°C were also investigated and found to be similar to the recent UHV/CVD data. However, using H_2-SiH_2Cl_2-GeH_4 mixtures in limited reaction processing (LRP) in the temperature range of 625°C-800°C, studies showed a monotonic increase in $Si_{1-x}Ge_x$ growth rate with the increase of GeH_4 flow rate [29, 46]. Careful analysis indicated that, using SiH_2Cl_2, GeH_4, and H_2, the growth rate is not limited by hydrogen desorption [29]. A model accounting for the peak in growth rate was proposed by Robbins *et al.* by considering the competition between an increasing rate for hydrogen desorption and a decreasing sticking probability for reactive hydrides as x increases [36]. But the details are still not clear.

1.2.3 Thermal Stability

In this section, an extremely important issue, thermal relaxation, associated with the post-deposition processing of $Si_{1-x}Ge_x$ strained layers will be discussed.

It has been shown that, through MBE or CVD, a pseudomorphic strained $Si_{1-x}Ge_x$/Si heterostructure can be grown at low temperatures to a thickness well beyond the critical thickness predicted by thermodynamic or mechanical equilibrium theories. The existence of a kinetic barrier to strain relaxation at low deposition temperature give rise to the *metastable* $Si_{1-x}Ge_x$/Si heterostructures in excess of the equilibrium h_c. However, the strained as-grown layers in the metastable state may relax if the thermal budget associated with device fabrication is too high. Strain relaxation may occur either via misfit dislocation formation or via Ge diffusion [47].

In recent years, the strain relaxation of the metastable $Si_{1-x}Ge_x$/Si heterostructures upon annealing have been widely studied [47]-[60]. One important issue associated with the relaxation of misfit strain is the sources for dislocation generation. The mechanisms for dislocation nucleation, that determine the critical thickness, have been widely studied. In addition to homogeneous nucleation mechanisms, which the majority of critical thickness research is based on (including direct or internal dislocation nucleation, dislocation half-loop nucleation at the free surface or at the surface containing irregularities producing local stress concentrations), heterogeneous nucleation mechanisms have also been investigated. The proposed possible heterogeneous nucleation sources involve local stress concentrations at surface heterogeneities, precipitate-induced defects, and oxygen/carbon contamination [52].

Besides dislocation nucleation, the movement of dislocations is also a major concern in the study of strain relaxation. During relaxation, major factors attributed to the rate of strain relief include the lattice misfit, the layer thickness,

the annealing temperature, the density of misfit dislocation nucleation centers, the glide and/or climb velocities of misfit dislocations, and the efficiency of dislocation multiplication process. Fiory et al. first reported the metastable nature of $Si_{1-x}Ge_x$ strained layers with thickness exceeding h_c [47]. They annealed samples at different temperatures up to 1050°C. Initially, all their films show a logarithmic time dependence in the growth of misfit dislocations at 850°C. For thinner samples annealed at different temperatures, no activated process was observed. However, above 850°C, thicker films dislocate rapidly. They postulated that the rapid increase in dislocation density is caused by dislocation climb aided by Ge diffusion. Interdiffusion is a competing mechanism and for thinner films (100Å) dominates. LeGoues et al. indicated that the initial condition of the interface is critical in determining which mechanism will dominate [48]. When the dislocation density at the interface is low, strain tends to relax predominately by interdiffusion. When the dislocation density is high, strain mainly relaxes by dislocation multiplication. By *in-situ* observation of strain relaxation, Hull et al. showed that at low Ge concentrations, annealing between 550 and 750°C led to significant strain relaxation [57]. But the samples with higher Ge concentrations relaxed far more gradually. This is ascribed to the dislocation interactions in the high Ge films. Concerning the relaxation processes, Tuppen et al. measured the misfit dislocation glide velocity and found the velocity depends on a number of factors including annealing temperature, an activation energy (which was found to depend on the Ge fraction), the effective misfit stress (which is a function of Ge mole fraction and layer thickness), and the length of the threading arm of the misfit dislocation [53]. They reported that the activation energy for misfit dislocation glide is 2.2±0.2 eV for $Si_{0.95}Ge_{0.05}$ and 2.2±0.3 eV for $Si_{0.87}Ge_{0.13}$. Houghton el at. also measured the misfit dislocation glide velocity and found, for all geometries and for effective stress in the range 100–750 MPa, the mean activation energy for misfit dislocation glide is 2.25±0.05 eV with the Ge fraction between 0.035 and 0.25 [55].

As the concerns over the possible relaxation arises for device fabrication, the understanding of the relaxation process becomes important and it will be necessary to codify the appropriate stability criteria to predict whether or not a particular $Si_{1-x}Ge_x$/Si strained heterostructure will survive a designed process.

1.2.4 $Si_{1-x}Ge_x$ Heteroepitaxy Applications

The attraction of $Si_{1-x}Ge_x$ heteroepitaxy on Si arises from its smaller bandgap compared to Si. SiGe-base heterojunction bipolar transistors (HBTs) offer numerous advantages for high-speed digital and microwave circuits: higher current and/or lower intrinsic base resistance, higher speed with a graded bandgap in the base, and improved low-temperature performance and operation. In addition, $Si_{1-x}Ge_x$ is also attractive for modulation-doped field-effect transistors (MODFETs) because of its enhanced carrier mobility. Since the bandgap discontinuity between $Si_{1-x}Ge_x$ and silicon mostly appears in the valence band, p-channel devices can further take advantage of modulation doping and carrier confinement in a $Si_{1-x}Ge_x$ channel and improve both circuit speed and integration level compared to conventional silicon p-channel metal-oxide-semiconductor field effect transistors. In this section, the two well demonstrated $Si_{1-x}Ge_x$ devices, HBT and MODFET, are described.

Heterojunction Bipolar Transistors

The basic concepts underlying the heterojunction bipolar transistor(HBT) were outlined about 40 years ago by William Shockley:

"What is claimed is:

(1) ...

(2) a device as set forth in claim 1 in which one of the separated zones is of a semiconductor material having a wider energy gap than that of the material in the

other zones."

Claim 2 of U.S. patent 2 569 347 to W. Shockley,

Filed 26 June 1948,

Issued 25 September 1951,

Expired 24 September 1968.

About ten years later Herbert Kroemer published the first journal article [61] describing the remarkable advantages that an HBT holds over a conventional bipolar transistor. Since then, heterojunction devices have been extensively studied.

The underlying basic principle of HBT is the use of energy gap variations beside electric fields to control the forces acting on electrons and holes, separately and independent of each other. Fig. 1.10 illustrates the principle underlying most heterostructure devices [62]. In ideal homostructures, the energy gap is constant; hence the slope of the two band edges are equal, and the forces acting on electrons and holes are necessarily equal in magnitude and opposite in sign. In fact they are equal to the ordinary electrostatic force $\pm q\vec{E}$. In a heterostructure, the energy gap may vary; hence two band edge slopes and the two forces need not be the same, nor need they be in any simple way related to the electrostatic force exerted by $\vec{E}$. Indeed, the two slopes may have opposite signs as shown in Fig. 1.10. implying forces on electrons and holes are in the same direction, despite their opposite charges. The possibility of control over the motion of electrons and holes within a bipolar transistor provides an extra degree of freedom in device design.

The performance of a bipolar transistor is determined by many compromises; [63, 64] those between gain and base resistance, base width and breakdown or punch-through voltage, breakdown voltage and collector capacitance are just a few examples. In conventional bipolar junction transistors (BJT), for high current gain it is desirable that the base of the transistor be lightly doped with respect to the doping level in the emitter. This reduces the number of minority carriers

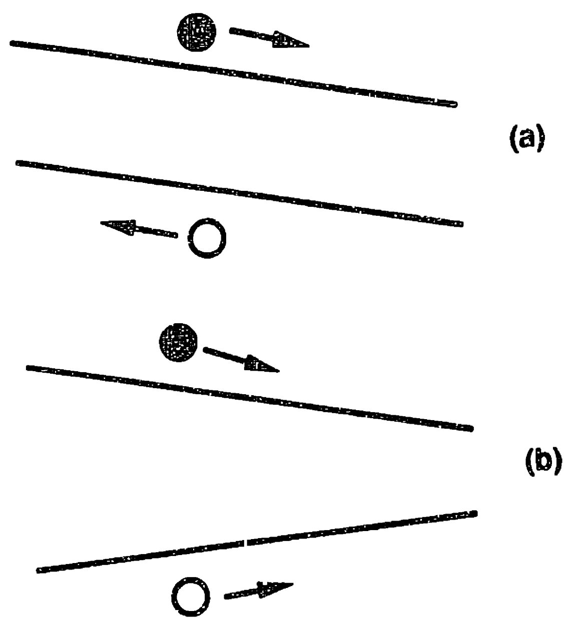

Figure 1.10: Forces on electrons and holes. In a uniform-gap semiconductor (a) the two forces are equal and opposite to each other, and equal to electrostatic force. In a graded-gap structure (b), the forces in electrons and holes may be in the same direction [66].

available for reverse injection into the emitter which increases the current gain. But the relatively light doping in the base creates a number of problems such as lateral bias effects caused by current flow in the base resistance. Lateral bias effects contribute to non-uniform emitter current flow paths, known as emitter crowding effects, that must be solved by emitter and base contact interdigitation. Other effects of relatively high base resistance may be "reach-through" of the base depletion region from the collector to the emitter at a low base-collector voltage level. The lateral bias effects may also contribute to "second-breakdown" in a transistor due to current pinch-in effects. High base resistance may also be a factor in the frequency response of a transistor because of the r_bC_c time constant, where r_b is the base resistance and C_c is the collector capacitance. Therefore high base doping might be needed to reduce base resistance, and particularly in scaled devices, to avoid base punchthrough at high V_{cb} and lateral bias effect. High base doping,

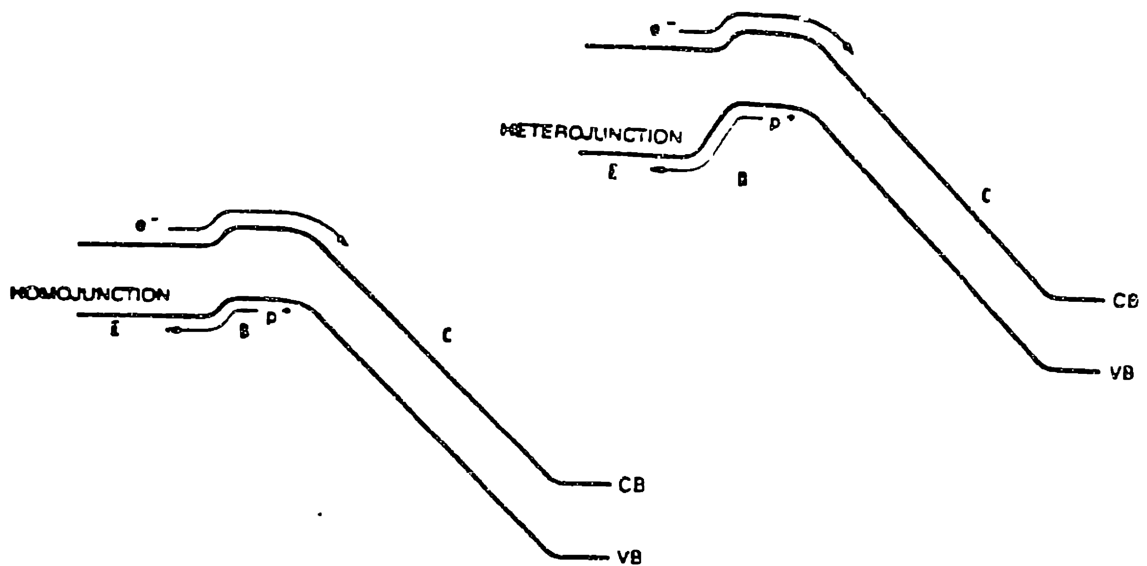

Figure 1.11: The band diagrams of npn homojunction and heterojunction transistors [66].

however, reduces emitter injection efficiency and causes hole storage in the emitter, reducing device speed. These problems are alleviated somewhat by high emitter doping, at the cost of high B-E capacitance and low breakdown voltage. Moreover, the effectiveness of this fix is compromised by emitter band gap shrinkage with high doping [65]. Hence, the transistor designer has to keep all of the factors under control and in balance. But in the HBT, the freedom to engineer both band gap and band offset is greater. Fig. 1.11 shows the difference of the band diagrams of npn homojunction and heterojunction transistors [66]. In the heterojunction transistor in Fig. 1.11, the energy barrier for the injection of holes from the base into the emitter can be made larger than that for electron injection into the base, with a resulting increase in gain. Consequently, the doping level in the base may be raised, increasing the threshold current density at which high injection effects begin to degrade transistor performance. In turn, the collector doping can be raised to reduce the B-C depletion width. Hence, each of the components of the

transit time equation is reduced, giving a significant improvement in the transistor's transit frequency. The collector capacitance is increased, but this is more than compensated by the combination of reduced base resistance and increased transit frequency. Thus the maximum oscillation is also improved. Furthermore, since the digital switching speed and analogue bandwidths are related to these two figures of merit, and the noise of the transistor is largely controlled by the base resistance, the HBT offers remarkable advantages over the conventional BJT for all applications.

Although the idea of HBT is as old as the transistor and its potential advantages have been long recognized, no technology offered the promise of making heterostructures until the early 70's when liquid-phase epitaxy appeared as a technology for III-V heterostructures. Since the mid-70's two additional very promising heterostructure technologies have appeared: molecular beam epitaxy [67] and metal-organic chemical vapor deposition [68], and impressive results on III-V heterostructures have been achieved. In III-V systems, the similarity of lattice constants of two semiconductors (e.g. GaAs and AlGaAs) allows almost complete freedom of choice of layer thickness and composition and spectacular high-frequency results have been obtained using $Al_{1-x}Ga_xAs$ as the wide-gap emitter and GaAs as the base [65, 69]. However, the cost and throughput problems associated with the epitaxial layer growth and the lack of a stable insulator for device processing have limited commercial availability of these devices. Besides, the split of the bandgap discontinuity between the valence and conduction bands leads to nonb-ideal properties. In particularly, an energy spike in the conduction band can form at the interface unless it is graded. This leads to additional complication in layer growth, and gives a potential source of nonuniformity in device parameter.

Since silicon is the dominant material in current semiconductor industry and III-V systems are not yet compatible with silicon processing, significant ef-

forts have been made toward obtaining an HBT within silicon technology where an HBT coupled with the existing and fast expanding silicon processing technologies can be obtained. The simplest way, from a process integration point of way, is to implement a wide bandgap emitter. Several materials, in addition to the conventional polysilicon emitter, have been tried over the years, such as oxygen-doped silicon epitaxial films [70], β-SiC [71], amorphous silicon [72], and microcrystalline silicon [73]. An inherent limitation of the wide-bandgap emitter approach is that it offers no means to reduce the base transit time, which is the dominant component at high current densities in a conventional polysilicon-emitter transistor. In addition, high thermal requirements for processing them, high bulk and contact resistivities, and the inability to form good quality junctions with silicon have degraded the performance of these materials.

Significant progress in the growth of $Si_{1-x}Ge_x$ strained layers in recent years has opened the possibility of obtaining a narrow-bandgap-base HBT technology in silicon [6]. Due to the lower bandgap of the $Si_{1-x}Ge_x$ base, the emitter injection efficiency is improved as shown in Fig. 1.11 and is less dependent on the doping levels in the emitter and the base. Therefore a high base doping can be used to achieve low base resistance, low noise figure, and high current density and a low emitter doping can be incorporated for high cut-off frequency and high breakdown voltage. Furthermore, the Ge profile can be tailored to maximize the transit frequency.

Modulation-doped Field Effect Transistors

Some of the geometries and basic ideas underlying the metal-oxide-semiconductor field-effect transistor (MOSFET) were described sixty years ago by Julius Edgar Lilienfeld in the first two of his three patents. Applications of Liliendfeld's three patents were filed in October 1926, March 1928, and December 1928, and were

granted in 1930, 1933, and 1932, respectively [74]. The chronological advances of the MOSFET can be divided into three phases: a discovery phase during the first thirty years from 1928 to 1958, a technology development and new device structure invention phase during the next ten years from 1959 to 1968, and the MOS transistor integration and integrated circuit manufacturing phase from 1969 to today [74]. Since the invention of the FET, the development of Si processing technology that most commercial MOSFETs are based on, has been astounding, and in response to continual demands for high switching speeds and smaller device dimension, the invention and development of novel field-effect devices continues to today. Modulation-Doped Field-Effect Transistor (MODFET) is an excellent example.

It is well known that one of the principal scattering mechanisms that limits carrier mobility in semiconductors is ionized impurity scattering. For example, at room temperature the upper limit of bulk mobility in undoped Si is about 1500 cm^2/V-sec for electrons and 450 cm^2/V-sec for holes. But after doping Si to a concentration of 10^{18} donors(acceptors)/cm^3, the mobilities of electrons and holes are degraded considerably to about 275 cm^2/V-sec and 140 cm^2/V-sec, respectively. By spatially separating carriers from ionized impurities, the limit of ionized impurity scattering can be reduced, and electron or hole mobility rises. In the heterojunction case, the spatial separation between ionized impurities and carriers can be achieved by doping only the material with higher band edge so that the carriers are collected and confined in the material with the lower band edge. This idea is called modulation-doping. Since the bandgap in $Si_{1-x}Ge_x$ is strain-dependent, the combination of strain and alloy composition may yield distinct band alignments. The examples are presented as follows: (i) growth of $Si_{0.80}Ge_{0.20}$/Si heterojunctions on (001) Si substrates, (ii) growth of $Si_{0.50}Ge_{0.50}$/Si heterojunctions of equal thickness on an unstrained (001)-$Si_{0.75}Ge_{0.25}$ bufpfer layer, and (iii) growth of $Si_{0.50}Ge_{0.50}$/Si heterojunctions on (001)-Si [7]. These resultant bandgaps

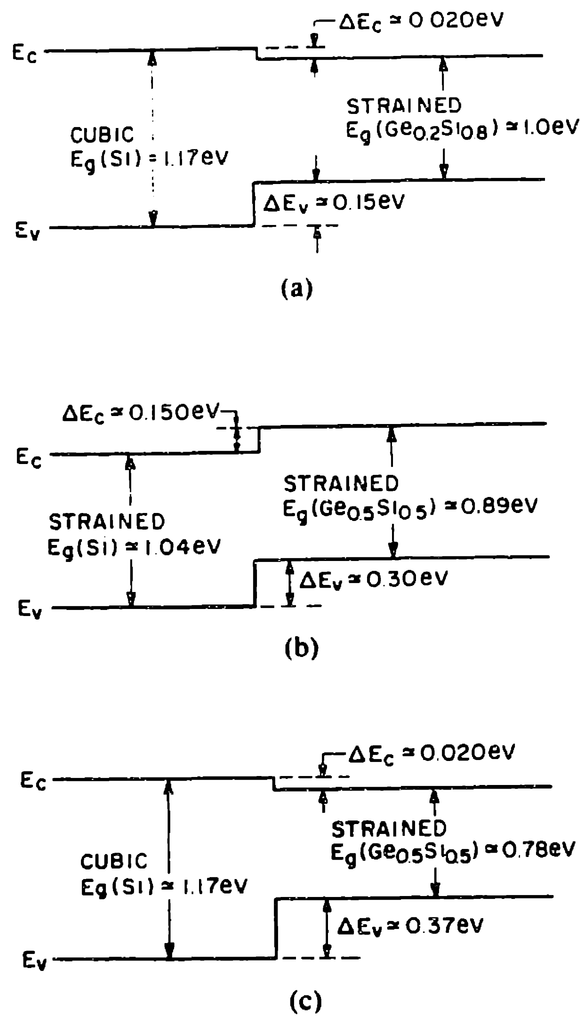

Figure 1.12: Band alignments for (a) $Si_{0.80}Ge_{0.20}/Si$ heterojunctions on (001) Si substrates, (b) $Si_{0.50}Ge_{0.50}/Si$ on (001)-$Si_{0.75}Ge_{0.25}$, and (c) $Si_{0.50}Ge_{0.50}/Si$ heterojunctions on (001)-Si [7].

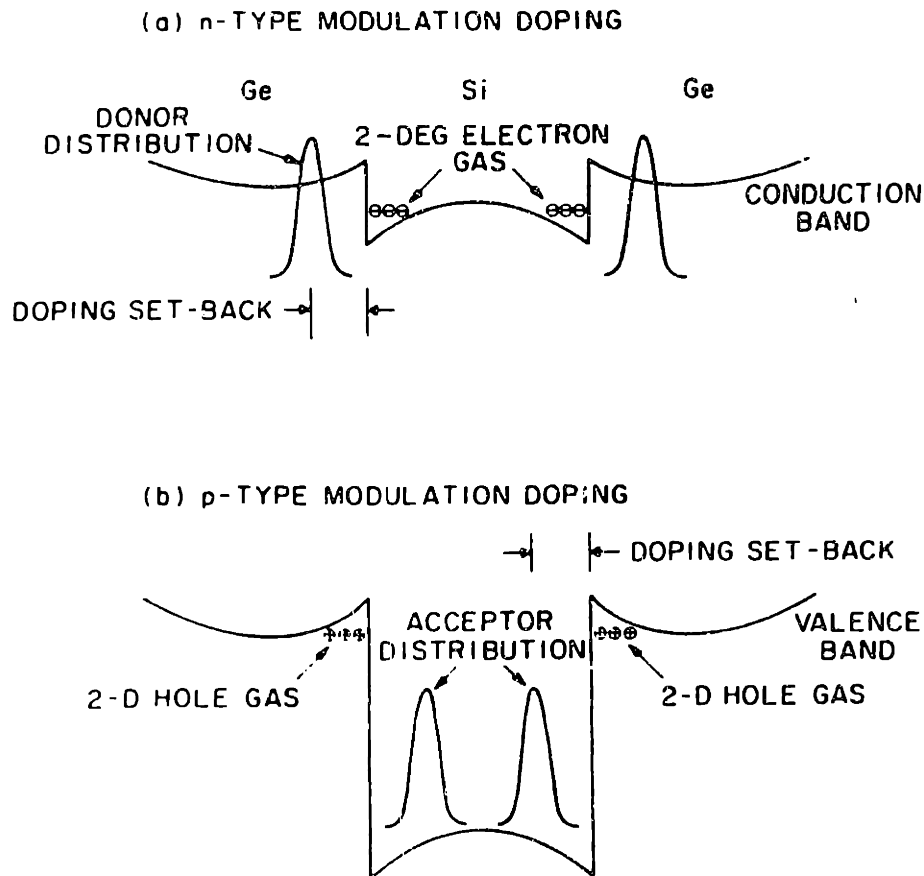

Figure 1.13: Modulation-doping of a $Si_{1-x}Ge_x$/Si heterostructure grown on (100) Si. (a) n-type modulation doping requires donor localization in $Si_{1-x}Ge_x$, and a two-dimensional electron gas is formed in Si. (b) p-type modulation doping requires acceptor localization in Si, and the two-dimensional hole gas is formed in $Si_{1-x}Ge_x$ [75].

are shown in Fig. 1.12 (a), (b), and (c), respectively. The band alignments in Fig. 1.12 (a) and (c) are Type-I, and that in Fig. 1.12 (b) is Type-II. The modulation doping of a $Si_{1-x}Ge_x$/Si heterostructures can be achieved by placing donors in the $Si_{1-x}Ge_x$ layer for n-type modulation-doping, or achieved by placing placing acceptors in the Si layer for p-type modulation-doping, as shown in Figure. 1.13 [75].

Because ionized impurity scattering is greatly reduced by modulation doping, carrier mobility increases. Enhanced mobility by $Si_{1-x}Ge_x$/Si modulation doping was first demonstrated for holes at Bell Laboratories [76] and for electrons at AEG and the Munich Technical University [77]. Since then, much of recent research effort in FETs have been focused on the Si/$Si_{1-x}Ge_x$ MODFET. However, taken as a whole, electron transport experiments on $Si_{1-x}Ge_x$ strained-layer heterostructure have thus far shown modest modifications in electron and hole mobilities. The effect of strain on the electron mobility, though still unexplained, appears to be the most promising as far as device applications are concerned. Very little of the potential of modulation-doping has been acheived in experiments so far. Progress is likely in this area with improvements in the quality of heteroepitaxy, particularly with regard to reductions in the concentration of defects and background dopant concentration which reduce the scattering of carriers [75].

1.3 Goal of This Thesis

The deposition of high quality $Si_{1-x}Ge_x$ epitaxial layers on Si substrates is crucial to the development of novel Si-based heterojunction devices. The major goal of this research is to examine novel materials technology for the growth of high-quality $Si_{1-x}Ge_x$/Si heterostructures using a very low pressure chemical vapor deposition (VLPCVD) reactor at MIT which allows deposition of low temperature ($\leq 800°C$) $Si_{1-x}Ge_x$ layers on Si with or without plasma enhancement. The development of

materials technology includes deposition and characterization of the grown films. Deposition of $Si_{1-x}Ge_x$ will take place with SiH_4 and GeH_4 as the process gases, AsH_3, PH_3, and B_2H_6 as the dopant gases with or without H_2 as a carrier gas. The flow rates, temperature, time, and surface cleaning techniques are reactor parameters that can be adjusted to optimize film quality. Characterization of structural quality and contamination can be used to provide feedback for optimizing reactor conditions or to study post-deposition properties of these materials. New deposition techniques are explored for $Si_{1-x}Ge_x/Si$ heteroepitaxial growth by VLPCVD at temperatures 570°C–750°C.

Besides the development of growth techniques for $Si_{1-x}Ge_x$, understanding the growth kinetics is essential to controlling the reactor parameters which allows the fabrication of desired devices. In particular, layer thickness, Ge and dopant profiles are important to post-deposition properties of $Si_{1-x}Ge_x/Si$ heterostructures and device performance. Therefore, growth kinetics concerning growth rate and Ge and dopant incorporation are investigated. The limits of critical thickness and two-dimensional growth in VLPCVD will also be explored.

In order that the devices based on $Si_{1-x}Ge_x$ strained layers can be successfully fabricated, it is very important to know if the grown film is stable or metastable and, if it is metastable, what restrictions are imposed on the thermal budget for device fabrication before strain relaxation starts to degrade device performance. Hence, the study of thermal stability of $Si_{1-x}Ge_x$ strained layers during post-deposition processing conditions will be emphasized in this research.

In brief, the overall goal of this research is to develop the novel technology for $Si_{1-x}Ge_x$ growth by VLPCVD, and understand the growth kinetics and thermal stability of $Si_{1-x}Ge_x$ strained layers.

Chapter 2

Experimental

2.1 Introduction

The experimental work consists of two parts: (i) very low pressure chemical vapor deposition of undoped and *in-situ* doped $Si_{1-x}Ge_x$ and Si layers on unpatterned and patterned Si wafers, and (ii) characterization of the deposited films. The feedback of the material characterization helps to understand the properties of the films for further applications and also helps to improve the process of epitaxial depositions. This chapter introduces the experiments involved in this research.

2.2 $Si_{1-x}Ge_x$ Heteroepitaxy and Annealing

The complete $Si_{1-x}Ge_x$ heteroepitaxial growth procedures include wafer patterning, *ex-situ* surface cleaning, *in-situ* surface cleaning, and very low pressure chemical vapor deposition; all are described in this section. In addition, procedures for thermal annealing post deposition are described too.

2.2.1 Wafer Patterning

Wafer patterning in this work involves wet-etching, LOCalized Oxidation of Silicon (LOCOS), and plasma-etching techniques carried out in Integrated Circuits

Laboratory, a class 10 cleanroom at MIT.

Wet-etching Isolation

Wafers were prepared by growing a 1000Å thermal oxide, patterning, and wet-etching in 3:1 BOE. After removing the photoresist in 3:1 H_2SO_4:H_2O_2, a 200Å oxide was grown to remove any residue surface defect and to protect the epitaxial window before deposition occurred. Wafers patterned by wet-etching shown in this thesis were prepared by Dr. C. Tsai.

LOCOS Isolation

The substrates were first thermally oxidized in dry O_2 and a 430 Å-thick stress relief oxide was formed, followed by 1500 Å LPCVD nitride deposition and UV photolithography patterning steps. Then, a 5100 Å thermal oxide was grown at 950°C and nitride was removed subsequently by wet etch. The process flow for LOCOS isolation is listed in Appendix A.

Plasma-etching Isolation

The substrates were first oxidized to grow 5100 Å field oxide at 950°C, followed by UV photolithography steps. The wafers were then plasma-etched (CF_4, H_2, and CFH_3 at 900W) to remove oxide and create windows. A 200 Å thermal oxide was grown in dry O_2 to remove any damages introduced by plasma etching and protect the windows for epitaxial growth from contamination. The process flow for plasma-etching is listed in Appendix B. Work in this part was assisted by Ken Liao.

2.2.2 Ex-situ Surface Cleaning

Prior to loading into the reactor for deposition, the oxide on the growth area was stripped in an HF dip, rinsed in deionized water, spin dried, and placed in an ultraviolet/ozone cleaning system for 5 min. The exposure to the ultraviolet light in ozone ambient reduces the surface carbon contamination and also forms an $\sim 10\text{\AA}$ protective oxide layer, which is subsequently removed by an *in-situ* Ar plasma sputtering. Before HF dip, wafers received RCA clean each week.

2.2.3 In-Situ Surface Cleaning

After loading into the reaction chamber, Si and $Si_{1-x}Ge_x$ layers are grown by a single-wafer, non-load lock, quartz halogen lamp heated VLPCVD reactor. The schematic of VLPCVD reactor is demonstrated in Figure 2.1. The detailed descriptions of the VLPCVD reactor have been described elsewhere [78]. In brief, the substrate resided against a high thermal mass silicon-coated SiC susceptor which is suspended between two RF electrodes in a quartz chamber. The SiC susceptor is used to improve the temperature uniformity across the silicon wafer. In addition, an electrical bias can be applied to the susceptor, independent of the RF electrodes. Evacuation of the reactor chamber is carried out using a 510 ℓ/s turbopump. A 13.56-MHz radio-frequency generator provides the power required to generate and sustain the plasma, while a dc power supply provides a negative bias to the susceptor to accelerate the ions toward the substrate during Ar sputter cleaning. The temperature was controlled by keeping the power supply to the heating lamps at a constant voltage. An infrared pyrometer, focused on the center of the wafer, is used to monitor the temperature.

After loading, the chamber is pumped down to approximately 2×10^{-7} Torr at room temperature and then subsequently baked at temperature between 750°C and 800°C for 1.5–2 hr with 50 sccm Ar flow. During bakeout, the UV ozone

Very-Low-Pressure CVD Reactor

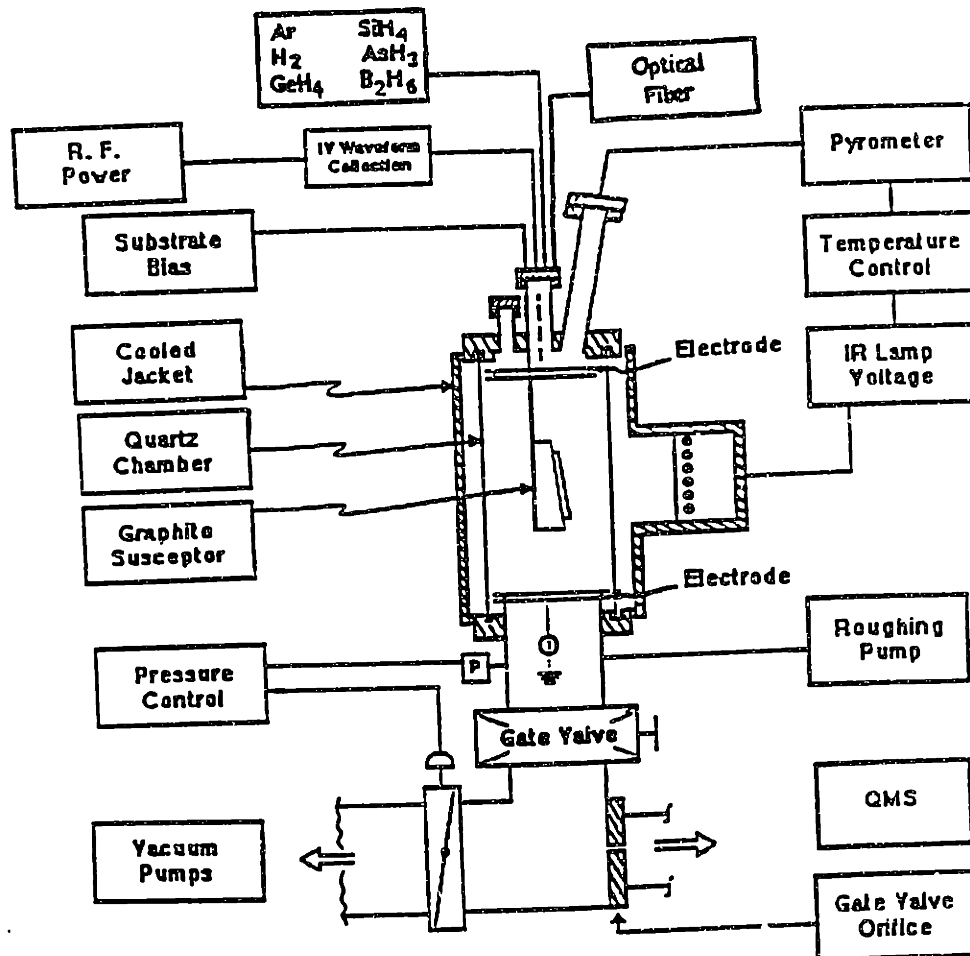

- quartz halogen lamp heating
- high thermal mass susceptor
- base pressure: 1×10^{-8} Torr (room temp)
- SiH_4, GeH_4, AsH_3/SiH_4, PH_3/SiH_4, B_2H_6/SiH_4
- deposition pressure ≤ 10 mTorr

Figure 2.1: Schematic of VLPCVD system.

oxide protects the Si surface from recontamination. When a "hot" base pressure of $\leq 2 \times 10^{-7}$ Torr is achieved, the wafer is *in-situ* Ar plasma sputtered to remove native oxide. The optimum sputter conditions at temperatures 750°C–800°C are -100V of dc bias and 2.5W of RF power for 15 minutes in 20 sccm Ar ($\sim$ 4m Torr).

2.2.4 Very Low Pressure Chemical Vapor Deposition

At the conclusion of the sputter or *in-situ* surface clean, the dc bias, RF power, and Ar gas are turned off and SiH_4 is introduced immediately into the chamber for growth of a Si buffer layer. After this Si deposition, SiH_4 is switched off for 30 seconds and $Si_{1-x}Ge_x$ epitaxial deposition commences immediately if $Si_{1-x}Ge_x$ growth occurs at the *in-situ* cleaning temperature. For depositions at temperature lower than 750°C, the lamp voltage is lowered and the flow of process gases was delayed for 20–40 minutes, depending on the desired growth temperature, to allow the susceptor to cool from the *in-situ* cleaning temperature.

In all depositions, SiH_4 and GeH_4 are used as process gases for $Si_{1-x}Ge_x$ growth with or without H_2 as a carrier gas. B_2H_6 and AsH_3 are employed for *in-situ* doping. In order to improve the Ge and dopant incorporation profile between two successive layers, process gases are distinguished for 30 seconds. While used, H_2 carrier gas is flowed continuously throughout the deposition process to reduce the gas turbulence when the process gases are switched. Details of $Si_{1-x}Ge_x$ VLPCVD will be described in following chapters.

2.2.5 Thermal Annealing

Thermal stability of $Si_{1-x}Ge_x$ strained layers were carried out by characterizing the samples received annealing at temperatures of 750 – 1100°C. Thermal annealing was conducted in Technology Research Laboratory (TRL), a class 10 cleanroom at MIT, in diffusion furnace. Samples were exposed to N_2 flow during annealing.

2.3 Materials Characterization

The deposited films are characterized by various techniques, including Nomarski optical microscopy, scanning electron microscope (SEM), ion-channeling/Rutherford backscattering spectrometry (RBS), secondary ion mass spectrometry (SIMS), transmission electron microscope (TEM), and double-crystal X-ray diffractometry (DCD), and Raman Scattering Spectrometry. The following sections will describe briefly the characteristics of these analytical tools.

2.3.1 Nomarski Optical Microscopy and Schimmel Etch

Differential interference contrast of Nomarski microscopy is a simple and versatile tool for observation of surface morphological variation of the epilayer. The magnifications of a Nikon optical microscope are 50X, 200X, 400X, and 1000X. Using the dark/bright field imaging techniques, the quality of the epilayer can be roughly estimated. In general, the shape, size, and density of the observed growth pits can be characterized to reflect the success or failure of the epitaxial growth and smooth morphology implies good film.

Chemical defect etching has been employed to monitor the dislocations in $Si_{1-x}Ge_x/Si$ system. With the aid of the differential interference contrast of Nomarski microscopy, the defects can be characterized more precisely. Schimmel etch was widely used to reveal the misfit dislocation segments at $Si_{1-x}Ge_x/Si$ interface and the threading parts of dislocation in $Si_{1-x}Ge_x$ layer. Nomarski microscope allows the observation of individual dislocation implying that the detection limit of $1cm^{-2}$ can be reached. The Schimmel etching solution is composed of 4 parts 48% HF and 5 parts 0.3M CrO_3 and the etching time is about 1 min at room temperature.

2.3.2 Scanning Electron Microscopy

SEM provides better lateral and depth resolution for examining the surface morphology of epilayer as the magnification can be increased up to 200KX. It allows the identification of two-dimensional or three-dimensional growth of $Si_{1-x}Ge_x/Si$ heterostructure and can be used for observing the nuclei clusters or polycrystalline $Si_{1-x}Ge_x$ on SiO_2 of pattern wafer.

2.3.3 Ion Channeling/Rutherford Backscattering Spectrometry

In RBS, a high energy beam of collimated helium ions is used to probe a sample. Impinged ions suffer nuclear collisions inside the sample and are backscattered. By analyzing the energy distribution of those ions that reflect backwards out of the sample, information on Ge composition and $Si_{1-x}Ge_x$ thickness may be obtained. In this research, the helium ions are singly charged and the ion energy is 2 MeV. The well collimated beam of He^+ ions is accelerated toward the sample along its normal direction and the backscattered ions are detected by a detector at near normal incident.

The evaluation of film quality was also carried out using the ion-channeling techniques on RBS. This technique consists of aligning the He^+ beam to a low-index direction of silicon (channeling direction, $< 100 >$ in this study) so that most of the beam is steered by the atomic potentials along the aligned direction. For $Si_{1-x}Ge_x$ strained layer on Si, the $< 100 >$ directions are identical for both. Disorder in the $Si_{1-x}Ge_x$ layers disrupts the channel and gives rise to an increase in backscattering yield with respect to a perfect crystal. Therefore, the quality of $Si_{1-x}Ge_x$ epilayer can be determined by the ratio of the channeling yield to the random yield which is obtained by averaging the backscattered yield over all directions few degrees, typically 7°, deviating from the channeling direction, i.e.

non-channeling directions. The measured ratio that indicates the quality of the epilayer is so called χ_{min}. For perfect Si and Ge crystal, χ_{min} is about 2.9% and 3.5%, respectively, depending on the collimation of the beam and the channeling direction.

2.3.4 Secondary Ion Mass Spectrometry

In SIMS, an epitaxial layer is eroded by the sputtering process and hence the relative abundance of the sputtered species provides a direct measurement of the composition of the layer that has been removed. In this work, SIMS was performed by Charles Evans and Associates using a Perkin Elmer 6300 SIMS. Ge profile, dopant profiles for B and As, and impurity profiles for C and O were generated using a Cs^{+} ion beam. Each sample was analyzed twice in order to obtain more accurate quantitative profils. The B, As, C, and O profiles were measured as negative secondary ion, with a Ge signal acquired as a layer marker. During the second analysis, Ge and Si were monitored as positive secondary ions. Conversion of ions counts to concentrations was accomplished by using relative sensitive factors derived from analysis of the standards. The depth scales were calibrated by measuring the analytical crater depth with a Dektak stylus profilometer.

2.3.5 Transmission Electron Microscopy

Cross-sectional transmission electron microscopy (XTEM) is used extensively to characterize the structural quality of the epitaxial layer(s) and the interfaces between different layers. To optimize the growth conditions, the results of XTEM is extremely valuable. XTEM is carried out using the electron beam oriented parallel to the growth plane such that the direct observation of the substrate, epitaxial layer(s), and interface(s) is possible.

Plan-view TEM is used for the study of thermal stability as it provides the top view of the interface(s) and allows the direct observation of misfit dislocations.

Both cross-sectional and plan-view TEM are performed using a JOEL 200CX which is a high-resolution microscope equipped with LaB_6 filament and is capable of 0.144nm line-to-line resolution and 0.3nm point-to-point resolution.

2.3.6 Double-Crystal X-ray Diffractometry

DCD is one of the most powerful tools for rapidly and nondestructively examining the layer thickness, compositions, and strain in epitaxial layers. In strained-layer system, the success of DCD for evaluating the structural quality relies primarily on the high strain sensitivity of the rocking curves. In this work, a Bede Model 300 double-crystal diffractometer is used which is characterized by 300mm axis separation and specimen scanning capability and provides precise determination of peak position and peak shape. The rocking curves are recorded in a (+,–) geometry using a (100) InP first crystal and Cu K_α radiation.

2.3.7 Raman Scattering Spectrometry

Raman scattering has been a powerful technique to characterize $Si_{1-x}Ge_x$/Si structures because it allows the measurement of strain. Furthermore, for superlattices, Raman studies also yields the information on confinement and interfacial disorder. For a $Si_{1-x}Ge_x$ layer grown on Si, there are three main peaks at around 300, 400, and 500 cm^{-1} corresponding respectively to Ge-Ge, Ge-Si, and Si-Si signals. The peak positions and the linewidth in $Si_{1-x}Ge_x$ depend on Ge fractional composition and strain. By comparing peak composition in the spectra from fully strained $Si_{1-x}Ge_x$ layer with those from partially relaxed thicker layers of the same composition we could quantitatively determine the strain in the relaxed layers. The comparison of line width qualitatively yields information about disorder, dislocation density, and inhomogeneous strain.

Chapter 3

VLPCVD/PECVD of $Si_{1-x}Ge_x$ at 750°C

3.1 Introduction

Heteroepitaxy of $Si_{1-x}Ge_x$ alloys on Si has attracted tremendous attention in recent years since they allow the fabrication of novel devices compatible with silicon processing technologies. Early experiments have demonstrated the commensurate growth of $Si_{1-x}Ge_x$ by molecular beam epitaxy (MBE) [13, 79]. Bean et al. have investigated the temperature ranges where two- and three-dimensional growth occurred [13]. At reduced temperature (T≤550°C), it was found that all alloy compositions could be grown smoothly on Si. More important, $Si_{1-x}Ge_x$ films with up to 50% Ge can be grown free of dislocations and the commensurate growth can be maintained for alloy layer thicknesses well beyond the predicted equilibrium values [18, 19], indicating metastable nature [47]. Some novel devices in the $Si_{1-x}Ge_x$/Si system produced by MBE have been demonstrated, including heterojunction bipolar transistors using a Si-Ge base layer [80]-[82], high electron mobility transistors [83], and optoelectronic devices [84].

In addition to MBE, recent progress with the epitaxial growth of $Si_{1-x}Ge_x$ on Si using other techniques, including limited reaction process (LRP) [29, 26],

ultrahigh vacuum chemical vapor deposition (UHVCVD) [27, 30] and rapid thermal chemical vapor deposition [35, 31] (RTCVD) have been reported. SiGe-based heterojunction bipolar transistors fabricated by LRP [85] and UHVCVD [86] have also been demonstrated. Of the processes proposed for $Si_{1-x}Ge_x$ epitaxial growth, CVD is of great interest since this technique appears to be compatible with manufacturing requirements such as high throughput, conformal coverage, and low cost.

In this chapter we report results of an investigation of the epitaxial growth of $Si_{1-x}Ge_x$ on (100) Si using a very low pressure ($\leq 10^{-2}$ Torr) chemical vapor deposition (VLPCVD) process at 750°C. Interrupted growth by gas switching was employed to reduce the compositional transition width of germanium. $Si_{1-x}Ge_x$ films have been grown commensurately with $x \leq 0.13$. The growth rate and germanium incorporation for a range of GeH_4:SiH_4 input ratios with varying total gas flow rate have been studied. We observed that the growth rate of $Si_{1-x}Ge_x$ alloys decreases with germanium content at 750°C. Our observation is in contrast with that reported in the literature [27, 29]. Flow rate dependence of germanium incorporation was also investigated.

3.2 Experiments

The substrates used were 100-mm, Czochraski-grown, p-type, 10-20 ohm-cm (100) silicon wafers. Mechanical damage introduced by wafer cutting and polishing was removed by the growth of a thermal oxide, nominally 1000$\AA$ thick. Prior to loading into the reactor, the oxide was stripped in an HF dip, rinsed in deionized water, spin dryed, and placed in an ultraviolet/ozone cleaning system for 5min. The exposure to the ultraviolet light in ozone ambient reduced the surface carbon contamination and also formed a $\sim 10\AA$ protective oxide layer, which was subsequently removed by an *in situ* argon plasma sputtering.

The reactor used for the epitaxial growth has been reported elsewhere [78]. The deposition system was a radiantly heated, single-wafer reactor with a 510 ℓ/s turbopump. The substrate resided against a silicon-coated graphite susceptor. A 13.56-MHz radio-frequency generator provided the power required to generate and sustain the plasma, while a DC power supply provided a negative bias to the susceptor to accelerate the ions toward the substrate during the argon sputter cleaning. The temperature was controlled by keeping the power supply to the heating lamps at a constant voltage. An infrared pyrometer, focused on the center of the wafer, was used to monitor the temperature.

After loading, the chamber was pumped down to (2-3) $\times 10^{-7}$ Torr at room temperature and then subsequently baked at 750°C for 1.5–2 hr with 50 sccm argon flowing. When a "hot" base pressure of $\leq 2 \times 10^{-7}$ Torr was achieved, the wafer was *in situ* argon plasma sputtered to remove native oxide. The optimum sputter conditions are -100V of DC bias and 2.5W of RF power for 15 min in 20 sccm argon ($\sim$ 4 mTorr). At the conclusion of the sputter, the DC bias, RF power, and argon gas were turned off and SiH_4 was immediately introduced into the chamber for growth of a silicon epitaxial layer 2400-3000 Å thick. After this silicon deposition SiH_4 was switched off for 30 seconds. A $Si_{1-x}Ge_x$ layer was then grown by introducing SiH_4 and GeH_4 after the 30 sec purge. To maintain a stable flow of gases, the flow rate of SiH_4 was kept constant for both Si and $Si_{1-x}Ge_x$ growth in the same run. Growth of $Si_{1-x}Ge_x$ layers were carried out by using 40, 20, 10, and 5 sccm SiH_4 with various GeH_4:SiH_4 ratios. SiH_4 and GeH_4 were introduced independently and the chamber pressure was 1-7 mTorr. The pumping speed was kept constant in this study. The deposition duration was varied with respect to the GeH_4 fraction to grow the $Si_{1-x}Ge_x$ layer commensurately. All thermal depositions (depositions without plasma enhancement) were carried out as described above except for the 40 sccm SiH_4 where there was no growth interruption and a silicon layer cap was grown following the deposition of $Si_{1-x}Ge_x$. For plasma enhanced

GeH_4 : SiH_4	20 sccm SiH_4	10 sccm SiH_4	5 sccm SiH_4
3%	commensurate $Si_{0.92}Ge_{0.08}$ (6min, 1240Å)	incommensurate $Si_{0.92}Ge_{0.08}$ (15min, 1700Å)	—
5%	commensurate $Si_{0.87}Ge_{0.13}$ (4min, 600Å)	incommensurate $Si_{0.88}Ge_{0.12}$ (10min, 1000Å)	—
8%	islanding (4min, 750Å)	islanding (7min, 600Å)	islanding $Si_{0.85}Ge_{0.15}$ (7min, 430±90Å)
12%	islanding (1min, 500Å)	islanding (4min, 800Å)	islanding (3.5min, 400Å)

Table 3.1: Growth conditions for $Si_{1-x}Ge_x$ growth at 750°C. Results obtained by SIMS and TEM are also shown.

depositions, a plasma was maintained throughout the SiH_4 exposure at nominal power level of 5 W. The deposition time is 1 min.

Structural characterization was performed by Nomarski optical interference contrast microscopy and planar and cross-sectional transmission electron microscopy (TEM). Thickness of $Si_{1-x}Ge_x$ was determined by cross-section TEM (XTEM). Sputter depth profile by secondary ion mass spectroscopy (SIMS) was utilized for chemical analysis of carbon and oxygen contamination. Germanium compositions of all films were measured by Rutherford backscattering spectroscopy (RBS) and SIMS. SIMS data are used in the table and plots.

3.3 Results

3.3.1 VLPCVD

Table 3.1 summarizes the material characterization results as a function of SiH_4 flow rate (20, 10, and 5 sccm) and GeH_4:SiH_4 input ratio (3, 5, 8, and 12 %). The entries in the table indicate whether the resulting films were commensurate, incommensurate, or whether islanding occurred, as well as the germanium content

in the films. The deposition time for $Si_{1-x}Ge_x$ growth and the corresponding thickness are indicated in parenthesis. The maximum thickness of islanding is also presented.

Figures 3.1(a) and (b) show XTEM micrographs of commensurate $Si_{0.92}Ge_{0.08}$ and $Si_{0.87}Ge_{0.13}$ heteroepitaxial layers grown at 20 sccm SiH_4 and 0.6 sccm GeH_4, and 20sccm SiH_4 and 1.0 sccm GeH_4, respectively. $Si_{1-x}Ge_x$ and Si layers are clearly distinguished as dark and light, respectively, in the bright field micrographs, indicating the commensurate nature. Plan-view TEM studies showed no dislocations; thus, the dislocation density of each film must be below the detection limit of 10^5 cm^{-2}. The smooth surface morphology of the strained layers examined by electron microscope and Nomarski optical interference contrast microscope confirmed that the heteroepitaxy occurred by two-dimensional growth.

No threading dislocations but only interfacial dislocations were observed in the incommensurate films, which suggests that the defect density is low within the deposited films and the the film thickness may not be far over the critical thickness. From Table 3.1, the critical thickness of $Si_{0.92}Ge_{0.08}$ was found to be between 1240Å (20 sccm SiH_4) and 1700Å (10 sccm SiH_4). We indicate the gas flow rates here since the different deposition time may result in different degree of thermal relaxation and thus different critical thickness at 750°C. Our observation is similar to that provided by Kasper et al. [79] who reported the critical thickness of $Si_{0.92}Ge_{0.08}$ grown at 750°C by MBE to be about 1000Å. The critical thickness of $Si_{0.87}Ge_{0.13}$ is found to be at least 600Å (20sccm SiH_4). Our previous investigation showed that in a 2400Å-Si/$Si_{1-x}Ge_x$/2400Å-Si/Si-substrate structure, the middle 2300Å-thick $Si_{0.97}Ge_{0.03}$ layer grown at 40sccm SiH_4 and 0.4sccm GeH_4 is commensurate.

As the GeH_4:SiH_4 ratio increased, island formation occurred in the $Si_{1-x}Ge_x$ growth, as indicated in Table 3.1. Fig. 3.2 presents XTEM images of $Si_{1-x}Ge_x$ formed by three-dimensional growth. Germanium incorporation in the film grown at 5 sccm SiH_4 and 0.4 sccm GeH_4 was analyzed directly from the island-coalesced

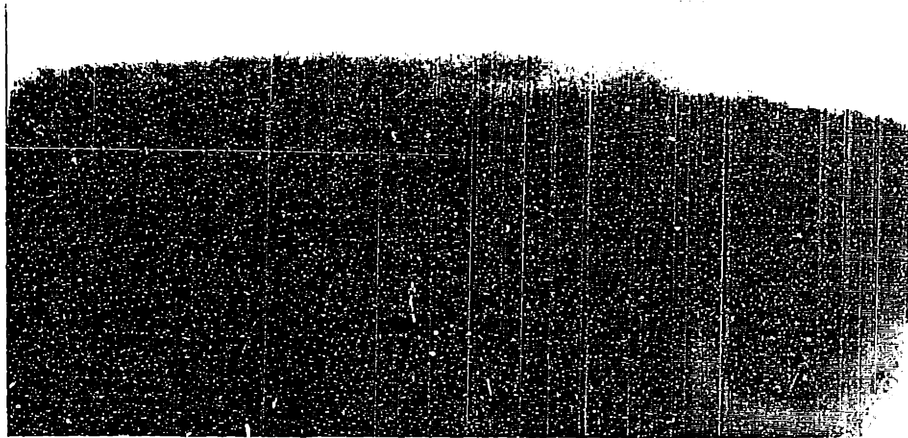

(a)

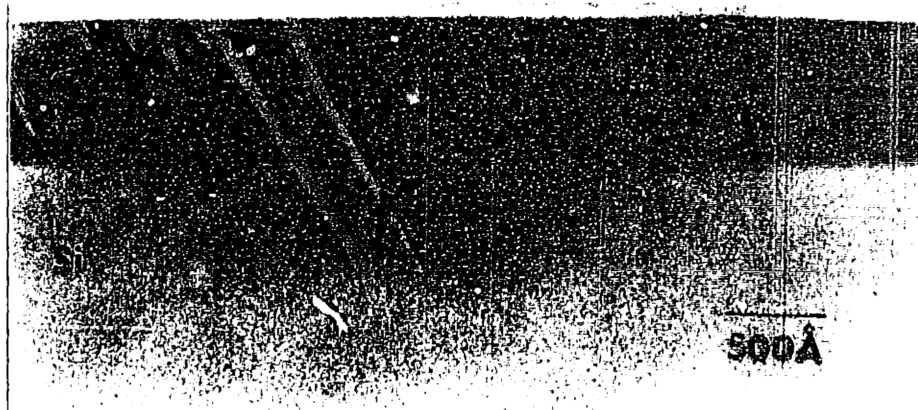

(b)

Figure 3.1: XTEM bright field images of 750°C smooth and commensurate $Si_{1-x}Ge_x$ films formed by two-dimensional growth: (a) x=0.08 and (b) x=0.13.

(a)

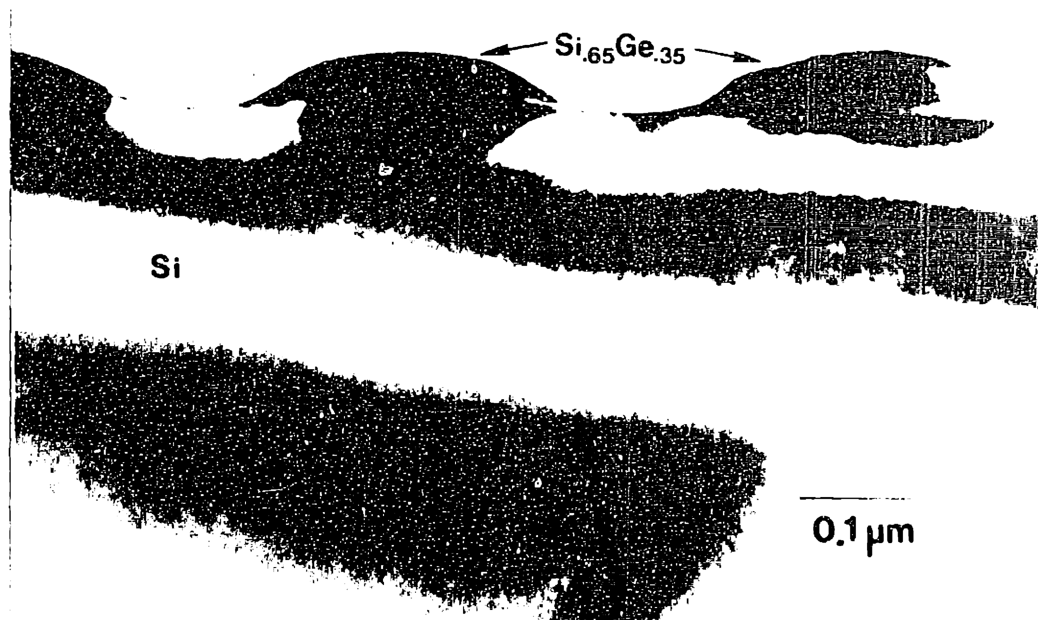

(b)

Figure 3.2: XTEM bright field images of 750°C rough $Si_{1-x}Ge_x$ islands formed by three-dimensional growth: (a) x=0.15 and (b) x=0.35, measured.

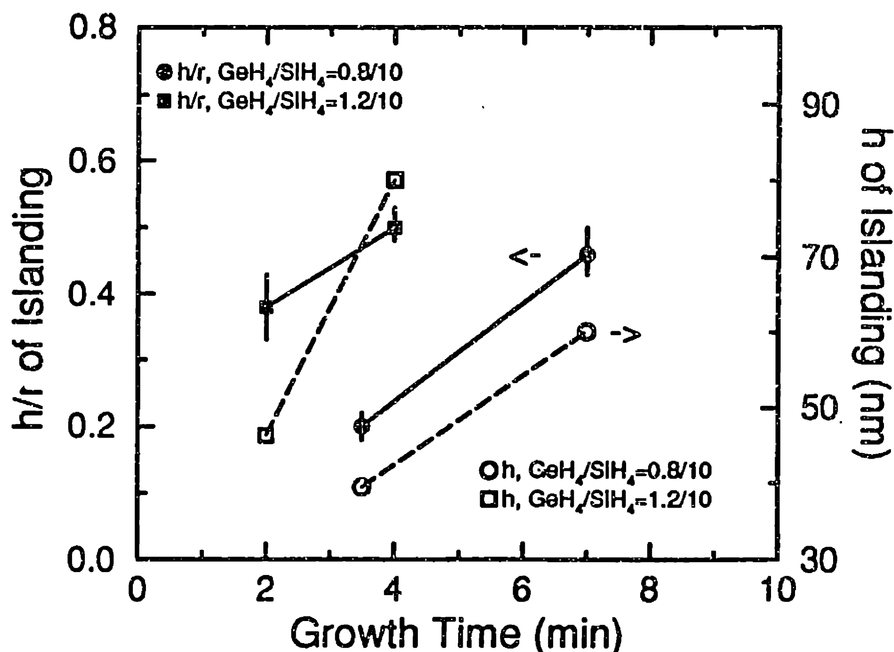

Figure 3.3: The measured ratios of height to radius of three-dimensional $Si_{1-x}Ge_x$ islands. The actual value of islanding height is also shown.

layer of about 430±90Å. While germanium composition in the individual $Si_{0.65}Ge_{0.35}$ islands was obtained from another sample where deposition time was increased under the same SiH_4 and GeH_4 flow rates to allow islands to coalesce to a certain thickness so that the measurements of thickness and composition were allowed.

The tendency of three-dimensional growth in the $Si_{1-x}Ge_x$/Si system has been reported previously by Bean et al. where the island formation was related to the high energy associated with the $Si_{1-x}Ge_x$/Si interface or the strain energy in $Si_{1-x}Ge_x$ [13]. In this work, the transition from two-dimensional to three-dimensional growth at 750°C took place when the germanium content is about 13–15% (see Table 3.1). Our result is similar to the MBE data reported by Bean et al. [13]. It is interesting to note in Fig. 3.3 that the measured ratio of height (h) and radius (r) of three-dimensional island (in semisphere) increases as germanium composition increases, and, for a given germanium composition, this ratio

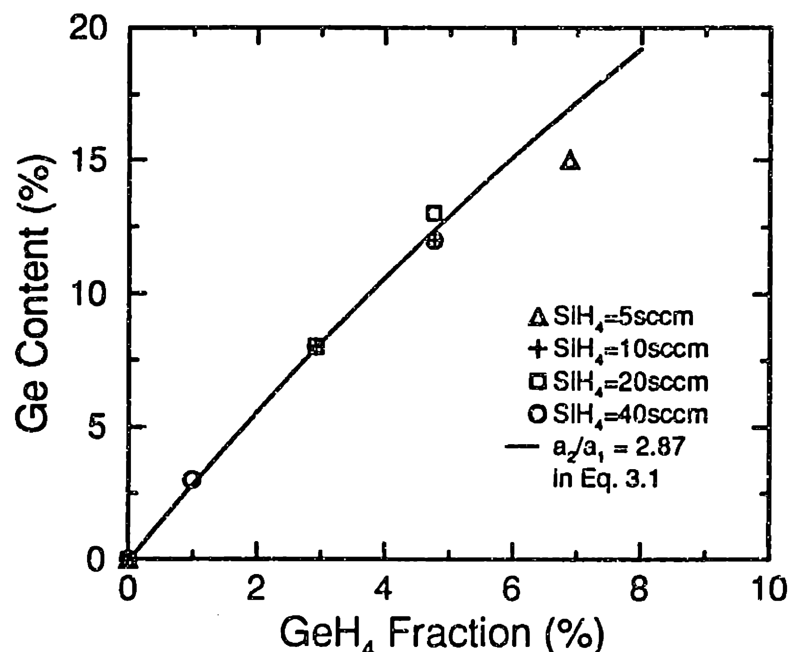

Figure 3.4: Germanium content as a function of GeH_4:SiH_4 input ratio by VLPCVD.

increases with the growth time. Figure 3.3 also presents the actual heights of the observed islands measured by XTEM, and the actual radii of the islands can also be extracted from the height/radius (h/r) ratios shown in Fig 3.3.

Figure 3.4 shows germanium content in the $Si_{1-x}Ge_x$ film as a function of GeH_4:SiH_4 input ratio. Figure 3.4 indicates that the germanium content increases with the GeH_4:SiH_4 ratio and that it is not significantly affected by the total gas flow rate for a given ratio of GeH_4:SiH_4. Our investigation is consistent with that reported by Suzuki et al. [87] who used an LPCVD process for $Si_{1-x}Ge_x$ deposition at 750°C and 1×10^{-2} Torr, and proposed the following empirical equation for the germanium content x:

$$x = \frac{a_2 \times y}{a_1 \times (1 - y) + a_2 \times y} \tag{3.1}$$

where y is the GeH_4 fraction, and the coefficients a_1 and a_2 include the contribution of the dissociation efficiencies of SiH_4 and GeH_4 and the sticking coefficients of Si

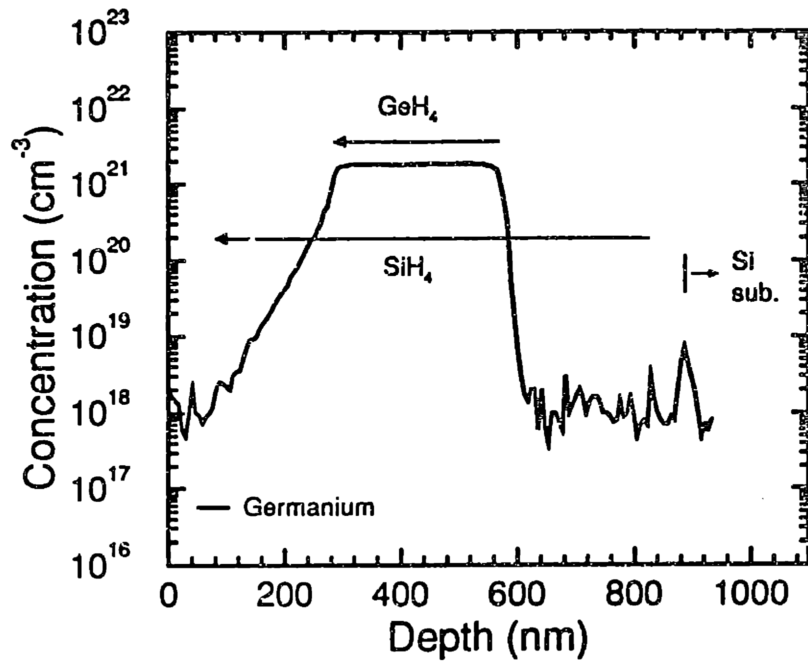

(a)

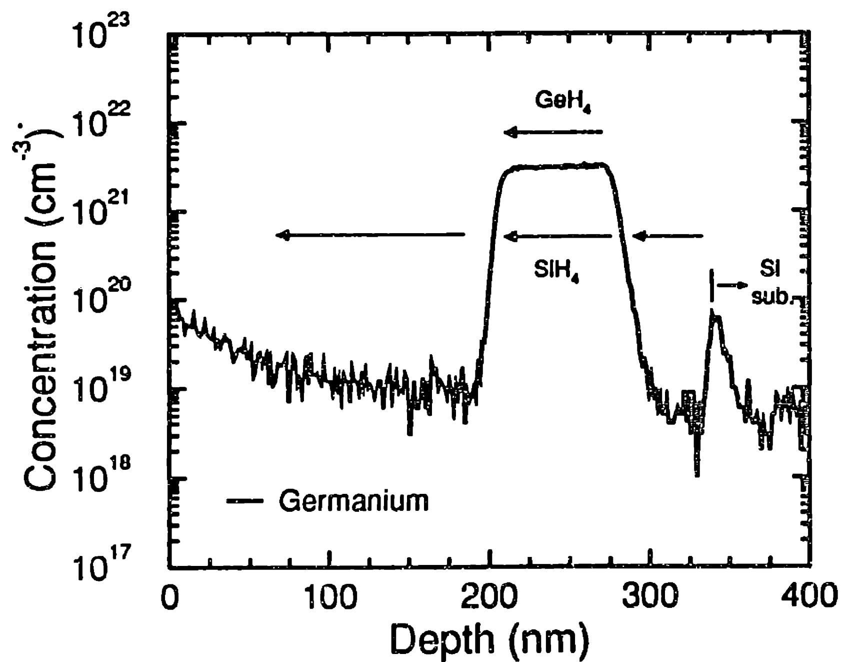

(b)

Figure 3.5: SIMS depth profile of germanium incorporation: (a) without growth interruption (b) with growth interruption between the deposition of $Si_{1-x}Ge_x$ and Si capped layer.

and Ge atoms, respectively, on the growing surface. Equation 3.1 has been plotted as a solid line in Figure 3.4 with a_2/a_1=2.87. In the case of LPCVD, a_2/a_1 was determined to be 2.7 [87].

Since the abruptness of $Si_{1-x}Ge_x$/Si interface is crucial to the heterojunction devices, it is important to examine how the control of gas flows affects the abruptness of germanium profile. Figure 3.5 (a) and (b) compare the probed germanium depth profiles using SIMS for the Si/$Si_{1-x}Ge_x$/Si deposition with and without growth interruption. Depositions without growth interruption were simply performed by switching in and out GeH_4 gas while keeping SiH_4 flowing to start and terminate the $Si_{1-x}Ge_x$ deposition. On the other hand, deposition with growth interruption means both SiH_4 and GeH_4 were turned off for 30 sec allowing the chamber evacuated before growing $Si_{1-x}Ge_x$ and Si cap layer. The turn-on transients between these two growth ways show no difference. However, remarkable change was observed in Figure 3.5 (a) and (b); with the growth-interruption one exhibiting much abrupter germanium turn-off profile. Clearly, between the end of $Si_{1-x}Ge_x$ deposition and the beginning of capping Si deposition, a certain amount of GeH_4 remained in the reaction chamber which affected the germanium turn-off profile. The transition of germanium profile between $Si_{1-x}Ge_x$ and Si strongly depends on how fast the residual GeH_4 can be purged. The gradual transition of germanium profile in Fig. 3.5 (a) suggests the GeH_4 remnant in the chamber was incorporated into the consecutive Si epitaxial deposition, but the germanium tail can be easily removed by terminating the growth process for 30 sec between two consecutive depositions, as exhibited in Fig. 3.5 (b).

SIMS measurements have also been carried out to evaluate the contaminants of carbon and oxygen in the samples. These measured impurities are less than 8ppm in the epitaxial $Si_{1-x}Ge_x$ layers. A typical SIMS depth profile is shown in Figure 3.5 (a). SIMS also reveals that the abrupt germanium profile has been achieved by interrupted growth using gas switching without introducing interfacial

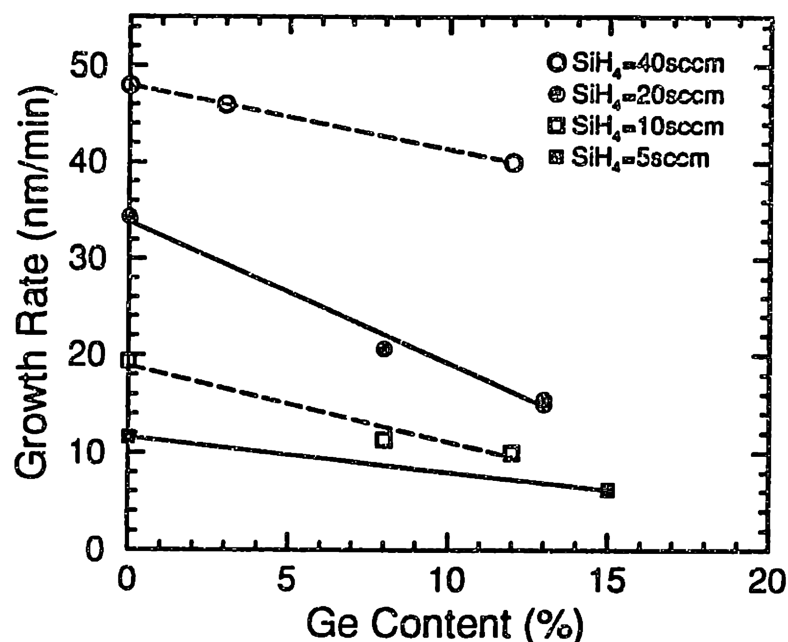

Figure 3.6: $Si_{1-x}Ge_x$ growth rate as a function of Ge content by VLPCVD.

contamination (not shown).

The growth rates of $Si_{1-x}Ge_x$ layers measured as a function of the germanium content are plotted in Figure 3.6. The data show that the growth rate of $Si_{1-x}Ge_x$ layer decreases as the germanium content (and/or the GeH_4:SiH_4) increases. The same behavior was also observed in the growth of $Si_{1-x}Ge_x$ at 700°C. These results appear to disagree with the published work [27, 29].

3.3.2 PECVD

Figure 3.7 exhibits XTEM images for PECVD $Si_{1-x}Ge_x$ heteroepitaxial layers. The germanium incorporation as a function of GeH_4 fraction is summarized in Fig 3.8, and it is found that, for a given GeH_4 fraction, the amount of incorporated germanium atoms is less in plasma enhanced CVD than in thermal CVD. The empirical equation (3.1) was employed to fit the measured data with a_2/a_1 = 1.33 and 2.98 for plasma enhanced CVD and thermal CVD, respectively, as shown

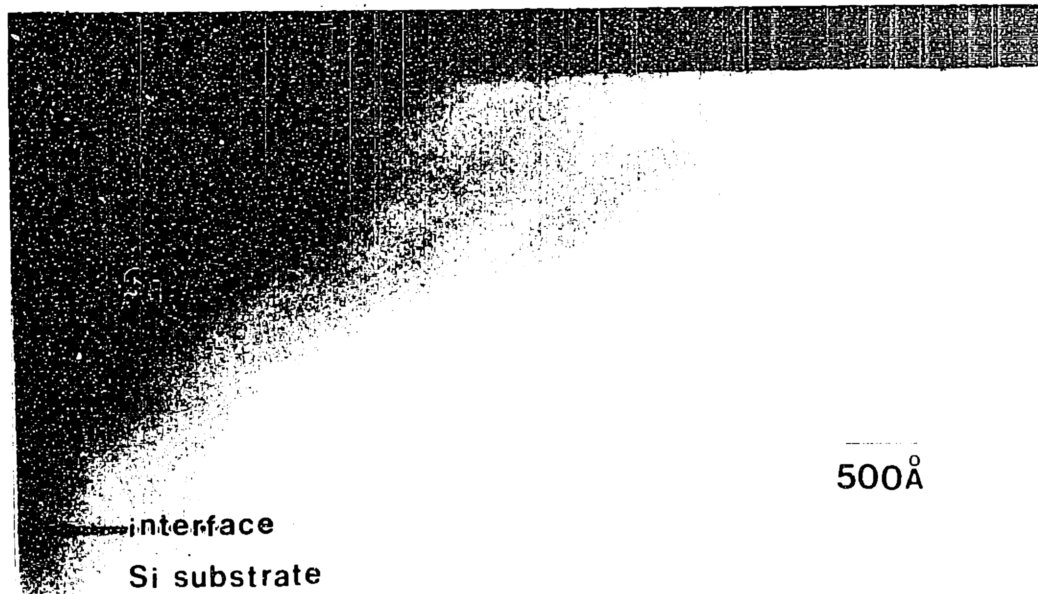

(a)

(b)

Figure 3.7: XTEM bright field images of 750°C $Si_{1-x}Ge_x$ grown by PECVD: (a) x=0.16 (two-dimensional growth) and (b) x=0.35 (three-dimensional growth).

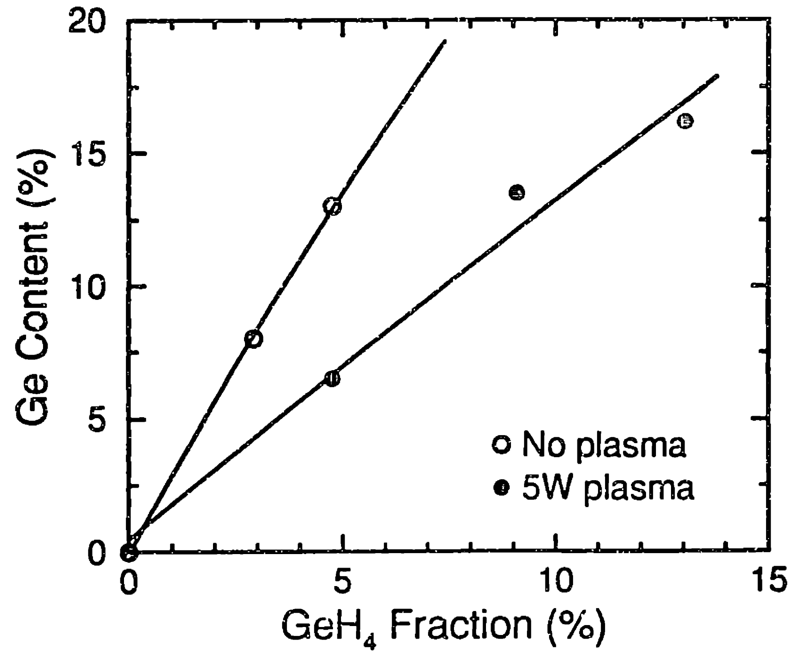

Figure 3.8: Ge content as a function of GeH_4:SiH_4input ratio by VLPCVD and PECVD. SiH_4 = 20 sccm.

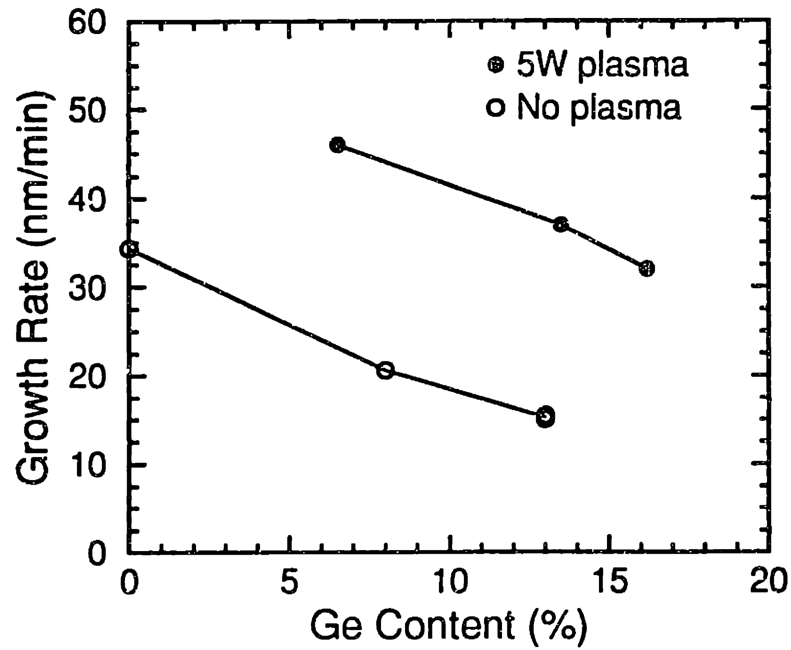

Figure 3.9: $Si_{1-x}Ge_x$ growth rate as a function of Ge content by VLPCVD and PECVD. SiH_4 = 20 sccm.

in Fig. 3.8. Differing from the results reported by Suzuki et al. [87] in which a_2/a_1 corresponds to 0.55 for rf power of 300 W at 10 mTorr, we found a_2/a_1 in equation (3.1) to be 1.33 with 5 W rf power at 3 mTorr. Clearly, the dissociation coefficients of SiH_4 and GeH_4 and sticking coefficients of Si and Ge, both included in a_2 and a_1, depend on plasma power. The increase of plasma power leads to lower germanium incorporation when GeH_4 fraction is fixed.

In addition to the impact of plasma power on germanium incorporation, we also see the increase of growth rate due to plasma enhancement, as exhibited in Fig. 3.9. The use of 5 W plasma power leads to an increase of $\sim$ 30 nm/min in $Si_{1-x}Ge_x$ growth rate. The increase of $Si_{1-x}Ge_x$ growth rate is consistent and is independent of Ge composition, but the overall growth rate of $Si_{1-x}Ge_x$ still decreases as germanium content increases.

3.4 Discussion

We have shown above that, by using VLPCVD at 750 °C, commensurate growth of a uniform $Si_{1-x}Ge_x$ layer with $x \geq 0.13$–0.15 was restricted by three-dimensional growth without plasma enhancement. Though it is difficult to conclude from limited depositions whether or not plasma enhances two-dimensional growth, our present results suggest that plasma might help to reduce islanding, because smooth film with 16% germanium atoms have been obtained and islanding films containing 34% germanium appeared to be more smooth compared to that with 35% germanium grown by thermal CVD. A possible explanation is that plasma enhnaced the growth rate and reduced the carbon and oxygen contamination which may act as island nucleation sites.

At 750°C, commensurate $Si_{1-x}Ge_x$ films ($x \leq 0.13$) can be grown up to 2–4 times the thickness predicted value by thermodynamical [20], and mechanical [18] equilibrium theories, indicating their metastable nature and the existence of kinetic

barriers to dislocation formation [47]. The interfacial abruptness and cleanliness obtained at low base pressures ($\leq 2 \times 10^{-7}$ Torr) are encouraging. This suggests that processing gases can be changed for heteroepitaxial deposition during the growth interruption without significant recontamination.

The interesting observation of the decrease in germnaium incorporation due to an increased plasma power can be realized from the decomposition and condensation behaviors of the reactive gases and their adsorbed species on the layer surface. In thermal VLPCVD, the dissociation of source gases, SiH_4 and GeH_4, mostly occurs on the surface of the growing layer and their decomposition is assisted by thermal energy provided by the heating lamps. Since the bonding of Ge-H is weaker (more readily to dissociate) than that of Si-H, it is expected that more germanium will be incorporated into the layer. Plasma provides a means in addition to the thermal energy to dissociate the source gases. In Suzuki's paper [87], it was reported that the dissociation efficiencies of reactive gases were proven to be 90% both for SiH_4 and GeH_4 by monitoring of QMS (quodrupole mass spectrometer), and, therefore, it was considered that the deposition of $Si_{1-x}Ge_x$ was mainly brought about by the atomic Si and Ge generated by the ion bombardment in plasma. This differs from thermal CVD where we believe deposition occurs due to the decomposition of SiH_4 and GeH_4 adsorbed on the surface. Thus, since the dissociation efficiencies of both SiH_4 and GeH_4 are high in PECVD, the incorporation ratio of germanium into to silicon is determined by their sticking coefficients on the surface. Since germanium is more weakly bonded (more readily to desorb or leave the surface before being incorporated) to the surface than Si, it is reasonable to see that, when both SiH_4 and GeH_4 have similar dissociation efficiencies, the ratio of Ge/Si in the solid is lower than that in the gas for thermal CVD. Because the dissociation efficiencies of SiH_4 and GeH_4 are near unity in Suzuki et al.'s work (rf power of 300 W), it is thus not unexpected to see that a_2/a_1 is lower than 1 in their study.

In our case (rf power of 5 W), we believe the decomposition efficiencies of source gases are much lower than that measured by Suzuki et al. due to lower plasma power (5W), and both thermal energy and ion bombardment might contribute to the dissociation of SiH_4 and GeH_4. In consequent, the ratio of Ge and Si readily to be incorporated is thought to be higher than that in high rf power case. As a result, we observed more germanium incorporated and the ratio of a_2/a_1 is higher than that presented by Suzuki et al..

We observed that the growth rate of $Si_{1-x}Ge_x$ layer decreased with increasing germanium content. This observation for $Si_{1-x}Ge_x$ growth rate in the range of $x \leq 0.13$ is in disagreement with the literature [27] where the same processing gases (SiH_4 and GeH_4) were used and the growth rate of $Si_{1-x}Ge_x$ is reported to increase monotonically with germanium content. In both cases, two-dimensional growth is expected. Meyerson et al. proposed that germanium adatoms act as desorption centers, lowering the activation energy for hydrogen desorption from the growing layer, and enhancing the reactivity of silane through the creation of bare adsorption sites [27]. Our results are probably related to the reaction-limiting step differing from the limit of hydrogen desorption at higher temperatures [36]. The kinetics of $Si_{1-x}Ge_x$ deposition will be revisited in Chapter 5.

The growth rate promoted from plasma is clear in Fig. 3.9. Plasma enhancement provided an alternative deposition pathway which operates in parallel with the existing thermal incorporation process [88]. In VLPCVD at reduced temperatures, SiH_4 gas-phase pyrolysis is inhibited and the growth proceeds through heterogeneous decomposition of SiH_4 on the surface, followed by diffusion and incorporation. Plasma excitation of reactive gases allows the regeneration of the gas-phase pyrolysis mode at lower temperatures [88]. In this way, plasma may transfer some portion of the growth process control back into the gas phase, which leads to enhanced adsorption of SiH_4 and GeH_4 and increased deposition rate. In addition to enhanced adsorption, continuous ion bombardment from plasma may

also contribute to the deposition. Since there is a flux of ionized species directed at the growth surface, an energy is provided to enhance the adatom mobility and encourage the diffusion and incorporation of surface atoms [88]. Thus, due to the enhanced adsorption and mobility from plasma-assisted SiH_4/GeH_4 decomposition and continuous ion bombardment, the $Si_{1-x}Ge_x$ deposition rate is increased. Note that, though plasma assists the growth process, the deposition rate of $Si_{1-x}Ge_x$ still decreases with increasing with germanium content, as shown in Fig 3.9. Moreover, the slopes of the growth rate as a function of germanium are similar for both thermal and plasma-enhanced CVD. This might imply that the mechanism responsible for germanium-reduced deposition rate at 750°C is the same for both plasma-enhanced and thermal CVD and is not restored by plasma. The constant increase in $Si_{1-x}Ge_x$ growth rate ($\sim$ 30 nm/min) for germanium compositions of 0.06 – 0.16 led by plasma suggests that plasma consistently contributes to the deposition rate in a way independent of the germanium content and of the mechanism that degrades the deposition rate when germanium is increased.

In this work, it is also worthy to note that the growth rate of islanding increased with the GeH_4 fraction as indicated in Table 3.1. The energy associated with the lattice mismatch of $Si_{1-x}Ge_x$ and Si may affect the contact angle, thickness, density, and coalescence of $Si_{1-x}Ge_x$ islanding. Therefore, growth in a three-dimensional manner may have a different germanium dependence than two-dimensional growth. Our speculation is supported by the data presented in Fig 3.3. Since the ratio of height to radius increases with both growth time and germanium content, it is likely that, when the energy between $Si_{1-x}Ge_x$ and Si is too high, islands tend to grow faster in the direction of the height to reduce the contact area or surface energy between $Si_{1-x}Ge_x$ and Si and to release more rapidly the misfit strain energy within $Si_{1-x}Ge_x$ islands. Thus, the growth rate of $Si_{1-x}Ge_x$ layer resulted from three-dimensional mode and island coalescence may be more complicated than the layer-by-layer-growth case.

3.5 Conclusion

We have demonstrated the deposition of commensurate $Si_{1-x}Ge_x$ layers on silicon with x up to 0.13 at 750°C by the use of a VLPCVD technique. TEM results showed that the transition of $Si_{1-x}Ge_x$ deposition from two-dimensional to three-dimensional growth occurred when x is 0.13–0.15. The amount of germanium incorporated in the solid is independent of the total gas flow rate for a given GeH_4:SiH_4 ratio in the very low pressure ambient. The measured growth rate of $Si_{1-x}Ge_x$ layers was found to decrease with increasing germanium content at 750°C. We also showed that the interruption of growth by gas switching can be inserted within the VLPCVD process to achieve interfacial abruptness for heteroepitaxy on silicon without recontamination. Finally, $Si_{1-x}Ge_x$ VLPCVD and PECVD were compared, and it was found that, for a given GeH_4/SiH_4 gas ratio, the incorporation of germanium decreased with raising plasma power. Similar to silicon homoepitaxial growth, plasma was observed to promote the deposition rate of $Si_{1-x}Ge_x$ heteroepitaxy compared to thermal CVD. However, the growth rate of $Si_{1-x}Ge_x$ still decreased with the increase of germanium composition, suggesting the use of plasma did not overcome the mechanism that led to the growth rate degradation caused by germanium.

Chapter 4

VLPCVD of $Si_{1-x}Ge_x$ at 570 – 700°C

4.1 Introduction

In previous chapter, we observed that the germanium range for two-dimensional growth at 750°C using VLPCVD is limited within ~ 15%. Thus, as suggested by Bean et al. that, although island formation is energetically favored in $Si_{1-x}Ge_x$ growth on Si, three-dimensional growth can be avoided by lower temperature deposition where atomic surface migration lengths are so short that macroscopic islands cannot form [13]. Moreover, it is well recognized that the limit of coherent growth or commensurate growth is defined by a critical thickness which depends on growth conditions such as germanium composition and profile, impurity level, and deposition temperature. Early work carried out by Bean et al. also showed that, at low temperatures, $Si_{1-x}Ge_x$ strained layer can be grown to a thickness far exceeding the criterion of thermodynamic or mechanical equilibrium theories without strain relaxation and metastable strained layer forms [13]. The encouraging progress that promises the deposition of strained films with greater thickness for more flexible device design and application is due to the existence of a kinetic barrier, which opposes dislocation nucleation and glide, to strain relaxation at low

temperatures.

To achieve smooth strained-layer growth with higher germanium contents and with greater thickness, the purpose of the experiments considered in this chapter is to examine the structure quality as well as carbon and oxygen contamination in $Si_{1-x}Ge_x$ and silicon films grown at temperatures much lower than 750°C, i.e., 620 and 570°C, by very low pressure chemical vapor deposition (VLPCVD). Surface cleaning techniques for these low temperature depositions (570°C - 700°C) were examined for reducing impurity contamination. Deposition of $Si_{1-x}Ge_x$ on patterned substrates were also investigated.

4.2 Experiments

All structures described in this chapter were grown by VLPCVD. The Si substrates were (100) silicon, 10 – 20 Ω-cm phosphorus doped, deposition on unpatterned or blanket substrates, the Si substrates were prepared by growing 1000 Å thermal oxide to remove residual surface damages. Prior to loading into vacuum, the substrate was dipped into a 25:1 HF solution to strip the 1000 Å oxide, rinsed in deionized water and spin dried. Next, the substrate was exposed to a UV ozone for 5 minutes to reduce surface carbon contamination and form a protective oxide of ~ 10 Å for bakeout. Substrate was then loaded into the VLPCVD system and the chamber was baked for 1.5 hour. When a chamber pressure of $\sim 1\times10^{-7}$ Torr was achieved, the substrate was *in-situ* sputtered to remove the 10 Å protective oxide before epitaxial growth was initiated.

In order to minimize carbon and oxygen concentrations in the grown films at very low pressure, we employed two different ways of cleaning techniques for comparison with our previous VLPCVD work [89]. For $Si_{1-x}Ge_x$ depositions at 620°C, the bakeout and *in-situ* clean were performed at 775°C, followed by a 1400Å Si deposition. The susceptor temperature was then reduced to 620°C in a

35-minute growth interruption. The optimum sputter conditions at 775°C are 2.5 W of rf power for 15 minutes in 20 sccm Ar (~ 4 mT) with susceptor biased to -100 V_{dc}. In the case of $Si_{1-x}Ge_x$ depositions at 570°C, bakeout and surface clean took place at 700°C. The optimized *in-situ* clean at 700°C consisted of a 3 W 5 sccm Ar/80 sccm H_2 (1 mT/10 mT) plasma for 60 minutes with susceptor zero biased. At the conclusion of sputtering, the susceptor was allowed to cool from 700°C to 570°C in a duration of 45 min. Different from 620°C depositions, a Si buffer layer was grown at 570°C instead of at the cleaning temperature (700°C). All depositions were carried out using 20 sccm SiH_4 with or without GeH_4 in an 80 sccm H_2 carrier gas.

Finally, once the limit of oxygen and carbon contamination is determined for low temperature deposition, we have grown $Si_{1-x}Ge_x$ layers on LOCOS and plasma-etch oxide patterned substrates at 675°C to reduce impurity levels and to examine $Si_{1-x}Ge_x$ deposition issues on patterned substrates. Previous VLPCVD $Si_{1-x}Ge_x$/Si heterostructures grown on patterned wafers prepared by chemical etching [89] were further characterized for studying the pattern sensitivity of $Si_{1-x}Ge_x$ growth kinetics at 625°C.

Structural quality of the as-grown samples was characterized using cross-sectional electron transmission microscopy (XTEM), double-crystal X-ray diffraction (DCD), and a dilute Schimmel etch (4 parts of 48% and 5 parts 0.3M CrO_3 for 1 min at room temperature). Scanning electron microscopy (SEM) were employed to examine the surface morphology. Thickness of $Si_{1-x}Ge_x$ layers were determined by XTEM and Rutherford backscattering spectrometry (RBS). Ge compositions were measured by RBS and secondary ion mass spectrometry (SIMS). SIMS was also utilized for probing carbon and oxygen impurity profiles.

	Deposition		Si buffer/Si-substrate interface	
in situ clean	Si buffer	$Si_{1-x}Ge_x$	Carbon (cm^{-3})	Oxygen (cm^{-3})
775°C	775°C	620°C	4×10^{18}	2×10^{18}
700°C	700°C	700°C	8×10^{19}	1×10^{19}
700°C	625°C	625°C	1×10^{20}	4×10^{19}
700°C	570°C	570°C	8×10^{19}	2×10^{20}
	Deposition		$Si_{1-x}Ge_x$ bulk	
in situ clean	Si buffer	$Si_{1-x}Ge_x$	Carbon (cm^{-3})	Oxygen (cm^{-3})
775°C	775°C	620°C	8×10^{17}	6×10^{17}
700°C	700°C	700°C	2×10^{17}	4×10^{17}
700°C	625°C	625°C	9×10^{17}	4×10^{17}
700°C	570°C	570°C	4×10^{17}	1×10^{19}

Table 4.1: Summary of SIMS data for the concentrations of carbon and oxygen impurities existing at the Si/Si-substrate interface and within $Si_{1-x}Ge_x$ layer for varied surface cleaning conditions and $Si_{1-x}Ge_x$ deposition temperatures.

4.3 Results

4.3.1 $Si_{1-x}Ge_x$ Deposition on Blanket Wafers

Table 4.1 summarizes the carbon and oxygen peaks at the Si/Si-substrate interface as well as their contents within $Si_{1-x}Ge_x$ layer for varied surface cleaning and deposition conditions. Measurements from $Si_{1-x}Ge_x$/Si multilayer structures grown at 700 and 625°C [89] are also presented for comparison. Table 4.1 exhibits that 15 min Ar sputter at 775°C led to lower impurity levels at the initial interface compared to that resulted from 1 hour Ar/H_2 sputter. To decouple the residual carbon and oxygen remaining on the substrate surface after *in situ* cleaning and the carbon and oxygen recontamination during a temperature ramp subsequent to 775°C surface clean, an epi-Si buffer layer was inserted between substrate and $Si_{1-x}Ge_x$ layer The effects of temperature ramp and deposition temperature on carbon and oxygen contamination are summarized from the data of Table 4.1, and oxygen present within $Si_{1-x}Ge_x$ layer was found to be independent of deposition

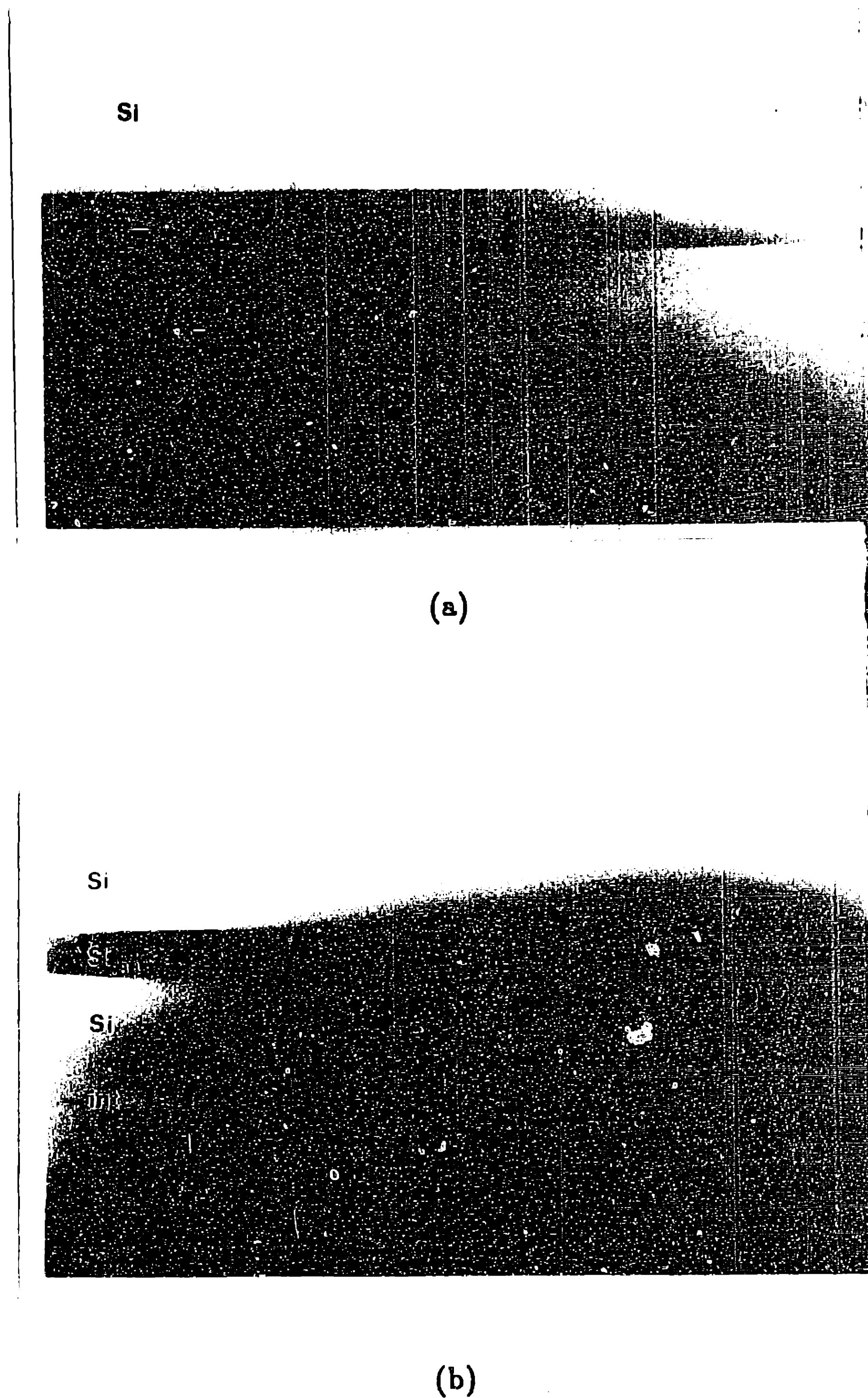

Figure 4.1: XTEM micrographs of (a) $Si/Si_{0.87}Ge_{0.13}/Si$ and (b) $Si/Si_{0.84}Ge_{0.16}/Si$ deposited at 620°C. SiH_4=20sccm, H_2=80scm, and GeH_4=0.75 and 1.00 sccm, respectively, for (a) and (b).

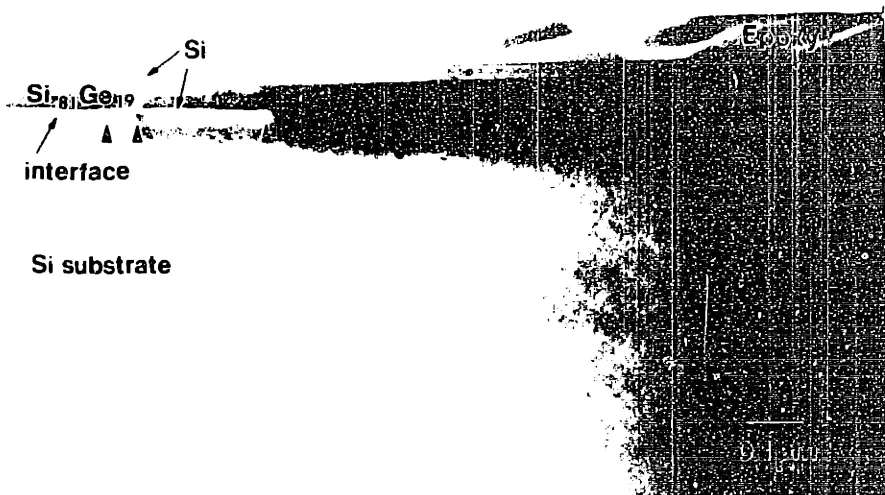

(a)

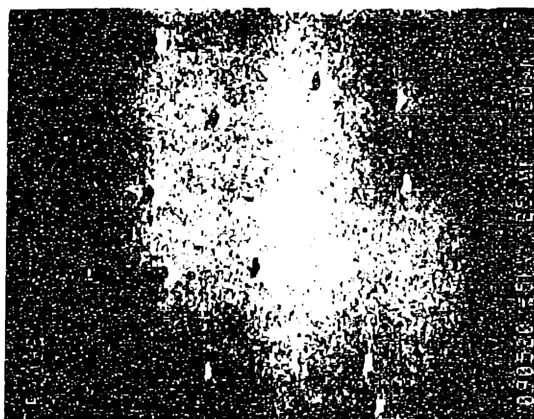

(b)

Figure 4.2: (a) XTEM and (b) SEM micrographes of $Si/Si_{0.81}Ge_{0.19}/Si$ deposited at 570°C. SiH_4=20sccm, H_2=80scm, and GeH_4=1.00 sccm.

temperature at 700°C and 620°C, while a considerable amount of oxygen (10^{19} cm^{-3}) appeared in the 570°C $Si_{1-x}Ge_x$ film. Since oxygen peak at the Si/Si-substrate interface of 570°C film (Table 4.1) is also high compared to that in 625°C films after receiving the same surface treatment at 700°C (Ar/H_2 sputtering), we speculate that in our VLPCVD system oxygen contamination becomes a major problem at low temperatures. However, it is not clear from Table 4.1 how carbon incorporation was affected by growth temperature.

The structural quality of as-grown $Si/Si_{1-x}Ge_x/Si$ heterostructures have been characterized by XTEM. Figures 4.1 (a) and (b) show that $Si_{1-x}Ge_x$ (x=0.13 and 0.16) and Si cap layer of high perfection have been attained at 620°C. However, misfit dislocations were observed in $Si/Si_{0.81}Ge_{0.19}/Si$, as shown in Fig. 4.2 (a), heterostructure grown at 570°C. The surface morphology of the dislocated $Si_{0.81}Ge_{0.19}/Si$ is exhibited in Fig. 4.2 (b). To determine the transition point of two-dimensional and three-dimensional growth at 620°C in VLPCVD, Ge has been increased up to 0.26 and islanding structure was observed. Figure 4.3 (a) and (b) show XTEM and SEM micrographs of $Si_{0.84}Ge_{0.26}$ deposited on Si substrate.

The results of Ge incorporation from $Si/Si_{1-x}Ge_x/Si$ sandwiched structures grown at 620 and 570°C from gas mixtures of GeH_4 and 20 sccm SiH_4 diluted in 80 sccm H_2 are presented in Fig. 4.4. The measured thickness of the epitaxial $Si_{1-x}Ge_x$ layer as a function of growth time for deposition temperatures of 620 and 570°C was investigated and shown in Fig. 4.5. Density of misfit dislocation measured from Schimmel etched 620°C film with varied $Si_{1-x}Ge_x$ thickness is also indicated. No incubation time was observed in the present work. Thus, the growth rate was calculated assuming no induction period for $Si_{1-x}Ge_x$ deposition on Si, as shown in Fig. 4.6. Figure 4.5 also implies that the growth rate of $Si_{1-x}Ge_x$ was not affected by misfit dislocations below density of 10^6 cm^{-2}. The growth rate data show a peak at intermediate Ge composition at 620°C and a monotonic increase in growth rate with Ge up to 21% was measured at 570°C.

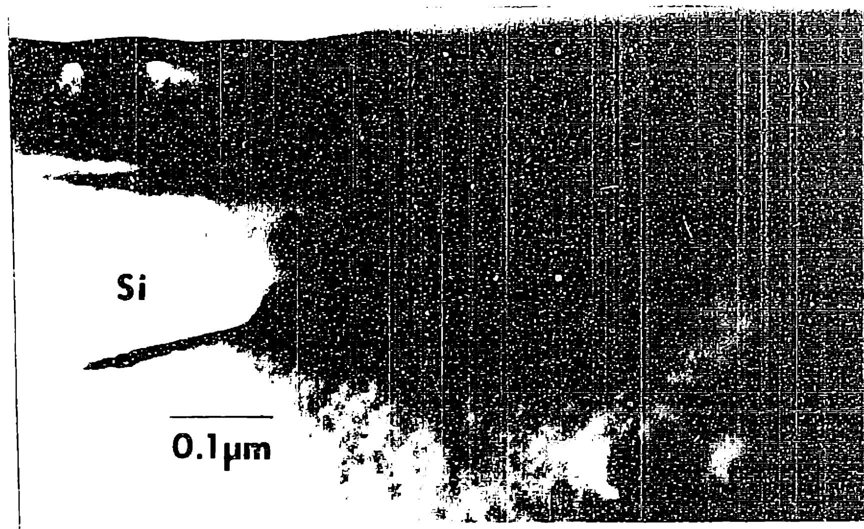

(a)

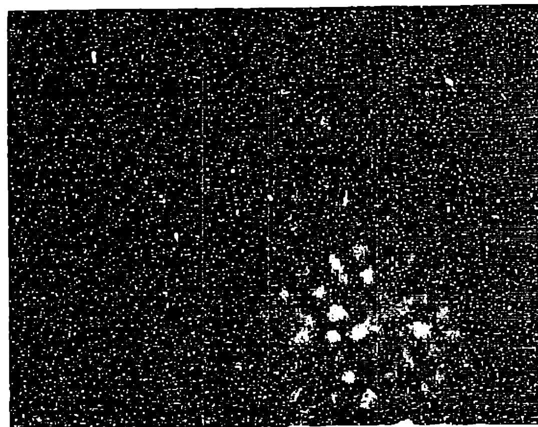

(b)

Figure 4.3: (a) XTEM and (b) SEM micrographs of $Si_{0.84}Ge_{0.26}$ deposited on Si substrate.

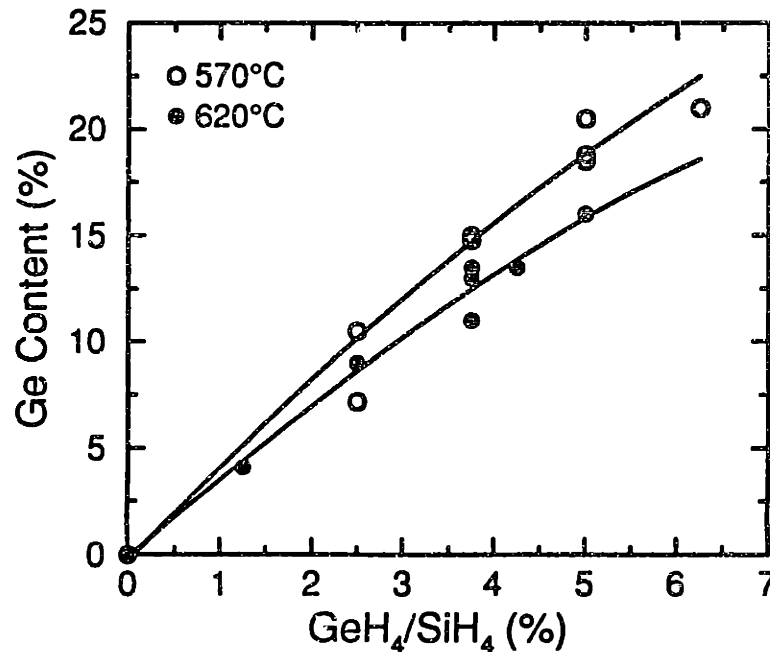

Figure 4.4: Ge content as a function of GeH_4/SiH_4 ratio at 620 and 570°C measured from $Si/Si_{1-x}Ge_x/Si$ sandwiched structures.

4.3.2 $Si_{1-x}Ge_x$ Deposition on Patterned Wafers

Figure 4.7 (a) shows a $Si_{1-x}Ge_x$ single layer grown on LOCOS patterned 10 × 20 μm epitaxial windows for 5 min. For 5 min deposition, $Si_{1-x}Ge_x$ strained layer was grown selectively in the epitaxial window with no polycrystalline layer or nuclei formed on the oxide, while polycrystalline $Si_{1-x}Ge_x$ layer was observed for the deposition time greater than 7 min by SEM. Figure 4.7 presents the thickest $Si_{1-x}Ge_x$ layer we have grown on LOCOS patterned Si substrate, and, although the growth time of 30 min produced $Si_{1-x}Ge_x$ layer of 3625Å-thick, no extended defects such as misfit dislocation or stacking fault was seen by XTEM in the 10 × 20 μm area. To compare the depositions on substrates patterned by different methods, we also characterized the structural quality of $Si_{1-x}Ge_x$ grown on oxide isolated 20 × 10 μm epitaxial windows prepared by plasma etch. In Fig. 4.8 (a), XTEM micrographs demonstrate selective $Si_{1-x}Ge_x$ strained-layer deposition (deposition

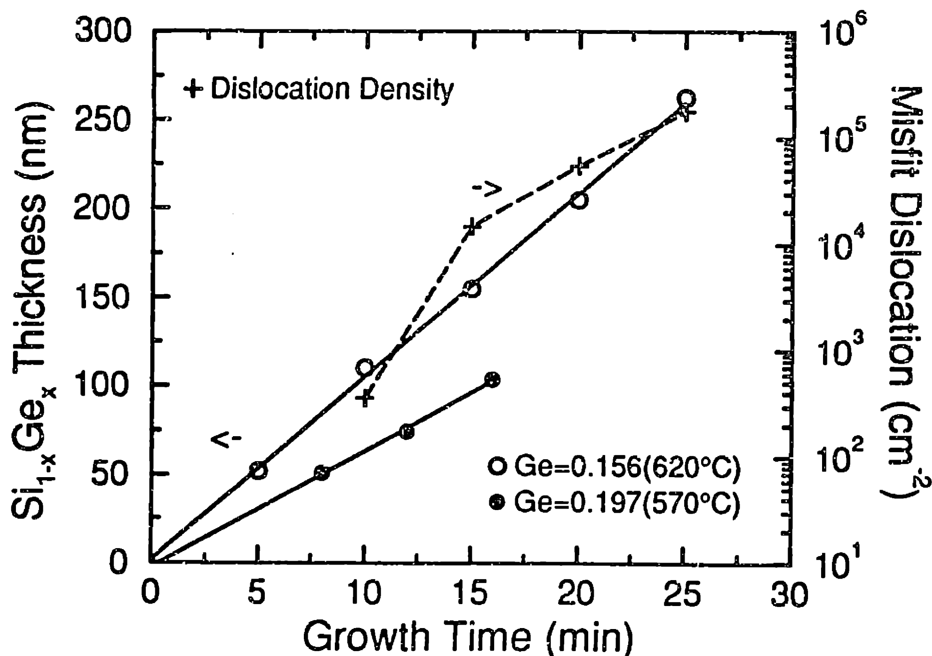

Figure 4.5: Measured thickness of $Si_{1-x}Ge_x$ deposited at 620°C and at 570 °C for various deposition time. In all cases, $Si_{1-x}Ge_x$ was capped with a Si film. Also indicated is the misfit-dislocation density in $Si/Si_{1-x}Ge_x/Si$ (x=0.156) structures with varied $Si_{1-x}Ge_x$ thickness observed by Normaski micrograph after 1 min Schimmel etching.

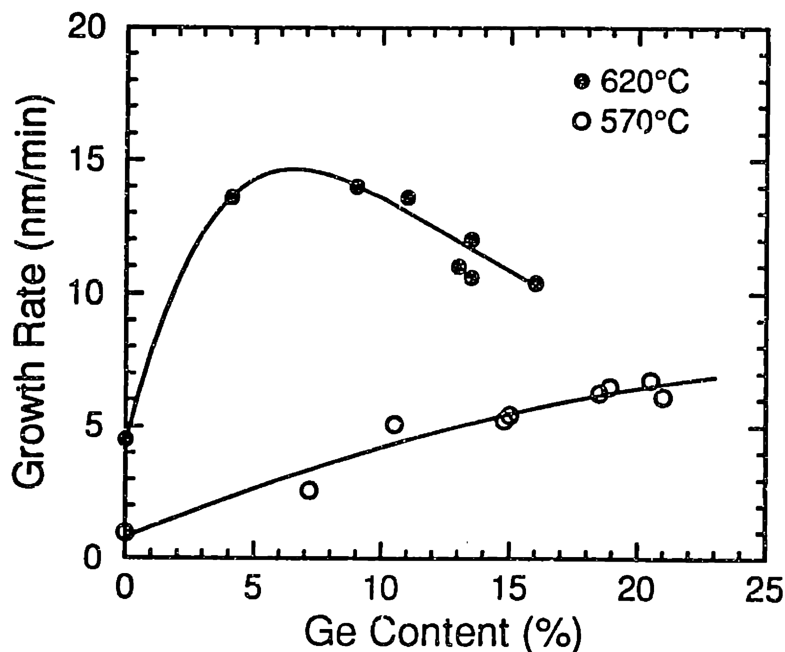

Figure 4.6: $Si_{1-x}Ge_x$ epitaxial growth rate as a function of Ge composition at 620 and 570°C.

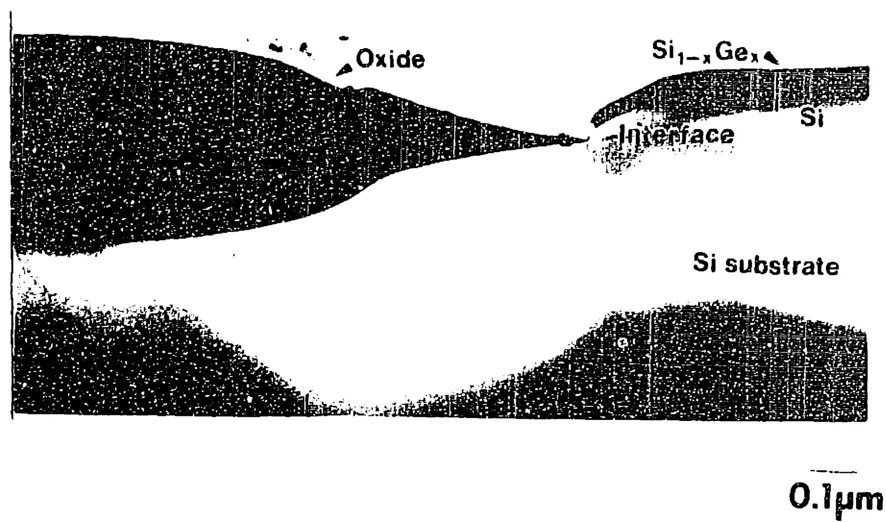

(a)

(b)

Figure 4.7: XTEM micrographs of $Si_{1-x}Ge_x$ layer grown on LOCOS patterned substrates: (a) deposition time = 5 min, (b) deposition time = 30 min.

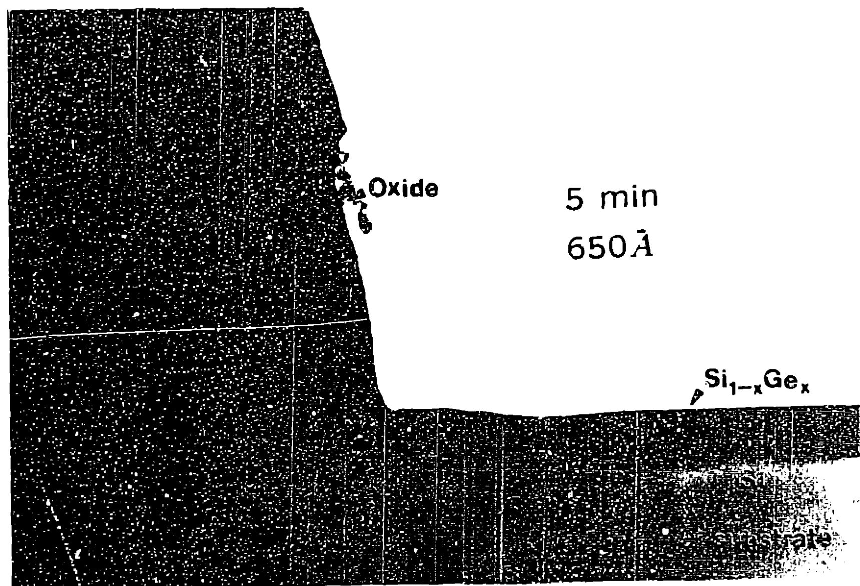

(a)

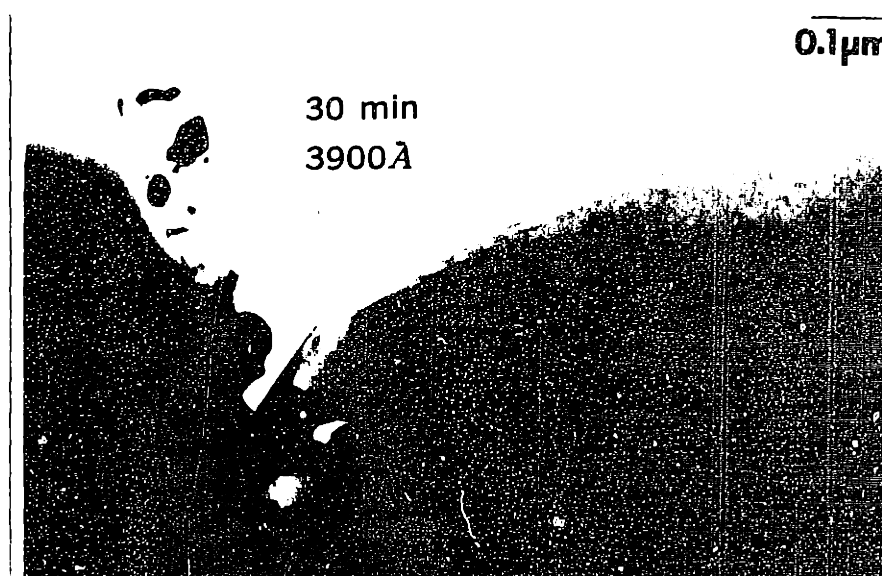

(b)

Figure 4.8: XTEM micrographs of $Si_{1-x}Ge_x$ layer grown on plasma-etch oxide patterned substrates: (a) deposition time = 5 min, (b) deposition time = 30 min.

time = 5 min). However, in contrast to the LOCOS case, 30 min deposition on plasma-etch substrate leads to strain relaxation in $Si_{1-x}Ge_x$ layer in the window. It is interesting to note that the sidewall of epi-layer/oxide/poly-$Si_{1-x}Ge_x$ plays an important role in the relaxation of $Si_{1-x}Ge_x$ strained layer. Unlike the interface of $Si_{1-x}Ge_x$/LOCOS-oxide where the contact of $Si_{1-x}Ge_x$ layer and the bird beak of the oxide is very limited (Fig. 4.7 (b)), the trench etched by plasma leads to larger boundary area of $Si_{1-x}Ge_x$ and oxide and poly-$Si_{1-x}Ge_x$; therefore, it would not be surprised to find the $Si_{1-x}Ge_x$ layer grown in plasma-etched trench is less stable than in LOCOS patterned window because the potential defect sources near the sidewall might assist in dislocation generation.

Figure 4.9 (a) and (b) demonstrate XTEM micrographs of $Si_{1-x}Ge_x$/Si multilayer structures deposited on a 10 × 20 μm window and a 5 × 5 mm window prepared by wet etching. From SIMS (Fig. 4.10), the modulation of Ge incorporation in the $Si_{1-x}Ge_x$ layers by the GeH_4/SiH_4 gas ratio is evident.

4.4 Discussion

4.4.1 $Si_{1-x}Ge_x$ Deposition on Blanket Wafers

Since the demands for low temperature Si and $Si_{1-x}Ge_x$ epitaxy require a highly perfect and impurity free surface, we have explored the optimum way to prepare an atomically clean surface prior to Si and $Si_{1-x}Ge_x$ low temperature epitaxial growth for VLPCVD. It is well known that deposition at low temperatures is crucial for defect-free $Si_{1-x}Ge_x$ film. Previous work on VLPCVD carried out using Ar/H_2 sputtering proved that good epitaxial layer can be produced at temperatures below 700°C. However, Table 4.1 suggests a cleaner interface can be achieved by Ar sputtering. Because the base pressures for *in situ* cleaning at 775°C and 700°C in the VLPCVD reactor were almost the same, the higher carbon and oxygen levels from one-hour Ar/H_2 sputter at 700°C was considered to be caused by the

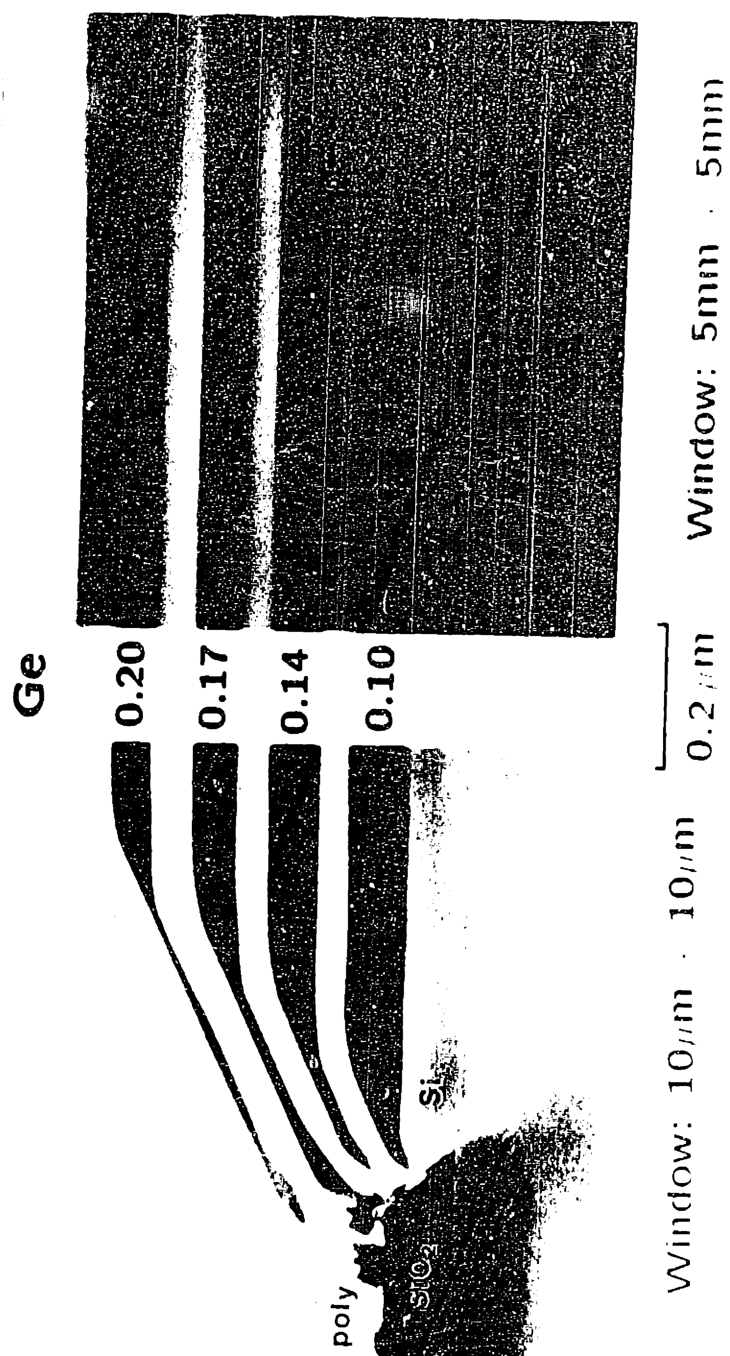

Figure 4.9: XTEM micrographs of $Si_{1-x}Ge_x/Si$ multilayer structures grown on oxide pattered substrates prepared by chemical etching. $Si_{1-x}Ge_x$ and Si layers were grown on 10 × 10 μm and 5 × 5 mm as indicated.

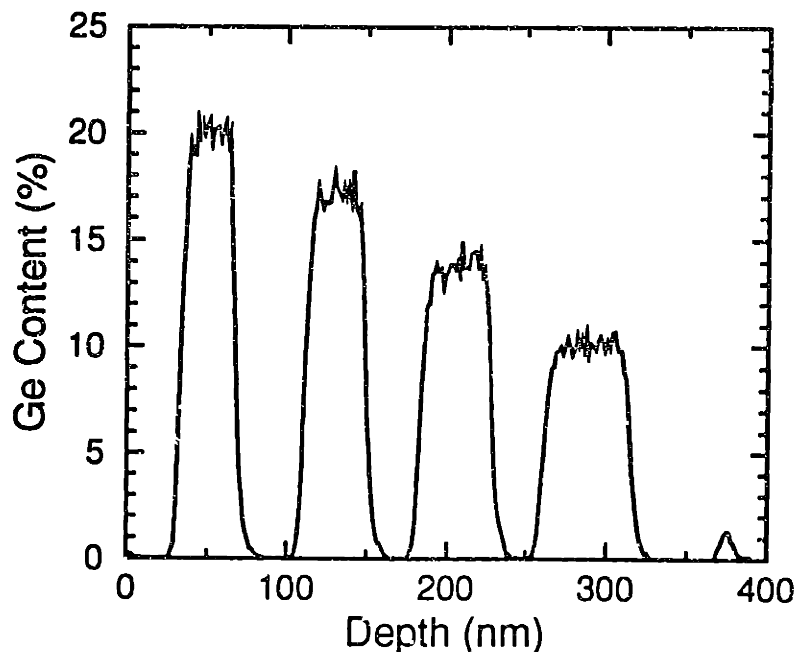

Figure 4.10: SIMS depth profile of 625°C multilayer structure. All layers had a 5 min deposition time.

incorporation of impurities from ambient and was enhanced by plasma accelerated toward the substrate during the longer sputtering time.

Though a cleaner surface may be prepared by Ar sputtering at 775°C, to grown at $Si_{1-x}Ge_x$ layers at temperatures < 775°C, the susceptor temperature has to be lowered. In our VLPCVD reactor, the Si substrate resides on a SiC-coated graphite susceptor of low thermal mass which provides DC bias for plasma sputtering and helps to improve temperature uniformity.

Hence, an interruption in the deposition process is unavoidable for the susceptor to cool from cleaning temperature to a lower temperature, and, during system cooling, surface recontamination may occur. The surface recontamination as well as the purity of Si and $Si_{1-x}Ge_x$ layer grown at different temperatures following 775°C surface cleaning have been examined systematically and are demonstrated in Fig. 4.11. Fig. 4.11 (a) shows the carbon and oxygen peak concentrations at the

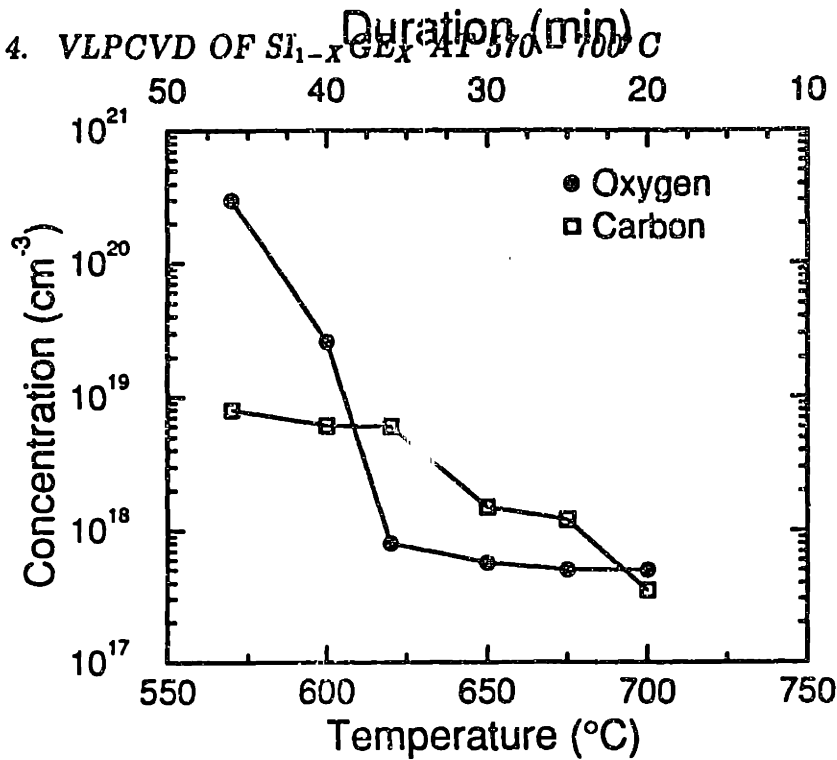

(a)

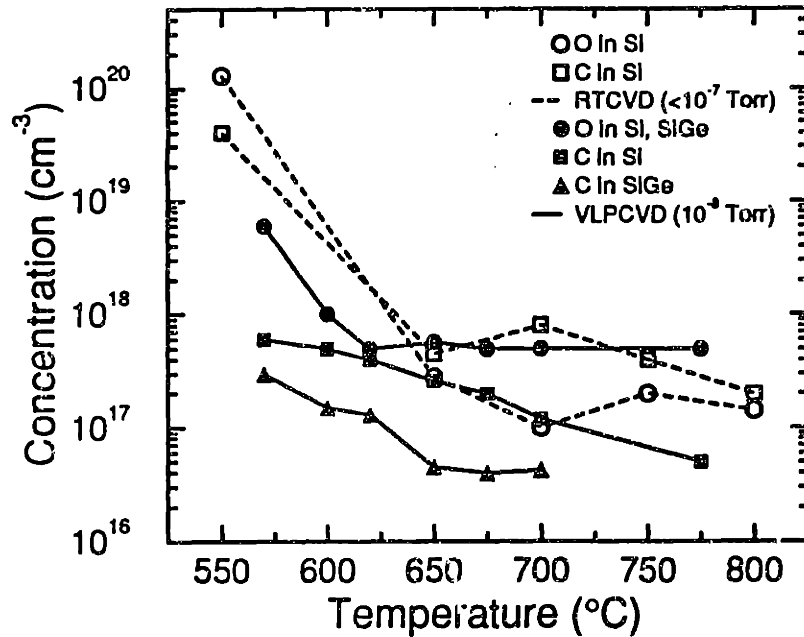

(b)

Figure 4.11: (a) SIMS data of oxygen and carbon recontamination at the interface of $Si_{1-x}Ge_x$ and Si buffer layer when system was cooled from 775°C, at which Si buffer layer was deposited, to the $Si_{1-x}Ge_x$ growth temperatures (570 – 700°C). Also exhibited is the system cooling times. (b) Oxygen and carbon concentrations in VLPCVD Si and $Si_{1-x}Ge_x$ films and in RTCVD Si films grown at 550 – 800°C. In both cases, SiH_4 and GeH_4 were used as source gases in H_2 carrier gas.

interface of $Si_{1-x}Ge_x$ and Si buffer layer, which resulted from the surface recontamination during chamber cooling. The surface recontamination was observed to depend on the duration of system cooling. It is clear that oxygen concentration at the $Si_{1-x}Ge_x$/Si interface remains relatively constant at temperatures above 620°C and is independent of the reactor cooling time with substrate sitting in an 80 sccm H_2 flow; however, carbon concentration was measured to increase gradually as temperature decreased. Figure 4.11 (b) exhibits the amounts of oxygen and carbon contaminants within Si and $Si_{1-x}Ge_x$ layers as a function of deposition temperature. The different behaviors of oxygen and carbon recontamination at surface are consistent with the tendency of their incorporation into growing Si and $Si_{1-x}Ge_x$ layer. From Fig. 4.11 (b), we see that deposition temperatures higher than 620°C did not affect the level of oxygen in $Si_{1-x}Ge_x$ and Si films, but a slow increase in the amount of carbon was evident as the growth temperature is lowered. Notice that carbon incorporation in $Si_{1-x}Ge_x$ remains the same at temperatures above 650°C. In addition, carbon contamination in $Si_{1-x}Ge_x$ is less pronounced than in Si but the reason is not clear yet.

Figure 4.11 (b) also compares bulk incorporation of carbon and oxygen in rapid thermal chemical vapor deposition (RTCVD) and VLPCVD films. Interesting to see that oxygen contamination is more severe in VLPCVD than in RTCVD, while the reverse is true for carbon. In both systems oxygen and carbon incorporation increase substantially when deposition takes place at temperatures below 620 – 650°C. This may provide an evidence of fundamental limit upon low-temperature deposition under background pressure of $\sim 10^{-7}$ Torr for non-loadlocked CVD systems. High level of oxygen ($\sim 2\times10^{20}$ cm^{-3}) was also observed in non-locked LRP at 625°C [46]. The measured oxygen concentration in RTCVD films grown at 650°C was found to be more than three orders of magnitude greater than for a film deposited at 900°C, and it has been determined that, under the limited base pressure of 10^{-7} – 10^{-8} Torr, the incorporated oxygen could be from the residual water

partial pressure in the chamber [35]. In VLPCVD, the possible oxygen sources include chamber out-gassing and residual water. On the other hand, carbon in the reactor is believed to be the out-diffusion of binder from silicon gaskets [91]. The gasket was utilized to seal the quartz reaction tube and stainless-steel endplates. When exposed to lamp radiation, the gaskets start to degrade and release carbon species.

Based on the results that oxygen recontamination becomes significant as temperatures was below 620°C, we conclude that under very low pressure conditions oxygen accumulation or oxide re-growth during growth interruption longer than 35 min will become a major concern for preparing a clean surface for low temperature epitaxial growth. The increase of surface oxygen and carbon content could be disastrous to strained-layer growth. A worse case resulted from 700°C clean is shown in Fig. 4.2 (c) in which misfit dislocations were observed by XTEM in a $Si/Si_{0.81}Ge_{0.19}/Si$ structures. The presence of misfit dislocations in the 510Å-thick $Si_{0.81}Ge_{0.19}$ was not expected, as in our another investigation, $Si_{0.80}Ge_{0.20}$ layer of 800Å grown at 620°C was confirmed to be fully strained by Raman spectrum and XTEM. The severe contamination problem was further confirmed by SEM, as indicated in Fig. 4.2, with the inclusions seen on the surface.

Though excess amount of oxygen was measured with $Si_{1-x}Ge_x$, it may not be the reason for the initial generation of misfit dislocation, because, according to a report on the effect of oxygen on the thermal stability of $Si_{1-x}Ge_x$ strained layer, oxygen was found to impede the kinetics of dislocation formation [92]. Therefore, it is possible that the appearance of misfit dislocation is formed by the extended defects, including threading dislocation, created by initial oxygen and carbon peaks, which is exacerbated by recontamination on the substrate surface during susceptor cooling. In a previous VLPCVD work on argon/hydrogen in situ surface cleaning low temperatures [93], it was claimed that interfacial oxygen and carbon levels of (9–100) $\times$ 10^{19} and (2–52) $\times$ 10^{18} together might lead to defected epitaxial

layer grown on the poor interface at 600°C, in spite of no surface damage incurred by argon/hydrogen plasma. Our present growth procedures (700°C surface clean followed by 570°C deposition) gave rise to even worse carbon contamination and high oxygen concentration; thus, the formation of growth defects leading to misfit dislocation is possible. To prevent such problem for low temperature deposition followed by surface cleaning at higher temperature, a buffer layer deposition prior to or during chamber cooling was found necessary in VLPCVD. Though systematic investigation was not performed, data in previous VLPCVD paper [93] suggests that such buffer layer is required for deposition at temperatures below 650°C.

4.4.2 $Si_{1-x}Ge_x$ Deposition on Patterned Wafers

In Fig. 4.7 (a) and 4.8 (a) we observe that the heteroepitaxial $Si_{1-x}Ge_x$ strained layers are selectively grown in the patterned oxide windows, while nucleation of polycrystalline $Si_{1-x}Ge_x$ is completely suppressed on the oxide. The selective deposition is usually performed using chlorinated silane as the silicon source, with the addition of hydrogen chloride or the reaction product of hydrogen chloride to suppress the nucleation of polycrystalline Si. The usage of SiH_4 make selective growth difficult because of no hydrogen chloride involved in the process. Thus, the growth time for selective Si epi-layer is limited to the incubation time of polycrystalline Si. In previous VLPCVD work, growth-sputter cycle, along with the use of H_2 to inhibit poly-Si nucleation, has been proposed to alleviate the problem and to achieve thick-layer epitaxial Si selective growth [94]. Selective heteroepitaxy of undoped $Si_{1-x}Ge_x$ in an UHVCVD reactor from SiH_4 and GeH_4/H_2 has been reported [95]. Shortly, selectively grown As-doped $Si_{1-x}Ge_x$ layer from $AsH_3/GeH_4/SiH_4/H_2$ has been presented for VLPCVD [89]. In a study using UHVCVD, it is found that selective growth is maintained during a short incubation time at 600°C and the incubation time is increased by introducing GeH_4/H_2. The observed increase in incubation times with GeH_4/H_2 flow could be due to GeH_4 retarding the formation

of stable nuclei by the evolution of GeO [96] or to hydrogen effects [97]. Direct comparison between VLPCVD and UHVCVD is difficult because the employed flow rates of source gases and H_2 carrier gas are different and cleaner environment in UHVCVD may also reduce the adsorption site density for Si deposition on oxide [98]. But we notice that, under optimized operation conditions, the maximum selective thicknesses of $Si_{1-x}Ge_x$ with x = 0.14 – 0.15 achieved in these two reactors are similar. The estimated maximum selective thickness is about 800Å for both techniques, in spite of the different growth rates.

Another interesting feature we have observed is the {311} facet near the $Si_{1-x}Ge_x$/oxide interface (675°C) which is consistent with the observations from previous VLPCVD Si epitaxial growth on patterned oxide substrates at 800°C [94]. The formation of facet also appears in the multilayer deposition at 625°C, as shown in Fig. 4.9. Since {311} is a slow-growth plane, $Si_{1-x}Ge_x$ layer near the sidewall becomes thinner. But this does not imply the thinner $Si_{1-x}Ge_x$ near the sidewall is more stable compared to the thicker $Si_{1-x}Ge_x$ grown far from the sidewall. Indeed, as demonstrated in Fig. 4.8, the defects associated with the interface of $Si_{1-x}Ge_x$/poly-$Si_{1-x}Ge_x$/oxide could be nucleation source of misfit dislocation. In a paper reported by Nishida et al. [99], who used Raman scattering spectroscopy with an Ar-ion laser to measure directly the strain in 1500Å-thick $Si_{0.80}Ge_{0.20}$ grown on a Si substrate with a 2 and 10 μm patterned oxide, it was clarified that the misfit strain was smaller near the boundary than in the center, meaning that the strain was released around boundary. When the opening was smaller than 2.5 × 2.5 μm, an almost dislocation-free area was obtained because the region near the boundary is strain-relaxed. The reduction of misfit strain around the sidewall eliminated the generation of dislocations. Nishida et al. also reported that the strain energy in the film grown on the 10 μm opening is greater than on 2 μm opening. Though it was not mentioned by Nishida et al. whether or not misfit dislocation formed in the larger opening (10 × 10 μm), it is believed from

our work that, if the epitaxial window is large and the strain energy is high in the film, the sidewall is a possible nucleation source for misfit dislocation. Note that the patterned oxide substrates used by Nishida et al. were prepared by wet etching, which gives the trench more similar to that prepared by plasma-etch. In the LOCOS substrates, the boundary of $Si_{1-x}Ge_x$ and polycrystal and oxide is greatly reduced. Consequently, the resulted $Si_{1-x}Ge_x$ films are expected to have higher strain energy and be more stable because the strain relaxation near the boundary is reduced and the chance of dislocation nucleation from the boundary is eliminated, as shown in Fig 4.7.

Finally, from the multilayer deposition on different oxide openings, Fig. 4.9 suggests that the $Si_{1-x}Ge_x$ and Si deposition rate are independent of the opening size. Since $Si_{1-x}Ge_x$ growth rate is a function of Ge, the identical $Si_{1-x}Ge_x$ thicknesses in both 5 × 5 mm and 10 ×10 μm windows imply that Ge incorporation might not depend on the window size either.

4.5 Conclusion

$Si_{1-x}Ge_x$/Si strained heterostructures have been grown on blanket substrates at 620°C and on patterned oxide substrates at 675°C and 625°C using a VLPCVD reactor. Oxygen and carbon contamination in both Si and $Si_{1-x}Ge_x$ films were examined and it was found that, similar to RTCVD operated under a base pressure of $< 10^{-7}$ Torr, both oxygen and carbon impurities increased rapidly as the deposition temperature is below 620°C, suggesting a limit on the purity of VLPCVD films. This fundamental limit can be further realized from the deposition of 500Å $Si_{0.80}Ge_{0.20}$ at 570°C where film contamination became sever and misfit dislocation formed. We also observed that, at 620°C, two-dimensional growth of $Si_{1-x}Ge_x$ layers is only likely at Ge compositions of < 25%. When Ge content exceeds 25%, islanding $Si_{1-x}Ge_x$ was seen. In addition, we have investigated the effects of iso-

lation techniques on the quality of $Si_{1-x}Ge_x$ layers. We found that $Si_{1-x}Ge_x$ layer grown on LOCOS patterned substrates appeared to be more stable because of the greatly reduced boundary of $Si_{1-x}Ge_x$, poly-$Si_{1-x}Ge_x$ and oxide. High-quality multilayer $Si_{1-x}Ge_x$/Si structures were also demonstrated, and the Si and $Si_{1-x}Ge_x$ thickness was found independent of window size.

Chapter 5

Growth Kinetics of $Si_{1-x}Ge_x$

5.1 Introduction

Over the past few years there has been significant interest in $Si_{1-x}Ge_x$ heteroepitaxial growth on silicon substrates because the $Si_{1-x}Ge_x/Si$ heterostructure allows bandgap engineering to be used in conjunction with silicon technologies. Deposition of $Si_{1-x}Ge_x$ on silicon carried out by chemical vapor deposition (i.e, atmospheric pressure chemical vapor deposition (APCVD) [32, 34, 37, 38]. limited reaction processing (LRP) or rapid thermal chemical vapor deposition (RTCVD) [26],[29], [31], [33], [35], [114], low pressure chemical vapor deposition (LPCVD) [87, 36], very low pressure chemical vapor deposition (VLPCVD) [100], and ultrahigh vacuum chemical vapor deposition (UHVCVD) [27, 30]), has been extensively studied in recent years, and kinetic data covering germanium incorporation and/or growth rate have been provided by several groups. However, different trends in deposition rate against germanium incorporation have been observed; for example, a monotonic increase in $Si_{1-x}Ge_x$ deposition rate with increasing germanium content was reported using APCVD and RTCVD with a mixture of dichlorosilane, germane, and hydrogen at 625 - 640°C [38, 29, 46]. Employing silane and germane as process gases in UHVCVD at 550°C and in VLPCVD at 570°C, similar growth trends were observed [27, 101]. But the deposition rate was

reported to decrease as germanium content increases in the epitaxial process using VLPCVD at 750 and 700°C and LPCVD at 750°C with silane-germane-(hydrogen) mixtures [36, 100, 101], At intermediate temperatures of 600 – 623°C, studies using UHVCVD, LPCVD, and VLPCVD show that a peak exists in $Si_{1-x}Ge_x$ growth rate versus germanium content [30, 36, 101]; the growth rate increases first and then falls off after reaching a maximum. This complex behavior has been attributed to a competition between an increasing desorption rate of surface hydrogen, which enhances the growth rate when germanium content is low, and decreasing sticking probabilities for the reactive hydrides, which degrades the growth rate when germanium content is high. [36]. An investigation of the activation energy in $Si_{1-x}Ge_x$ growth suggested that the observed growth rate peak in UHVCVD, VLPCVD, and LPCVD might arise from different rate-limiting steps operative at different germanium contents and deposition temperatures [101]. However, even with similar germanium contents and processing temperatures (610 – 640°C), RTCVD and APCVD exhibit a monotonic increase in growth rate as a function germanium or germane flow and no peak in growth rate. Some distinct features among LPCVD/VLPCVD/UHVCVD and APCVD/RTCVD include different source gases (i.e., silane-germane-(hydrogen) versus dichlorosilane-germane-hydrogen), and different deposition pressures (i.e., 1 – 100 mTorr versus 6 – 760 Torr); hence, comparisons among these CVD reactors appear difficult because the growth mechanisms may be reactor/process dependent.

By varying the gas flow rates at a constant pumping speed in VLPCVD, we have found that the position of the growth rate peak was affected by both hydrogen and deposition pressures [102]. More importantly, the range where the growth rate was enhanced by germanium incorporation was increased consistently by raising the gas flows or deposition pressure, and this helps to explain the effects of operating pressure on $Si_{1-x}Ge_x$ growth. A more recent study of $Si_{1-x}Ge_x$ deposition rate using three different silicon reaction gases, dichlorosilane, silane, and

disilane, in the same reactor (APCVD) showed similar trends for all gases, with the deposition rate enhanced by the addition of germanium, and the differences in the reported growth rate behaviors using a variety of reactors were suggested to be a result of the different operating-pressure regimes, rather than the different source gases [103].

Although possible reasons, including promoted hydrogen desorption at low germanium contents and decreased sticking probabilities at high germanium contents due to germanium addition, as well as the effects of deposition pressures on the growth rate peak, have been proposed to account for the growth phenomena, there is still a lack of understanding of mechanistic details. In this chapter, we examine the $Si_{1-x}Ge_x$ heteroepitaxial growth kinetics under very low pressure chemical vapor deposition (VLPCVD) conditions at temperatures of 570 – 700°C.

5.2 Experiments

The VLPCVD reactor employed here has been described elsewhere [78], and deposition of high-quality $Si_{1-x}Ge_x$/Si epitaxial multilayer structures have been demonstrated [89]. In this work, $Si_{1-x}Ge_x$/Si multilayer structures were deposited for the characterization of germanium incorporation and layer growth rate.

The procedure for substrate preparation was as follows. Prior to loading, the Si substrate was *ex situ* cleaned by 25:1 HF dip, DI water rinse, spin dry, and 5 min ultraviolet ozone exposure, which reduced carbon contamination and gaved a protective 12 Å oxide for the 1.5 hour bakeout at 775°C or 700°C in 6 mTorr argon flow. When the chamber reached ~1-2×10^{-7} Torr, the ozone-created protective oxide was removed by a 2.5 watts argon plasma at ~4 mTorr with the susceptor biased to −100 V_{dc} for 15 min at 775°C. Following the argon sputter cleaning, a ~1400 Å silicon epitaxial layer was grown using silane/hydrogen (3/7 mTorr) for 5 min, followed by a temperature ramp allowing the susceptor to cool from 775°C

to lower temperatures for $Si_{1-x}Ge_x$ deposition.

The multilayer deposition procedure in this study is described elsewhere [101, 102]. In each run, six discrete $Si_{1-x}Ge_x$ layers were grown with various germane/silane ratios: 1.25%, 2.50%, 3.75%, 4.25%, 5.00%, and 5.75%, increasing from the substrate surface. Individual $Si_{1-x}Ge_x$ layers were separated by a silicon spacer layer to facilitate material characterization. The source gases used were 40 sccm silane with various germane flow in an 80 sccm hydrogen flow. The selected deposition temperatures of 700, 675, 650, 620, 600, and 570°C were kept constant in each multilayer deposition. Deposition times for silicon and $Si_{1-x}Ge_x$ growth were 5 min. Growth pressures were 16 – 18 mTorr.

To examine the impact of source gase and hydrogen flows on $Si_{1-x}Ge_x$ growth, multilayer experiments were carried out at 620°C. These structures consist of six $Si_{1-x}Ge_x$ layers spaced by silicon layers with germane/silane ratios increasing from 1.25% to 5.75% with or without hydrogen carrier gas. The effects of deposition pressure were investigated by varying both silane and germane flow rates, while keeping the same germane/silane ratios, from run to run. By keeping the pumping speed of the turbo pump essentially constant ($510\ell/s$), the deposition pressure increased linearly with the total gas flow rate, which is mainly determined by the flow rate of silane. The silane flow rates employed here were 20, 40, 60, and 80 sccm with different germane flow rates at the same germane/silane ratios of 1.25%, 2.50%, 3.75%, 4.25%, 5.00%, and 5.75% in all runs. To eliminate the influence of hydrogen, no hydrogen carrier gas was used and the deposition pressures corresponding to 20 – 80 sccm SiH_4 + (0 – 4.6) sccm GeH_4 range over 3 to 10 mTorr. The investigation of the effect of hydrogen flow on $Si_{1-x}Ge_x$ growth was carried out using only one silane flow rate (40 sccm) with the same germane/silane ratios mentioned above. The employed hydrogen flows are 0, 50, 80, and 120 sccm giving rise to a pressure range of 6 – 36 mTorr during epitaxial growth.

Secondary ion mass spectrometry (SIMS) and Rutherford backscattering

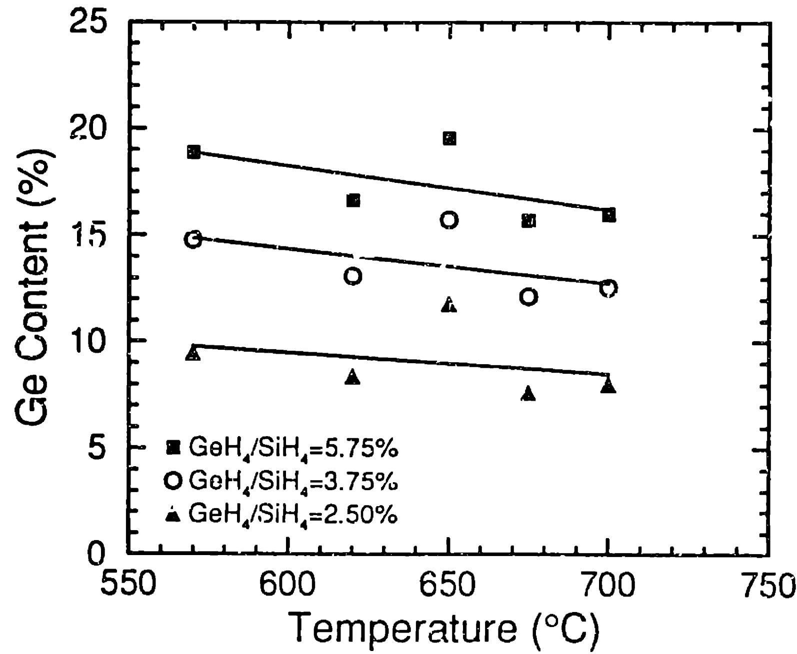

Figure 5.1: Germanium composition in $Si_{1-x}Ge_x$ as a function of deposition temperature; silane flow = 40 sccm and hydrogen flow = 80 sccm.

spectrometry (RBS) were performed to measure germanium composition and layer thickness. Our previous multilayer research confirmed that thicknesses measured by these techniques are in excellent agreement with those obtained from cross-sectional transmission electron microscopy (XTEM). Multilayer thicknesses measured by XTEM and confirmed by SIMS led to errors of less than 25Å for silicon and $Si_{1-x}Ge_x$ layers of 400 – 800Å thick [89]. Furthermore, several single-layer $Si_{1-x}Ge_x$ depositions revealed no inconsistence with multilayer data.

5.3 Results

5.3.1 Germanium Incorporation

Figure 5.1 shows germanium content as a function of temperature for layers deposited over the temperature range 570 – 700°C for various GeH_4/SiH_4 flow ratios. Germanium incorporation increases slightly with a reduction in deposition temper-

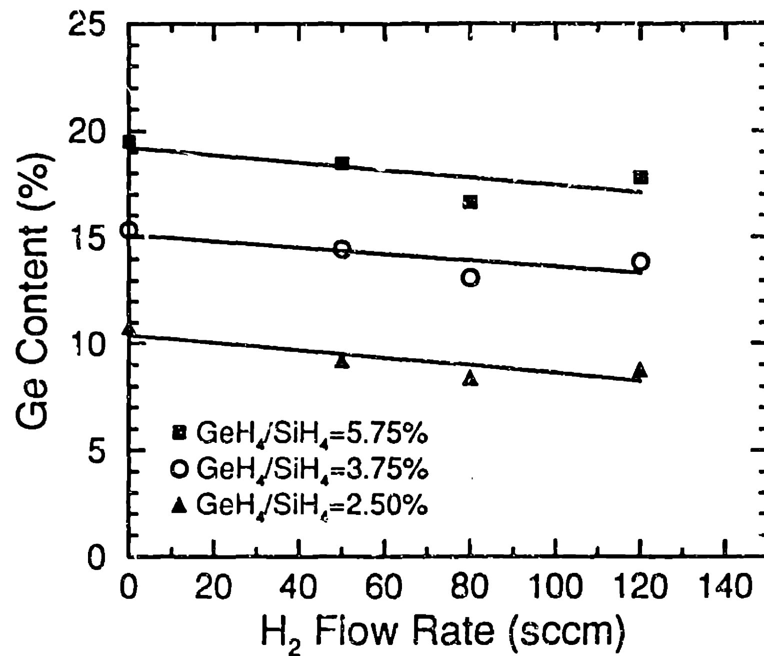

Figure 5.2: Atomic germanium fraction as a function of hydrogen flow rate at 620°C; silane flow = 40 sccm.

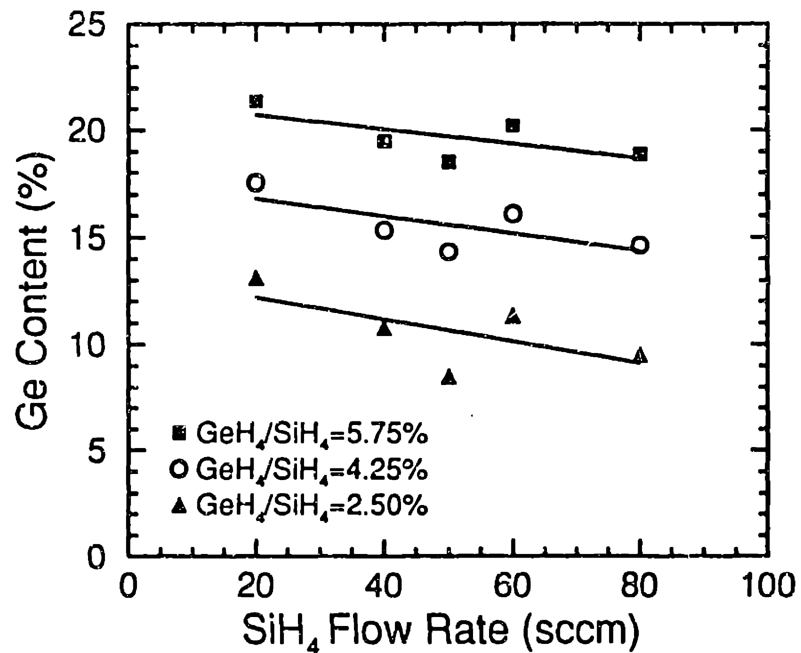

Figure 5.3: Atomic germanium fraction as a function of silane flow rate at 620°C; no hydrogen flow.

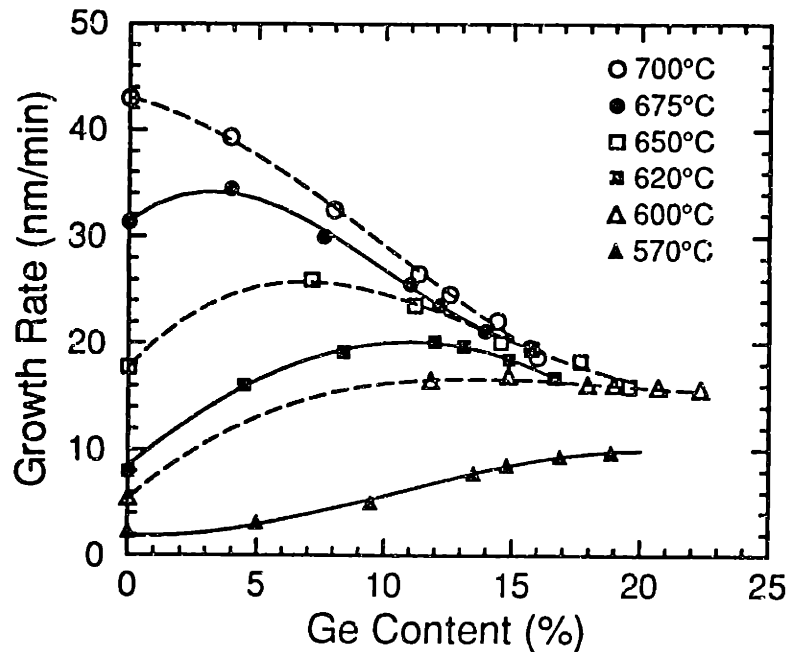

Figure 5.4: Growth rate of $Si_{1-x}Ge_x$ measured at different germanium content; silane flow = 40 sccm, hydrogen flow = 80 sccm

ature.

Since the chamber pressure increased linearly with the gas flow rate, for convenience, we use the gas flow rate to represent the the pressure. The effects of hydrogen and silane flow rates on the amount of germanium incorporated into $Si_{1-x}Ge_x$ are illustrated respectively in Fig. 5.2 and Fig. 5.3. In both cases, for a given GeH_4/SiH_4 ratio a increase in hydrogen or deposition pressure was observed to reduce germanium incorporation.

5.3.2 $Si_{1-x}Ge_x$ Growth Rate

The measured germanium dependency of $Si_{1-x}Ge_x$ growth rates at temperatures of 570 - 700°C are shown in Fig. 5.5. Data measured from $Si_{1-x}Ge_x$ layers have germanium compositions in the range 0 - 0.23. It can be observed that the trends of $Si_{1-x}Ge_x$ deposition rate versus germanium incorporation strongly depend on

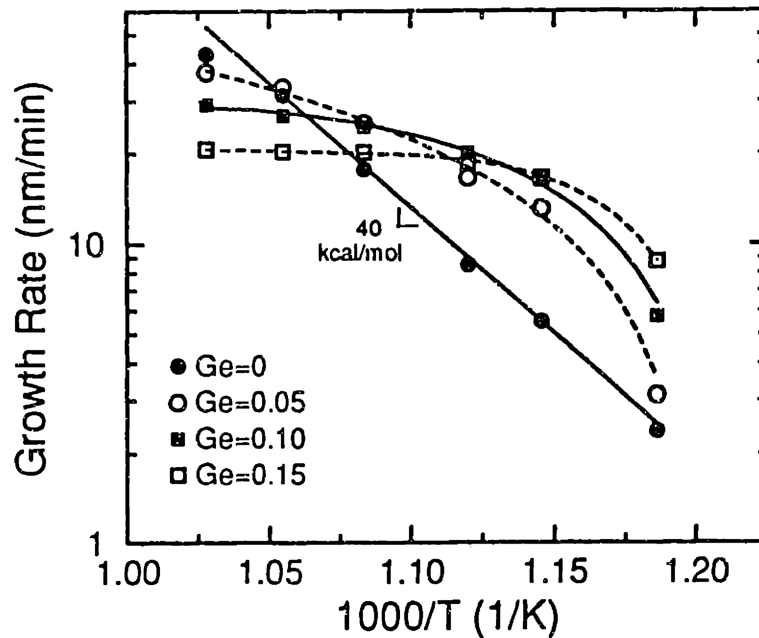

Figure 5.5: Arrhenius plots for the growth rate of $Si_{1-x}Ge_x$ shown in Fig. x in the temperature range of 570 – 700°C.

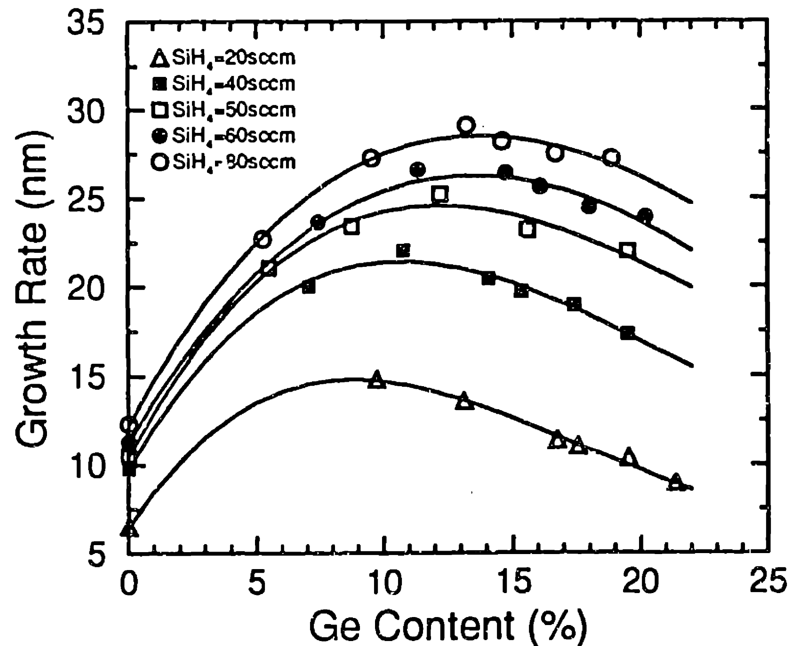

Figure 5.6: Measured $Si_{1-x}Ge_x$ growth rate expressed as a function of germanium incorporation. Layers were grown at 620°C at different deposition pressures with silane flow rate = 20, 40, 50, 60, and 80 sccm; no hydrogen flow.

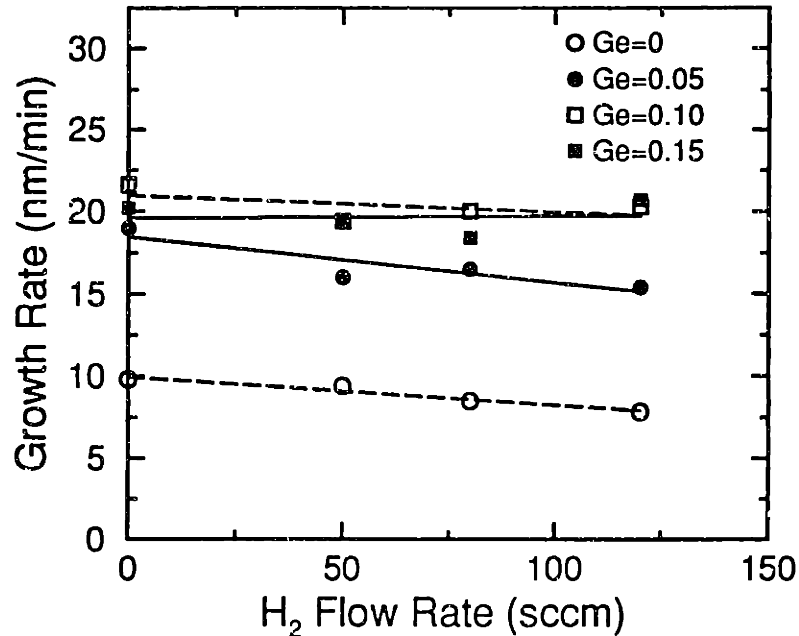

Figure 5.7: $Si_{1-x}Ge_x$ growth rate versus hydrogen flow rate at 620°C. silane flow rate was kept at 40 sccm. The germanium content that gives maximum growth rate for varied hydrogen flow is also indicated.

temperature. At 700°C, the growth rate decreases monotonically with increasing germanium, which is consistent with our previous $Si_{1-x}Ge_x$ depositions at 750°C using the same reactor [100]; on the other hand, the growth rate was found to be enhanced at 570°C with germanium up to 19%. At intermediate temperatures between 570 and 700°C, $Si_{1-x}Ge_x$ deposition rate increases first, followed by a decrease after reaching a peak. The position of the growth peak is a function of temperature. As temperature is lowered, the peak occurs at higher germanium content.

The measured growth rate as a function of deposition temperature shown in Fig. 5.4 can be better understood from the Arrhenius plot (Fig. 5.4. Growth rate data for a fixed germanium content extracted from curves that best fit the experimental results in Fig. 5.4 are plotted in Fig. Fig. 5.5. Epitaxial growth of silicon has an apparent activation energy of 40 kcal/mol that agrees with previous

VLPCVD work [104]. The presence of germanium during epitaxy was found to modify the activation process. With the increase of germanium, the activation energy was no longer constant at 570 – 700°C. The value of activation energy was significantly reduced at temperatures close to 700°C. On the other hand, an activation energy of near 40 kcal/mol was observed at lower temperatures and a broad transition was observed. This suggests the rate-limiting step in silicon deposition is not necessarily the same as that in $Si_{1-x}Ge_x$ deposition, and the range over which different mechanisms dominate is both germanium and temperature dependent. At higher temperatures and germanium contents, the rate-limiting step has a lower activation energy; whereas, at somewhat lower temperatures and germanium contents the growth rate is determined by a slowest step with higher activation energy.

The influence of silane flow rate on the epitaxial deposition rate of $Si_{1-x}Ge_x$ expressed as a function of germanium content is exhibited in Fig. 5.6. Because the flow rate of silane is much higher than that of germane, the growth pressure can be looked as linear function of silane flow rate. It is seen that the peak position moved to higher germanium composition as the SiH_4 flow rate increases. In other word, the germanium range over which $Si_{1-x}Ge_x$ deposition rate was enhanced was extended.

Figure 5.7 presents epitaxial growth rate as a function of hydrogen flow rate at four germanium compositions. The reduction of about 10% in silicon epitaxial growth rate by introducing 80 sccm hydrogen quantitatively agrees with previous VLPCVD data at 800°C [105]. Therefore, we consider the slightly reduced growth rate as a result of hydrogen addition rather than measurement error. In addition, the use of hydrogen was found to cause slight or no variations in $Si_{1-x}Ge_x$ growth rate. A consistent decrease in low-germanium film was measured; while hydrogen seems to have no effect on films with more incorporated germanium.

5.4 Discussion

5.4.1 Kinetic Model

In this section, we attempt to develop a steady-state kinetic model based on surface-controlled reactions to account for the VLPCVD growth of $Si_{1-x}Ge_x$ epitaxial layers using silane and germane as source gases at low temperatures.

The decomposition mechanisms of silane on (100) silicon surface have recently been investigated by Gate *et al.* [106] using static secondary ion mass spectrometry (SSIMS). The net reaction

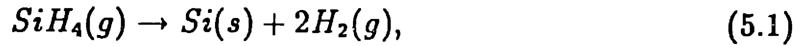

$$SiH_4(g) \rightarrow Si(s) + 2H_2(g), \tag{5.1}$$

which is commonly used in CVD to describe the growth silicon films by pyrolysis of silane was observed to occur via a series of reaction steps, which generate su face species SiH_3, SiH_2, SiH, and H, as follows:

$$SiH_{4(g)} + 2_ \stackrel{k_{1,Si}}{\rightarrow} \underline{Si}H_3 + \underline{H} \tag{5.2}$$

$$\underline{Si}H_3 + _ \stackrel{k_{3,Si}}{\rightarrow} \underline{H} + \underline{Si}H_2 \tag{5.3}$$

$$2\underline{Si}H_2 \stackrel{k_{4,Si}}{\rightarrow} H_2(g) + 2\underline{Si}H \tag{5.4}$$

$$2\underline{Si}H \stackrel{k_{5,Si}}{\rightarrow} H_2(g) + 2\underline{Si} \tag{5.5}$$

$$2\underline{H} \stackrel{k_{6,H}}{\rightarrow} H_2(g) + 2_ \tag{5.6}$$

$$\underline{Si} \stackrel{k_{7,Si}}{\rightarrow} Si + _ \tag{5.7}$$

where the symbol $_$ denotes a surface vacant site. $k_{1,Si}$ is the condensation coefficient, and k_i (i= 3 – 7) are rate constants for reactions (5.2 – 5.7). In step (5.2), two adjacent dangling bonds are required on the silicon surface for dissociative adsorption of SiH_4. To write the rate equations, it is important to know the order of decomposition steps of SiH_x in silane case with x = 1, 2, 3, and it should be

noted that both first- and second-order models can be postulated and the order of reaction may depend on surface coverage of the decomposition species, on the fraction of vacant sites, and other factors [106]. Thus, the order of reaction may differ under different growth conditions because of coverage dependent kinetics. Following published literatures, in this study decomposition kinetics for SiH_3 in reaction (5.3) is first order in SiH_3 and first order in available site [106]. Isothermal studies revealed second-order hydrogen desorption kinetics from both the monohydride and dihydride surface species [107]. The second-order reaction resulted from recombination and desorption of adatoms. However, a new mechanism for the thermal desorption of molecular hydrogen from SiH on (100) silicon has been identified, and the observed unusual first-order desorption kinetics are due to the irreversible excitation of a hydrogen adatom into a delocalized, two-dimensional band state on the surface [108]. The desorption reaction occurs between this excited hydrogen adatom and a second, localized hydrogen adatom. The discrepancy of reaction order for monohydride decomposition may be explained by the different range of fractional surface coverage. In the case of coverage greater than 0.2, first and second-order cannot be distinguished [108]. Here we use a second-order model for SiH decomposition because excess hydrogen flow was frequently flowed during deposition and higher surface coverage is likely in most cases.

In VLPCVD it is reasoned that the silane residence time of 0.1 sec is so short that no homogeneous silane gas-phase dissociation occurs and the only adsorbing species is silane [106]. Assume that germane reacts with the silicon (100) surface via the similar decomposition steps. In addition, we consider an activated complex $(MH_3\text{-}H)^*$, where M represent silicon or germanium, generated by the collision of silane and germane with the surface,

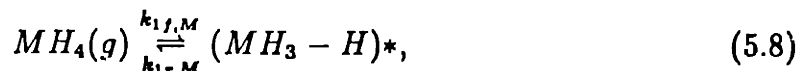

$$MH_4(g) \underset{k_{1r,M}}{\overset{k_{1f,M}}{\rightleftharpoons}} (MH_3 - H)*, \tag{5.8}$$

followed by the decomposition

$$(MH_3 - H)* \overset{k_{2,M}}{\rightarrow} \underline{M}H_3 + \underline{H}. \tag{5.9}$$

Since molecular hydrogen is in excess in gas mixture, we do not rule out the possible reverse reaction of hydrogen desorption, and reaction (5.10) becomes

$$2\underline{H} \underset{k_{6r,H}}{\overset{k_{6f,H}}{\rightleftharpoons}} H_2(g) + 2_ \tag{5.10}$$

For each species the rate of change of the surface coverage (θ) can be expressed as the following rate equations

$$\frac{d\theta_{M*}}{dt} = k_{1f,M}P_{MH_4}\theta^2 N_s^2 - k_{1r,M}\theta_{M*}^2 N_s^2 - k_{2,M}\theta_{M*}^2 N_s^2, \tag{5.11}$$

$$\frac{d\theta_{MH_3}}{dt} = k_{2,M}\theta_{M*}^2 N_s^2 - k_{3,M}\theta_{MH_3}\theta N_s^2, \tag{5.12}$$

$$\frac{d\theta_{MH_2}}{dt} = k_{3f,M}\theta_{MH_3}\theta N_s^2 - k_{4,M}\theta_{MH_2}^2 N_s^2, \tag{5.13}$$

$$\frac{d\theta_{MH}}{dt} = k_{4,M}\theta_{MH_2}^2 N_s^2 - k_{5,M}\theta_{MH}^2 N_s^2, \tag{5.14}$$

$$\frac{d\theta_H}{dt} = k_{2,M}\theta_{M*}^2 N_s^2 + k_{3,M}\theta_{MH_3}\theta N_s^2 - k_{6f,H}\theta_H^2 N_s^2 + k_{6r,H}P_{H_2}\theta^2 N_s^2, \tag{5.15}$$

and

$$\frac{d\theta_M}{dt} = k_{5,M}\theta_{MH}^2 N_s^2 - k_{7,M}\theta_M N_s, \tag{5.16}$$

where N_s is the density of surface sites, P_{MH_4} and P_{H_2} are partial pressures of silane or germane and hydrogen. θ_{M*}, θ_{MH_3}, θ_{MH_2}, θ_{MH}, θ_M, and θ_H denote the surface coverage fractions of MH_3* and $H*$, MH_3, MH_2, MH, M, and H, respectively. The surface vacant sites are represented by θ, and, for the conservation of surface sites,

$$\theta + \theta_H + f_{Si} + f_{Ge} = 1, \tag{5.17}$$

where f_{Si} and f_{Ge} denote the total surface coverage of silicon- and germanium-associated species. Applying the steady-state approximation for all species

$$\frac{d\theta}{dt} = \frac{d\theta_{M*}}{dt} = \frac{d\theta_{MH_3}}{dt} = \frac{d\theta_{MH_2}}{dt} = \frac{d\theta_{MH}}{dt} = \frac{d\theta_H}{dt} = \frac{d\theta_M}{dt} = 0, \tag{5.18}$$

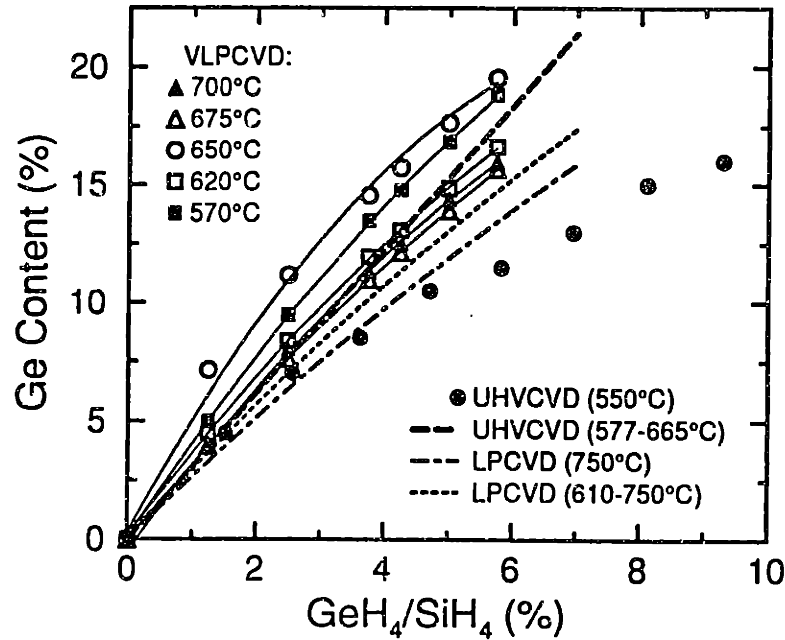

Figure 5.8: Comparisons of germanium incorporation versus germane fraction for different reactors.

and utilizing equation (5.17), the fractional coverage of each surface species can be solved.

Once θ is known, the growth rate of $Si_{1-x}Ge_x$, R(x), can be obtained by [109]

$$R = R_{Si}(x)+R_{Ge}(x) = \frac{k_{1f,Si}k_{2,Si}}{k_{1r,Si}+k_{2,Si}}\theta^2 N_s^2 P_{SiH_4} + \frac{k_{1f,Ge}k_{2,Ge}}{k_{1r,Ge}+k_{2,Ge}}\theta^2 N_s^2 P_{GeH_4}, \quad (5.19)$$

where $R_{Si}(x)$ and $R_{Ge}(x)$ are silicon and germanium component of deposition rate, and germanium composition

$$x = \frac{R_{Ge}}{R_{Si}+R_{Ge}}. \quad (5.20)$$

5.4.2 Germanium Incorporation

In our previous work, a simple relation between germanium fraction and processing gases has been obtained for $x \leq 0.20$ [101]

$$\frac{x}{1-x} = \frac{k_{1f,Ge}k_{2,Ge}(k_{1r,Si} + k_{2,Si})}{k_{1f,Si}k_{2,Si}(k_{1r,Ge} + k_{2,Ge})} \frac{P_{GeH_4}}{P_{SiH_4}} \sim m \frac{P_{GeH_4}}{P_{SiH_4}}, \tag{5.21}$$

where P_{SiH_4} and P_{GeH_4} are partial pressures of silane and germane, respectively, and m is between 3.24 - 4.29 at temperatures 570 - 700°C for VLPCVD. Similar expressions have been used for LPCVD previously and the constant m is $\sim$ 2.7 (deposition pressure $\sim$ 10 mTorr) at 750°C [87] and $\sim$ 3 (deposition pressure $\sim$ 100 mTorr) at 610 - 750°C [36]. Using UHVCVD, the germanium content is approximately given by x=0.306($flow_{GeH_4}/flow_{SiH_4}$) [30]. Fig. 5.8 summarizes germanium incorporation versus germane fraction for different reactors employing silane-germane-(hydrogen) mixtures, and it is evident that well defined relations exist in all cases.

It is not clear at this point how deposition pressure and hydrogen influence germanium incorporation. A speculation is that as germanium may act as desorption center for surface species, which will be discussed in the next section, the germanium adatoms are thought to be usually surrounded by adsorbed species, thus the probability of germanium being incorporated into the growing layer is determined by how long . Raising hydrogen and deposition pressure results in higher coverage of surface and may hinder the incorporation of adsorbed germanium atoms. Since the overall variations in Fig. 5.2 and Fig. 5.3 are not significant, for a given germane/silane ratio we will not take into account the possible change of m or $k_{i,M}$ in equation (5.21) led by the increase of hydrogen or total deposition pressure at 620°C, and the reaction parameters in equation (5.21) are considered as functions of germanium only in later discussions.

5.4.3 $Si_{1-x}Ge_x$ Growth Rate

Hydrogen Desorption

In the study of kinetics of surface reactions in very low pressure chemical vapor deposition of silicon from silane, it was proposed that, in the low temperature limit silane adsorption is slowest but is not a simple rate determining step. The silane adsorption is controlled by the rate of hydrogen desorption from two surface SiH species, producing dangling bonds. However, in the cases that hydrogen was used as carried gas, as exhibited in Fig. 5.4, we consider equation (5.10) as the dominant source of surface coverage. For simplicity, we assume $\theta(x) \sim 1 - \theta_H(x)$, and equation (5.17) reduces to

$$\theta(x) = \frac{1}{1 + \frac{1}{k_{6f,H}^{1/2}}[(k_{2,Si}K_{1,Si}^2 + k_{3,Si}K_{2,Si}^2)P_{SiH_4} + (k_{2,Ge}K_{1,Ge}^2 + k_{3,Ge}K_{2,Ge}^2)P_{GeH_4} + k_{6r}P_{H_2}]^{1/2}}, \tag{5.22}$$

where
$$K_{1,M} = [\frac{k_{1f,M}}{(k_{1r,M}+k_{2,M})N_s^2}]^{1/2},$$

and
$$K_{2,M} = [\frac{k_{1f,M}k_{2,M}}{k_{3,M}(k_{1r,M}+k_{2,M})N_s^2}]^{1/2},$$

If surface hydrogen is manily from the adsorption of hydrogen molecular, equation (5.22) reduces to

$$\theta(x) = \frac{1}{1 + \frac{k_{6r,H}}{k_{6f,H}}P_{H_2}} \tag{5.23}$$

The value of $k_{6r,H}$ can be estimated by comparing the observed ratios of silicon epitaxial growth rate at different temperatures. It was found that $k_{6r,H}(700°C)/k_{6r,H}(570°C)$ = 1.3 in VLPCVD and thus $k_{8r,H}$ can be looked as constant at 570 – 700°C. $k_{6f,H}$ is an important parameter controlling hydrogen desorption.

It has been proposed that germanium could act as a desorption center for mobile hydrogen adatoms on the silicon surface, accelerating heterogeneous silane pyrolysis by the enhanced availability of open sites [27]. The supposition was

supported by a study of the desorption of deuterium from clean and germanium-covered surface, in which the presence of germanium on silicon surface dramatically lowers the deuterium (or hydrogen) desorption temperature [110]. The lowering of the deuterium desorption energies caused by surface germanium helps to account for the acceleration in growth rate observed in $Si_{1-x}Ge_x$ chemical vapor deposition. Following Garone *et al.* [29], we modify $k_{6f,H}$ due to germanium-enhanced hydrogen desorption as

$$k_{6f,H} = \nu[xe^{-E_{dG}/kT} + (1-x)e^{-E_{dS}/kT}], \tag{5.24}$$

where ν is the frequency factor, 8×10^{11} s^{-1}, and E_{dS} and E_{dG} are activation energy of hydrogen desorption from silicon and germanium, respectively. When temperature or germanium is low so that $k_{6r,H}P_{H_2}/k_{6f,H} \gg 1$, $\theta = \sqrt{k_{6f,H}/k_{6r,H}P_{H_2}}$ and equation (5.19) reduces to

$$R = R_{Si}(x)+R_{Ge}(x) = \frac{\nu[xe^{-E_{dG}/kT} + (1-x)e^{-E_{dS}/kT}]}{k_{6r,H}P_{H_2}}\left(\frac{k_{1f,Si}k_{2,Si}}{k_{1r,Si}+k_{2,Si}}P_{SiH_4}+\frac{k_{1f,Ge}k_{2,Ge}}{k_{1r,Ge}+k_{2,Ge}}P_{GeH_4}\right). \tag{5.25}$$

When temperature or germanium is high such that $k_{6r,H}P_{H_2}/k_{6f,H} \ll 1$, $\theta \sim 1$ and equation (5.19) yields

$$R = R_{Si}(x) + R_{Ge}(x) = \frac{k_{1f,Si}k_{2,Si}}{k_{1r,Si}+k_{2,Si}}P_{SiH_4} + \frac{k_{1f,Ge}k_{2,Ge}}{k_{1r,Ge}+k_{2,Ge}}P_{GeH_4}, \tag{5.26}$$

and the temperature and germanium dependencies of $Si_{1-x}Ge_x$ growth rate are from the condensation coefficients and rate constants of silicon and germanium.

The combination of equations (5.25) and (5.26) explains the behaviors of Arrhenius plots demonstrated in Fig. 5.5. For a fixed germanium fraction, the deposition rate has higher activation energy or is more temperature dependent as the deposition temperature is lowered. While at a given growth temperature, the activation energy decreases with increasing germanium concentration. This is supported by the observation that the deuterium desorption energy is lowered as

compared to the silicon (100) surface when germanium is present [110]. Thus, in the temperature regime of 570 – 700°C, unlike pure silicon epitaxial growth which shows a constant activation energy, $Si_{1-x}Ge_x$ heteroepitaxy on silicon exhibits an lower activation energy which is functions of both temperature and germanium content. The observed nonlinear Arrhenius temperature dependencies in $Si_{1-x}Ge_x$ growth implies that the rate-limiting step was altered by germanium. The modified $k_{6f,H}$, ν[xexp(-E_{dG}/kT) + (1-x)exp(-E_{dS}/kT)], owing to germanium incorporation plays an important role in the growth process limited by hydrogen desorption.

Though the equations derived above are based on the assumption that the equilibrium between surface hydrogen species and molecular hydrogen is reached. When excess amount of hydrogen is not employed, desorption of hydrogen from SiH and GeH species may become rate-determining step. May it be the case, $\theta = 1 - \theta_{SiH} - \theta_{GeH}$ and equation (5.5) strongly depends on $k_{5,Si}$ and $k_{5,Ge}$, that control the rate of SiH and GeH dissociation, and

$$\theta = \frac{1}{1 + K_{3,Si}P_{SiH_4}^{1/2} + K_{3,Ge}P_{GeH_4}^{1/2}}, \tag{5.27}$$

where $$K_{3,M} = [\frac{k_{2,M}k_{1f,M}}{k_{5,M}(k_{1r,M}+k_{2,M})N_s^2}]^{1/2}.$$

Considering the possible reaction $\underline{Si}H + \underline{Ge}H \rightarrow H_2(g) + \underline{Si} + \underline{Ge}$, we can modify $k_{5,M}$ in the way similar to equation (5.24). Hence, the qualitative analysis of $Si_{1-x}Ge_x$ growth rate as functions of θ_H and θ_{SiH} are similar.

Equations (5.25) and (5.26) also suggest that for a given temperature the growth rate of $Si_{1-x}Ge_x$ epitaxial layer with lower germanium fraction decreases as hydrogen flow is increased, which can be supported by Fig. 5.7. The increase of germanium eliminates the degradation of deposition rate caused by hydrogen addition. Besides, using the identity of (5.21), equations (5.25) and (5.26) imply that, as the temperature is kept constant the growth rate R(x) increases with germanium composition following ν[xexp(-E_{dG}/kT) + (1-x)exp(-E_{dS}/kT)]/(1-x) at lower

germanium contents and following 1/(1-x) at higher germanium contents. However, at 620°C, $Si_{1-x}Ge_x$ deposition rate first increases, as expected, but followed by a drop as germanium composition continues to increase, leaving a peak at intermediate germanium composition, as shown in Fig. 5.4. The increase in growth rate with the addition of germanium can be explained by the accelerated hydrogen desorption due to the reduced desorption energy, which gives more available sites for dissociative adsorption of silane and germane and thus enhance the overall deposition rate. However, this argument only holds under the conditions when surface hydrogen serves to block the surface, i.e. at lower germanium content or reduced deposition temperature, and conflicts the observed degradation in growth rate when germanium composition or deposition temperature is high. Recalling that the incorporation of germanium contributed to lowering the activation energy in $Si_{1-x}Ge_x$ growth rate (Fig. 5.5), it is appropriate to consider that the decreasing growth rate is subject to a rate-limiting step rather than hydrogen desorption. If hydrogen desorption is promoted by germanium and no longer controls the growth rate, other mechanisms may become dominant and lead to different germanium dependency of growth rate. In the following section, we will examine the possible reasons for the drop of $Si_{1-x}Ge_x$ growth rate owing to more incorporated germanium.

Sticking Probabilities of Silane and Germane

The diminished $Si_{1-x}Ge_x$ growth rate has been first discussed by Robbins *et al.* and was attributed to a decreasing sticking probabilities for the reactive hydrides as germanium composition increases [36]. A simple trial scaling relationship has been used to fit the experimental data. In previous study by VLPCVD, it was demonstrated that $k_{1f,M}$, $k_{1r,M}$, and $k_{2,M}$ are affected by germanium, which in turn change the deposition-pressure dependency of growth rate. If deposition pressure

plays an important in $Si_{1-x}Ge_x$ growth kinetics, the disprepancies in the reported deposition rates might be related to different deposition pressures [102]. The coefficients $k_{1r,M}$ and $k_{2,M}$ could be referred to as the sticking probabilities of silicon and germanium hydrides as mentioned by Robbins *et al.*. Recently, using dichlorosilane, silane, and disilane, along with germane, $Si_{1-x}Ge_x$ growth rate was measured to increase monotonically with increasing germanium content in the layer for all three silicon source gases, in contrast to the behavior seen in systems operating at substantially lower total deposition pressure, suggesting that the differences in previously reported behavior are dominated by the different operating-pressure regimes, rather than different silicon sources [103].

The effects of silane and germane flow rates on $Si_{1-x}Ge_x$ growth rate in VLPCVD is shown in Fig. 5.6. The extent of growth rate enhancement due to increasing silane and germane partial pressures depends on germanium content and increase greatly as x increases. Thus, the observed peak in growth rate moves to higher germanium value as the deposition pressure is raised. This means the reaction parameters involved in the growth process are germanium dependent and the degradation of growth rate at higher x can be somehow circumvented by providing more gas flows. To evaluate the possible alteration of reaction-rate parameters by germanium, we now restrict our attention to the growth behavior in the higher-germanium regime. We assume that the growth rate falloff occurs when hydrogen desorption is not dominant, and the growth kinetics is associated with a new rate-limiting step. Ruling out the coverage of surface hydrogen, we only consider the fractional coverage of adsorbed intermediate silane and germanium species, and under steady-state conditions

$$\theta \sim 1 - \theta_{Si*} - \theta_{Ge*} = \frac{1}{1 + K_{1,Si} P_{SiH_4}^{1/2} + K_{1,Ge} P_{GeH_4}^{1/2}}, \qquad (5.28)$$

and the density of available sites is determined by silane and germane flow rates. Using the identity of (5.21), equation (5.19) becomes

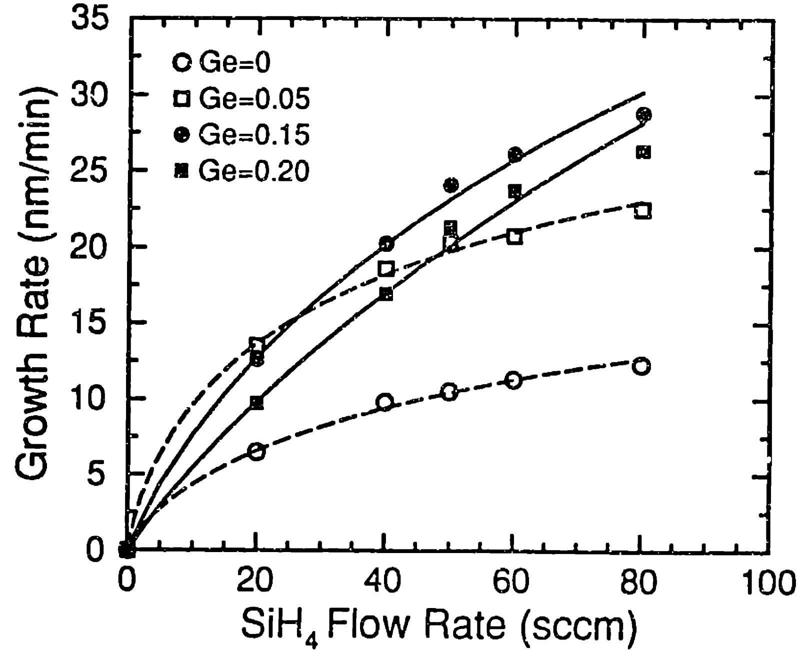

Figure 5.9: $Si_{1-x}Ge_x$ growth rate expressed as a function of silane flow rate. Growth rates for $x = 0$ and 0.05 were fit using equations (19) and (23), and equation (29) was used for $x = 0.15$ and 0.20.

$$R(x) = \frac{k_{2,Si}K_{1,Si}^2 P_{SiH_4}}{(1-x)\{1 + K_{1,Si}P_{SiH_4}^{1/2}[1 + (\frac{xk_{2,Si}}{(1-x)k_{2,Ge}})^{1/2}]\}^2} \tag{5.29}$$

Figure 5.9 shows the growth rate as a function of silane flow rate. Equation (5.29) was employed to fit the $Si_{1-x}Ge_x$ growth rates with $x = 0.15$ and 0.20 as shown in Fig. 5.9. Good agreement between equation (5.29) and experimental data was obtained. The influences of germanium on the rate constants of silicon is demonstrated in Fig. 5.10 and it is evident that $k_{2,Si}k_{1f,Si}/(k_{1r,Si} + k_{2,Si})$ decreases as germanium increases, suggesting that these parameters depend on germanium in some way reducing the entire growth rate. The measured decrease in $k_{2,Si}k_{1f,Si}/(k_{1r,Si} + k_{2,Si})$ may be a result of decreased $k_{1f,Si}$ and/or increased $k_{1r,Si}$, which yields a decreased $k_{2,Si}$ if the relationship of $k_{1r,Si} + k_{2,Si} = 1$ is as-

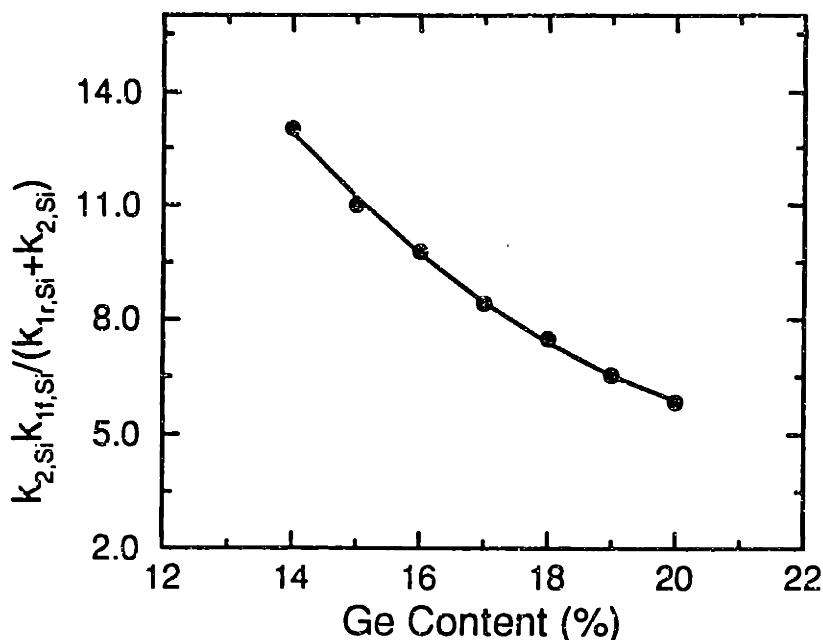

Figure 5.10: Germanium dependency of the extracted $k_{2,Si}k_{1f,Si}/(k_{1r,Si}+k_{2,Si})$ from Fig. 9.

sumed [36]. Thereby, if hydrogen desorption is not the rate-determining step in the growth of $Si_{1-x}Ge_x$ when more germanium atoms are added, the deposition may be determined by the decreased reaction probabilities of processing gases. The inhibited surface reaction can be speculated as an outcome of germanium-enhanced desorption of silicon and germanium hydrides.

For comparison of different rate-limiting step, additionally, we show the silane dependency of $Si_{1-x}Ge_x$ growth rate with $x = 0$ and 0.05, where hydrogen desorption is considered important. The sublinear curves for silicon and $Si_{0.95}Ge_{0.05}$ growth rates versus silane pressure are fit utilizing equations (5.19) and (5.27), assuming surface coverage of hydrogen associated with SiH and GeH are dominant. Excellent agreements exhibited in Fig. 5.10 show that $k_{2,Si}^2k_{1f,Si}/k_{5,Si}(k_{1r,Si}+k_{2f,Si})$ increases with germanium composition. Since $k_{5,Si}$ is the dominating parameter, it is concluded that $k_{5,Si}$ increases as germanium increases, which is qualitatively

consistent with the behavior of modified $k_{6f,H}$ due to germanium addition.

It should noted here that the identity of equation (5.21) bridges the components of silicon and germanium growth rate, R_{Si} and R_{Ge}, and greatly simplifies the silane or germanium dependencies of the overall growth rate. Indeed, the individual components of R_{Si} $((1-x)R)$ and $R_{Ge}(xR)$ can be expressed as functions of P_{SiH_4} and P_{GeH_4} and sublinear relations at 570 - 700°C were defined, similar to the entire growth rate shown in Fig. 5.9. However, since the surface coverage consists of both silicon- and germanium-related species, decoupling the reaction parameters of silicon and germanium hydrides appears unlikely. Equation (5.21) leads to a possible comparison of reaction parameters of silicon for varied germanium contents, though obtaining individual parameter is still difficult. Nevertheless, the data we measured exhibits that the degraded $Si_{1-x}Ge_x$ growth rate in certain situations are due to the decrease of reaction or sticking probabilities.

5.5 Conclusion

This paper has examined germanium incorporation and $Si_{1-x}Ge_x$ growth rate as functions of temperature, hydrogen pressure, and total deposition pressure, silane partial pressure + germane partial pressure, using a VLPCVD reactor. A slight decrease of germanium incorporation was observed as temperature, hydrogen flow, or deposition pressure was increased. Germanium incorporation as a function of germane fraction was compared for UHVCVD, VLPCVD, and LPCVD employing silane and germane with or without hydrogen carrier gas, and similar trends were observed at 550 - 750°C under 1 - 100 mTorr.

The measured $Si_{1-x}Ge_x$ growth rates in the temperature regime from 570 - 700°C exhibit different dependencies on germanium at different temperatures. In general, the deposition rate was enhanced when germanium composition was low, but was degraded with further increasing the amount of germanium Different from

pure silicon epitaxial growth, the measured growth rates of $Si_{1-x}Ge_x$ heteroepitaxy show nonlinear Arrhenius temperature dependencies. The overall activation energy was observed to decrease as germanium increases. The measured increased and subsequently decreased growth rate and modified activation energy suggest that the rate-determining step was altered by increasing germanium incorporation. The possible different rate-limiting steps responsible for the complicated germanium dependency of growth rate were further examined by varying hydrogen and total deposition pressure. The increase of hydrogen carrier gas led to small reduction in $Si_{1-x}Ge_x$ growth rate, but appeared to have no consistent effect on it. The total deposition pressure was found to have significant influence on the growth kinetics. The growth rate was enhanced by raising total deposition pressure. Moreover, the degree of enhancement was germanium dependent; it becomes more pronounced as germnaium content increases.

Suggested by the published literatures and supported by the experimental results in this work, two mechanisms were assumed to explain the overall growth behavior. The model we propose to explain our observations allows the comparisons of measured data and key parameters of growth rate. It is reasoned that when germanium composition or deposition temperature is low, hydrogen desorption is the slowest step and is accelerated by germanium. While when germanium composition or deposition temperature is high and hydrogen desorption becomes not dominant, the incorporation of germanium leads to a decrease in the reaction probabilities of silane and germane, thus degrading the growth rate. The changes of sticking probabilities of silicon and germanium hydrides also affect the dependency of $Si_{1-x}Ge_x$ growth rate on deposition pressure. When germanium is increased, the deposition rate is greatly enhanced by deposition pressure, and this help to explain why monotomic increase of $Si_{1-x}Ge_x$ growth rate is routinely observed in CVD reactor operated at higher pressures (e.g., reduced and atmospheric pressures).

Chapter 6

In-Situ Doping of $Si_{1-x}Ge_x$

6.1 Introduction

In recent years, growth of strained $Si_{1-x}Ge_x$ layer on silicon has become a hot topic because bandgap discontinuities between $Si_{1-x}Ge_x$ and silicon allows for the design of novel and high performance devices with the Si-based technology. New applications such as heterojunction bipolar transistors, modulation doped field effect transistors, and bipolar inversion channel field effect transistors with $Si_{1-x}Ge_x$/Si heterostructures have been demonstrated [6]. Small-geometry devices requires low temperature epitaxial growth process with minimal autodoping and dopant redistribution, and with flexible *in situ* doping capability for absolute control of vertical doping profile within a few monolayer angstroms. Although molecular beam epitaxy (MBE) allows precise control of complicated doping profiles, its wide applications are limited by its expense, complexity, and throughput. In addition, the doping is not flexible and suffers from the inability to achieve high active doping levels using typical Si MBE dopant species such as Ga and Sb [6]. Therefore, chemical vapor deposition (CVD) is attractive. Recently, work on *in situ* doped $Si_{1-x}Ge_x$ have been reported [28, 89, 111, 112, 113, 114]. In these researches, for n-type $Si_{1-x}Ge_x$ doping arsine and phosphine were routinely used as dopant source in germane and silane or dicholosilane with/without hydrogen, and doping with

diborane for growing p-type $Si_{1-x}Ge_x$ have also been explored. In this study, we have considered *in situ* doping of $Si_{1-x}Ge_x$ with boron, arsenic, and phosphorus at 620°C in very low pressure chemical vapor deposition (VLPCVD). Results of *in situ* doped silicon epitaxial layers are presented as well for comparisons.

Different from our previous efforts on *in situ* boron and arsenic doped $Si_{1-x}Ge_x$ in multilayer structures where strained layers only existed in growth area of 10μm×10μm [89], here we attempt to grow fully strained $Si/Si_{1-x}Ge_x/Si$ structures with $Si_{1-x}Ge_x$ boron and arsenic doped, which is of practical interest for heterojunction bipolar transistors, on very large area, i.e. 4" wafer. Although we have demonstrated the strained-layer deposition of Si/undoped $Si_{1-x}Ge_x/Si$ structures [116], there is still a need to examine whether or not VLPCVD provides good-quality *in situ* doped $Si_{1-x}Ge_x$ layer at low temperature. Once the capability of strained-layer deposition by VLPCVD was confirmed, we deposited phosphorus-doped $Si_{1-x}Ge_x/Si$ multilayer to gather more information on the interactions of phosphorus and germanium during epitaxial growth. In this case the deposition times for arsenic and phosphorus doped $Si_{1-x}Ge_x$ and Si layers were increased for clearer Ge and doping profiles.

6.2 Experiments

The procedures used to prepare a clean substrate surface prior to $Si_{1-x}Ge_x$ deposition at 620°C have been described in the preceding paper. Depositions for *in situ* doping of $Si_{1-x}Ge_x$ were carried out as follows. After the removal of 12 Å protective oxide, a silicon epitaxial layer was deposited, followed by system cooling from 775°C to 620°C. $Si/Si_{1-x}Ge_x/Si$ with *in situ* boron and arsenic doping into $Si_{1-x}Ge_x$ were grown by introducing silane or germane + silane containing 0-1000 ppm dopant gas, i.e., diborane or arsine, in an 80 sccm hydrogen flow. Silane flow rate was fixed at 20 sccm and germane 0.75 sccm at a deposition pressure of 10

mTorr with hydrogen as a carrier gas. The p- and n-type dopant sources were 1000 ppm diborane or arsine in silane. Dopant fraction in the silane cylinder was verified through analysis by the manufacturer. The dopant concentration in the gas during deposition was varied by mixing silane with 1000 ppm dopant source and pure silane. The deposition times were 5 min for boron-doped $Si_{1-x}Ge_x$ layers, and are 20 and 30 min for arsenic doping with 100 and 1000 ppm, respectively. The undoped silicon capping layers were grown for 30 min.

The dopant source employed for phosphorus doping was 100 ppm phosphine diluted in silane. As for boron and arsenic doping, phosphine in the gas was modulated by mixing silane containing 100 ppm phosphine and pure silane. N-type $Si_{1-x}Ge_x$ and undoped silicon multilayer depositions were performed using various phosphine fractions up to 100 ppm in a constant flow of silane and germane. In each run six $Si_{1-x}Ge_x$ layers separated by undoped silicon layers were grown and phosphine gas-phase fractions during $Si_{1-x}Ge_x$ epitaxy were 0, 1, 3, 10, 30, 100 ppm for each layer, increasing from the bottom. For different runs germane/silane ratios employed were 0, 1.25%, 2.50%, 3.75%, 5.00%, and 6.25% in a 50 sccm silane flow. At 620°C the first undoped $Si_{1-x}Ge_x$ layer and the subsequent silicon layer were grown for 5 min; while, considering the growth rate depression from phosphorus doping and residual phosphine that may exist in the reaction chamber after being turned off, the growth times of doped $Si_{1-x}Ge_x$ and undoped silicon spacer layer were held at 20 min. Typical pressures during deposition are 6.5 – 7.5 mTorr,

Cross-sectional transmission electron microscopy (XTEM) was used to characterize the thickness and structural quality of the as-grown films. Double-crystal X-ray diffraction techniques were also utilized to evaluate the crystalline quality of two boron-doped $Si_{1-x}Ge_x$ films for comparing XTEM results. Germanium composition was measured by Rutherford backscattering spectrometry (RBS) and secondary ion mass spectrometry (SIMS). Germanium, boron, arsenic, and

phosphorus depth profiles were assessed by SIMS. Layer thicknesses in multilayer phosphorus-doped structures measured by RBS and SIMS were verified by XTEM with errors within 100Å for $Si_{1-x}Ge_x$ layers of 2000 – 4000Å thick (20 min depositions) and 40Å for silicon and $Si_{1-x}Ge_x$ layers of 500 – 1300 Å (5 min depositions). Previously, our comparisons between SIMS and XTEM suggested the errors on growth rates were less than 25 Å for the boron doped and 50 Å for the arsenic doped with thicknesses of about 500 and 250 – 400Å, respectively [89].

6.3 Results

The XTEM micrographs of Si/p-$Si_{1-x}Ge_x$/Si structures grown from mixtures of silane-germane-hydrogen containing 25 and 1000 ppm diborane are shown in Fig. 6.1 (a) and (b). Germanium content obtained by RBS are 0.132 and 0.128. Si/n-$Si_{0.87}Ge_{0.13}$/Si doped from 100 and 1000 ppm AsH_3 diluted in processing gases are shown in Fig. 6.2 (a) and (b). One feature noted here is the smooth morphology of these epitaxial layers, which contrasts the previous VLPCVD arsenic doping of pure silicon epitaxial layer [117]. At a deposition temperature of 800°C, differential interference contrast images of surfaces of deposited silicon layers exhibited that the morphology of as-deposited film appeared rough when arsine gas-phase concentration exceeded 10 ppm at very low pressure, and the surface morphology were exacerbated by reducing the temperature to 750 and 700°C. However, it was demonstrated that arsine *in situ* doping of $Si_{1-x}Ge_x$ did not incur surface morphology degradation at 625°C [89].

SIMS depth profiles of the most heavily n- and p-type $Si_{1-x}Ge_x$ layer in Fig 6.1 and 6.2, 2×10^{20} boron atoms/cm^3 and 5×10^{19} arsenic atoms/cm^3, are exhibited in Fig. 6.3. Clearly, boron and arsenic chemical concentrations in $Si_{1-x}Ge_x$ films exceeding 10^{19} cm^{-3} in bulk were achieved, and the presence of any associated extended defect such as dislocation or stacking fault was under the detection

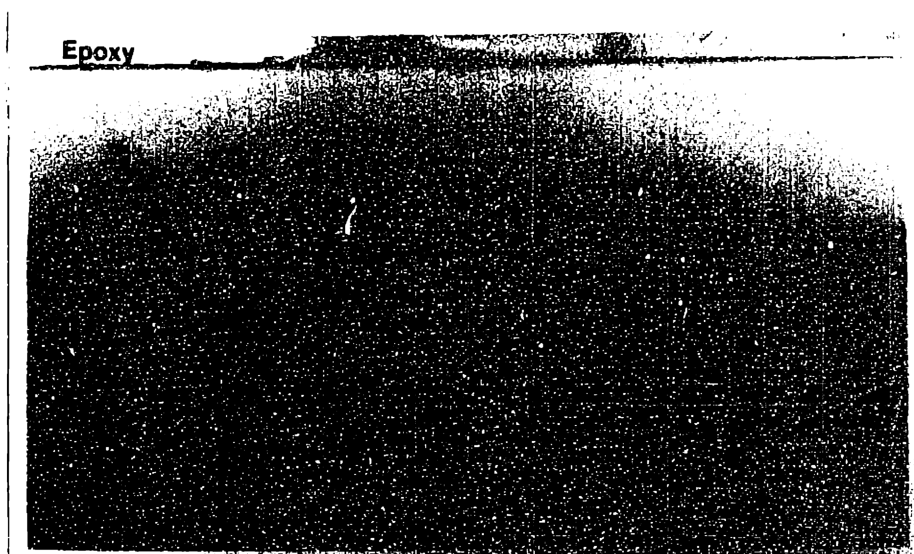

(a)

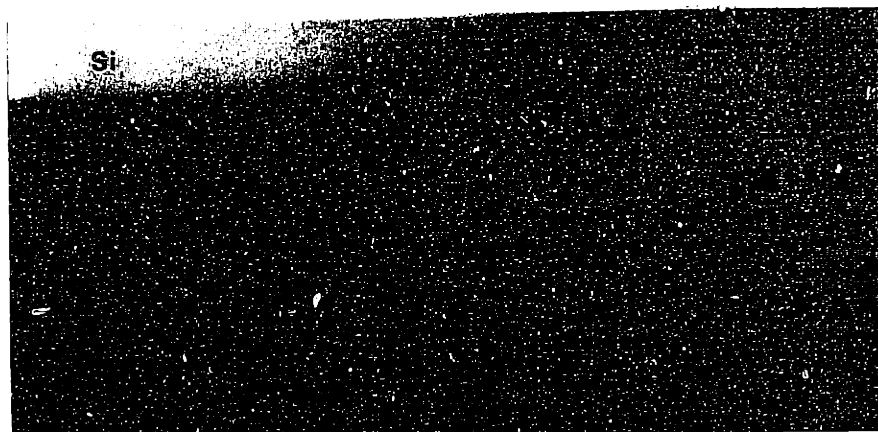

(b)

Figure 6.1: Cross-sectional transmission electron microscopy images of Si/boron-doped $Si_{1-x}Ge_x$/Si heterostructures with (a) $x = 0.13$, 25 ppm diborane in silane, and (b) $x = 0.13$, 1000 ppm diborane in silane; silane flow = 20 sccm, germane flow = 0.75 sccm, and hydrogen flow = 80 sccm.

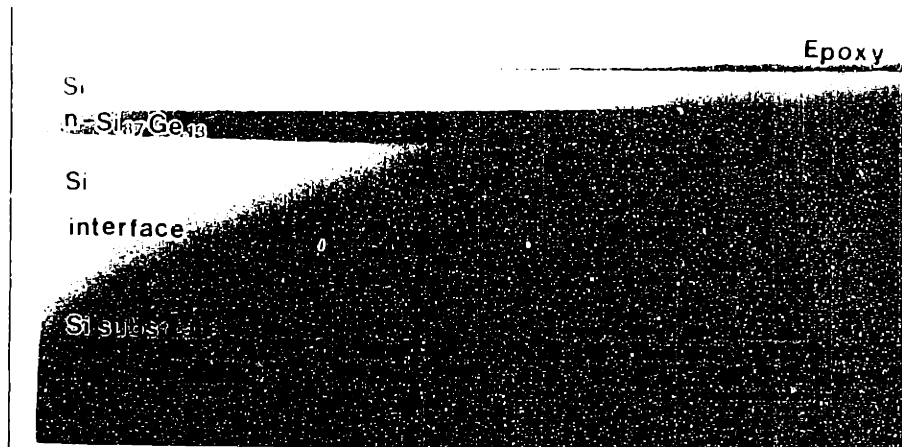

(a)

(b)

Figure 6.2: Cross-sectional transmission electron microscopy images of Si/arsenic-doped $Si_{0.87}Ge_{0.13}$/Si heterostructures with (a) 100 ppm arsine in silane, and (b) 1000 ppm arsine in silane; silane flow = 20 sccm, germane flow = 0.75 sccm, and hydrogen flow = 80 sccm.

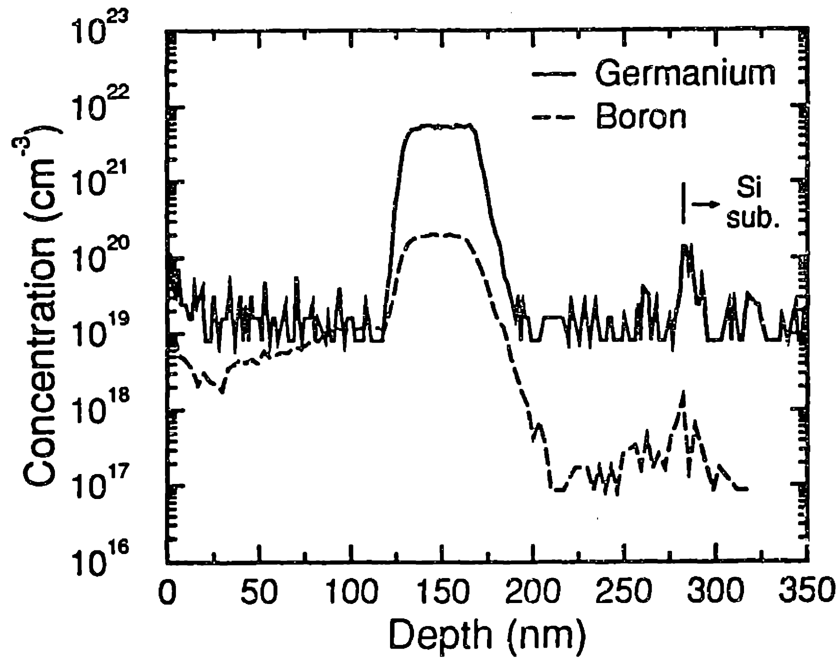

(a)

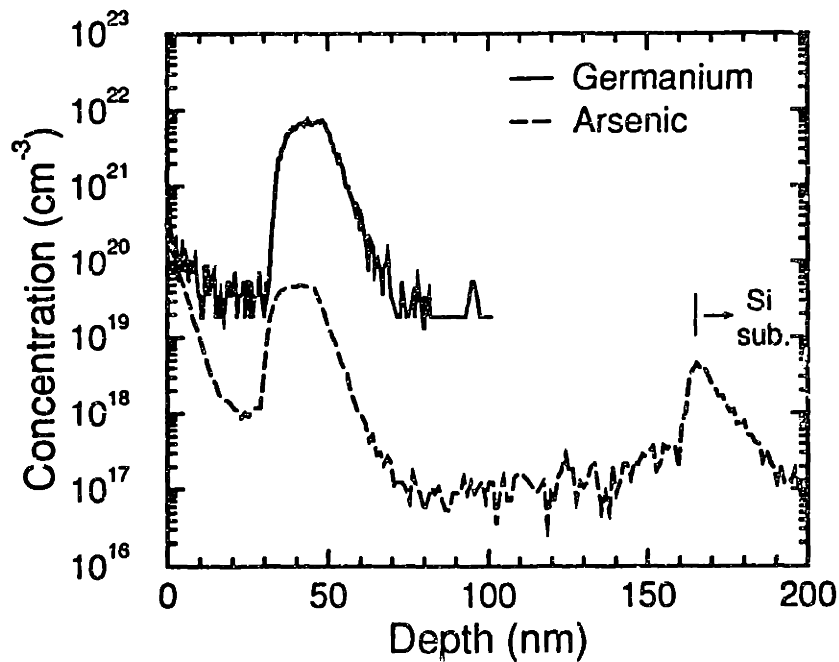

(b)

Figure 6.3: Secondary ion mass spectrometry depth profiles of dopant and germanium in (a) Si/boron-doped $Si_{0.89}Ge_{0.13}$/Si shown in Fig. 6.1 (b), and (b) Si/arsenic-doped $Si_{0.89}Ge_{0.13}$/Si shown in Fig. 6.2 (b).

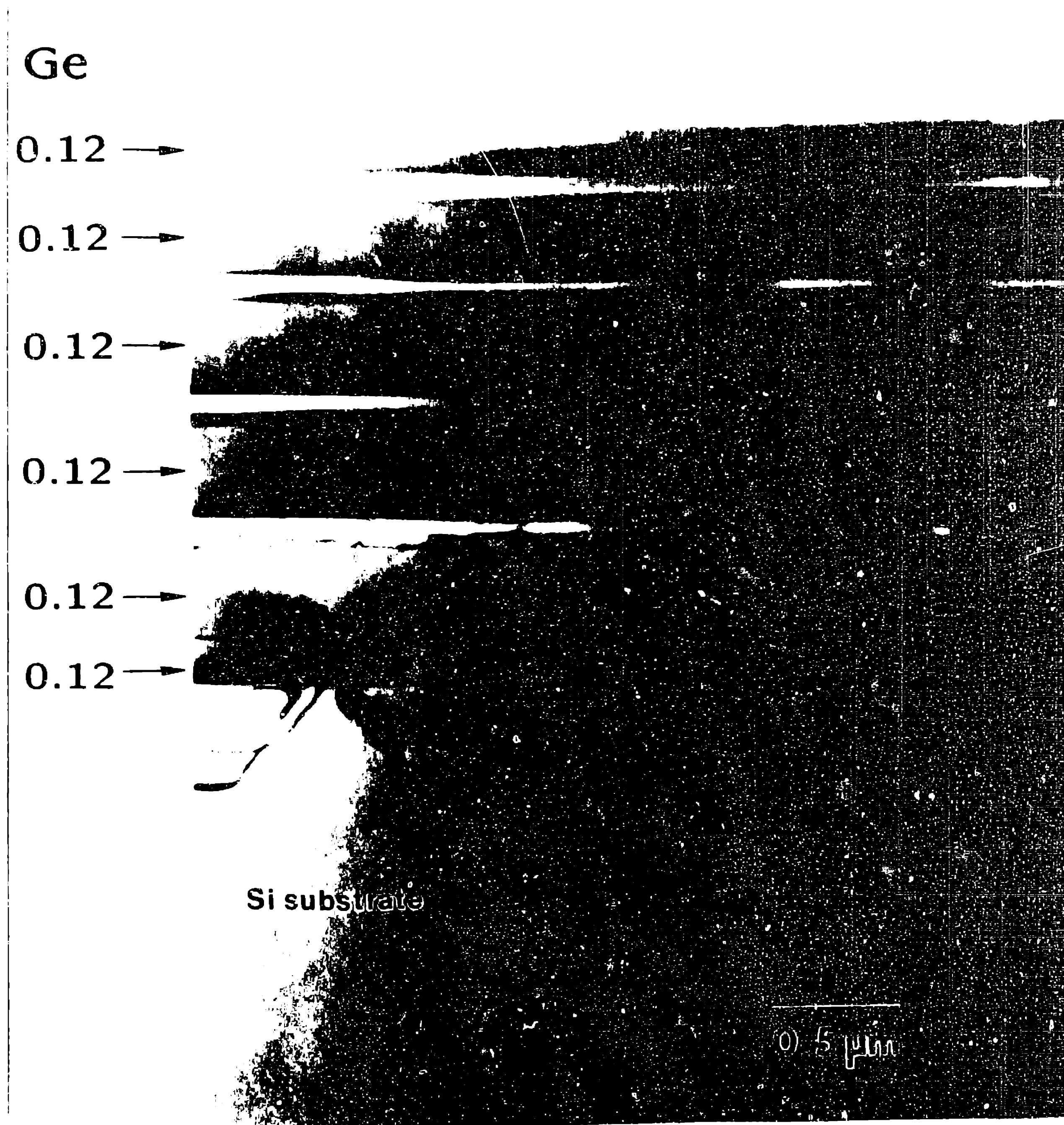

Figure 6.4: Cross-sectional transmission electron microscopy images of phosphorus-doped $Si_{0.88}Ge_{0.12}/Si$ multilayer structures; silane flow = 50 sccm, germane flow = 0.75 sccm, and phosphine fractions are 0, 3, 10, 30, and 100 ppm in silane.

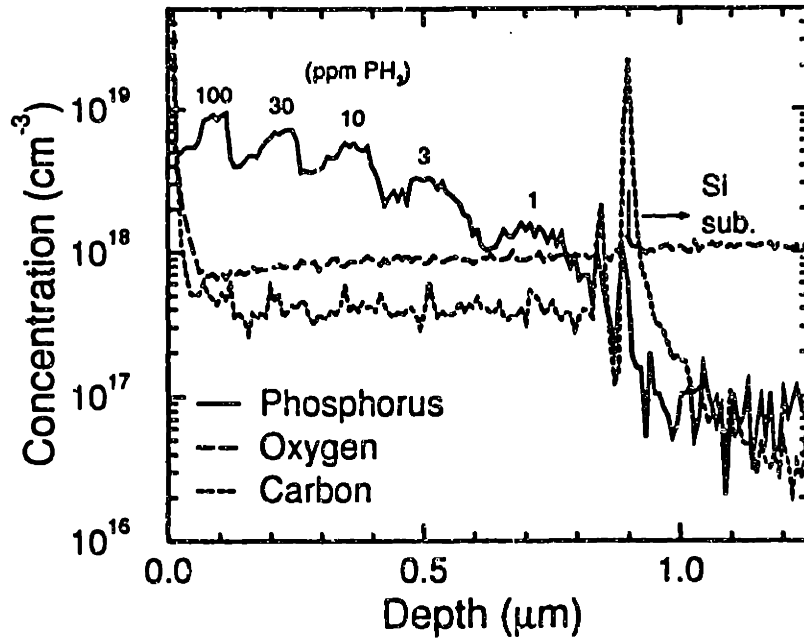

(a)

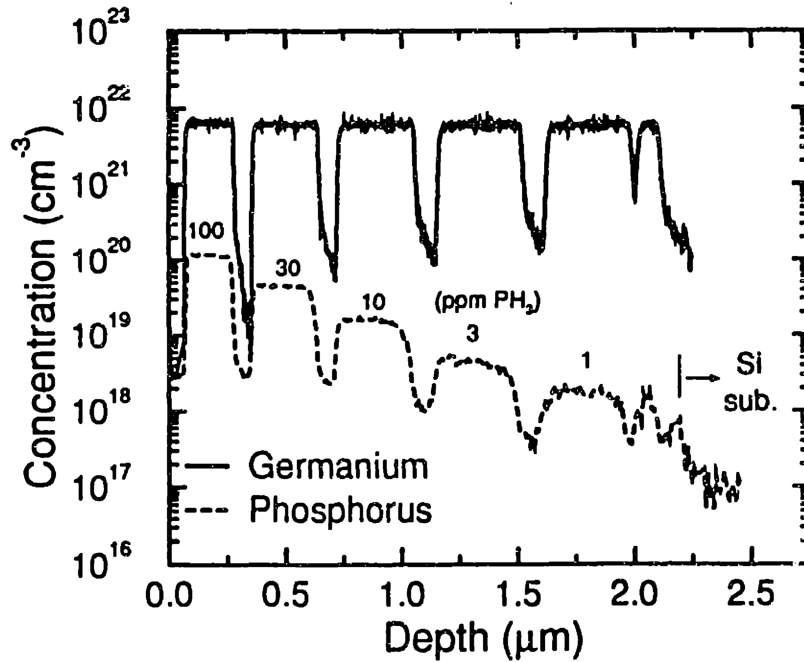

(b)

Figure 6.5: Secondary ion mass spectrometry depth profiles of germanium and/or phosphorus in (a) phosphorus-doped Si/Si, and (b) phosphorus-doped $Si_{0.88}Ge_{0.12}/Si$ multilayer structures shown in Fig. 6.4.

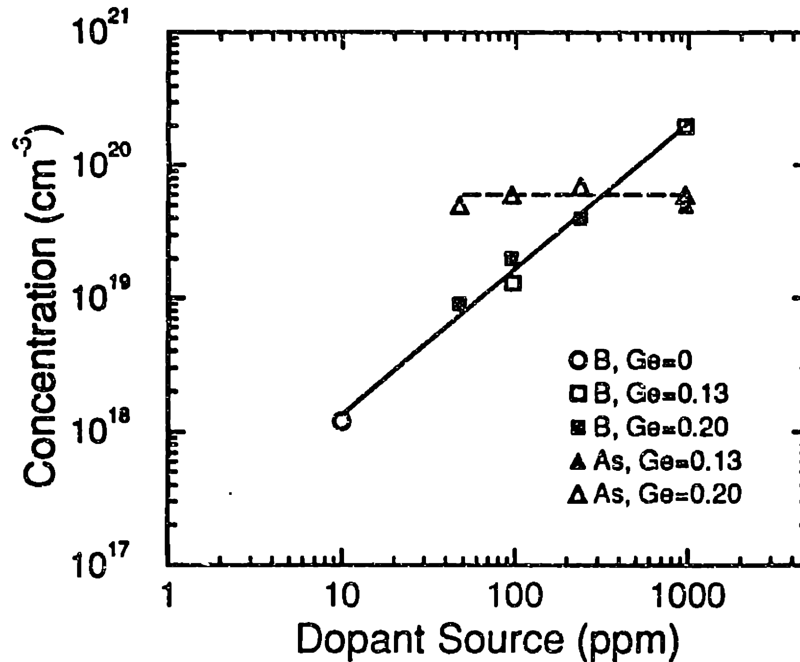

Figure 6.6: Boron and Arsenic incorporation as a function of gas-phase dopant fraction for varied germanium contents.

limit of XTEM, 10^5 - 10^8 cm^{-2}, as demonstrated in Fig. 6.1 and 6.2. Furthermore, DCD proved excellent quality in boron-doped $Si_{1-x}Ge_x$ layers.

Figure 6.4 presents the XTEM images obtained from phosphorus-doped $Si_{0.88}Ge_{0.12}/Si$ multilayered structure. The interfaces of $Si_{1-x}Ge_x$ and silicon were determined by more than one micrographs, since some of them are not evident in the present figure. Misfit as well as threading dislocations were observed and, similar to the $Si_{1-x}Ge_x/Si$ multilayered structure with germanium increasing from substrate grown by ultrahigh vacuum chemical vapor deposition (UHVCVD) [27], cumulative compressive stress in this $Si_{0.88}Ge_{0.12}/Si$ structure also led to the nucleation of extensive dislocation network around the bottom $Si_{1-x}Ge_x/Si$ interface. However, the top two layers remained highly perfect though partially relaxed. Phosphorus incorporation profiles probed by SIMS in an n-Si/i-Si modulation doping structures, where i represents undoped, and in the $Si_{0.88}Ge_{0.12}/Si$ struc-

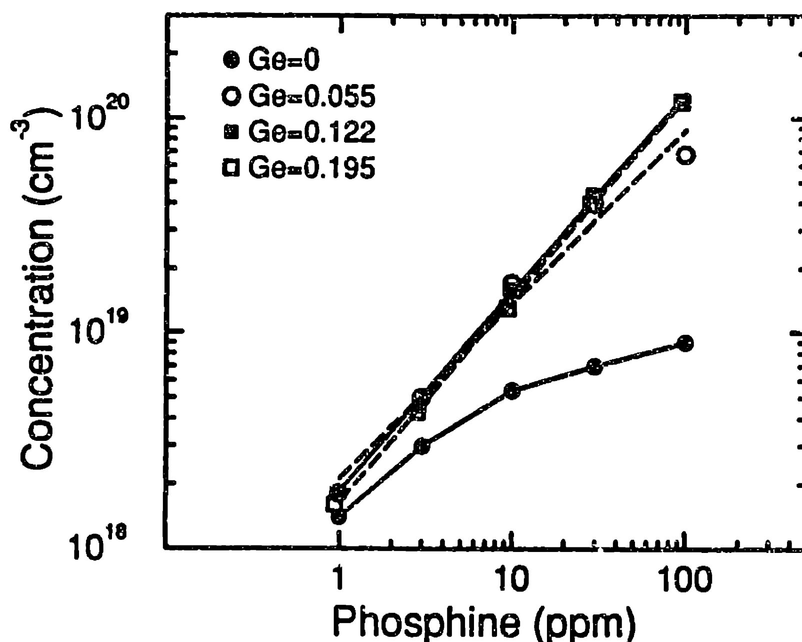

Figure 6.7: Phosphorus incorporation as a function of gas-phase dopant fraction for varied germanium contents.

turers are compared in Fig. 6.5 (a) and (b). Incorporated germanium profile in the $Si_{0.88}Ge_{0.12}$/Si multilayer is also exhibited in Fig. 6.5 (b), and germanium composition in $Si_{1-x}Ge_x$ was found to be independent on phosphine addition. The tremendous difference of phosphorus doping behavior in silicon and $Si_{1-x}Ge_x$ is evident from Fig. 6.5 (a) and (b); with phosphorus incorporation range and depth profile greatly improved in $Si_{1-x}Ge_x$ film.

Figures 6.6 and 6.7 summarize the observed total dopant incorporation results as a function of gas-phase diborane, arsine, and phosphine for various germanium content. The data of boron incorporation in $Si_{1-x}Ge_x$ with germanium compositions of 0, 0.13, and 0.20, and all fall in the same straight line, suggesting boron doping behavior is not affected by germanium. However, more phosphorus atoms are doped into $Si_{1-x}Ge_x$ than into pure silicon, but the germanium dependency of phosphorus incorporation is not very clear with phosphine at or less than

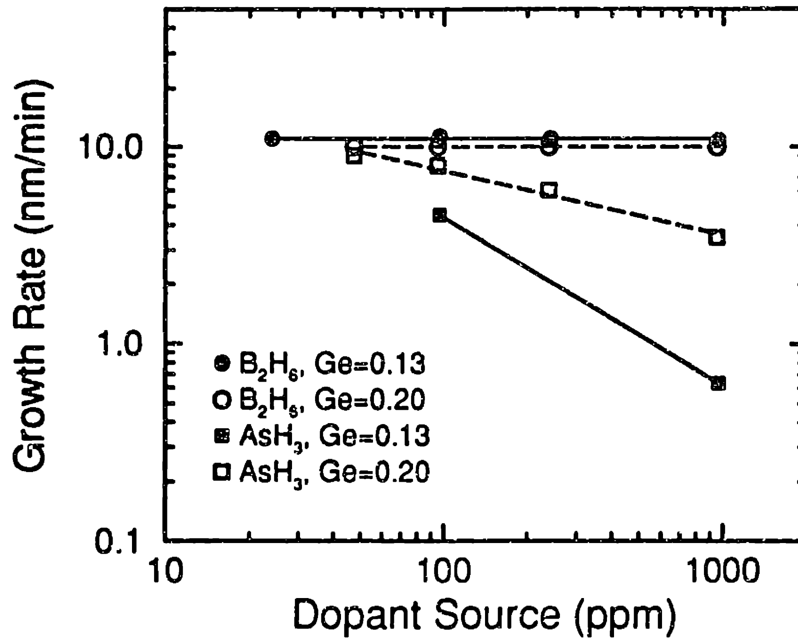

Figure 6.8: Growth rate as a function of gas-phase diborane and arsine fraction for varied germanium content.

30 ppm. It is observed that boron and phosphorus incorporation increase in proportional to gas-phase dopant fraction, while arsenic doping appears saturated in the range of 50 – 1000 ppm arsine. In the cases of boron and phosphorus doping, an empirical relation is obtained

$$[DS] = A[DG]^a, \tag{6.1}$$

where [DS] and [DG] are the dopant fraction in solid and gas phase, respectively, and A and a could be referred as constants.

Figures 6.8 and 6.9 compare the growth trend of *in situ* boron, arsenic, and phosphorus doped $Si_{1-x}Ge_x$ layer determined by dopant gas concentration for different germanium compositions. No consistent variation in the deposition rate was measured for the increase of diborane fractions, whereas the deposition rate was diminished due to the presence of arsine and phosphine. However, the degradation of growth rate was eliminated by adding germanium. In all cases,

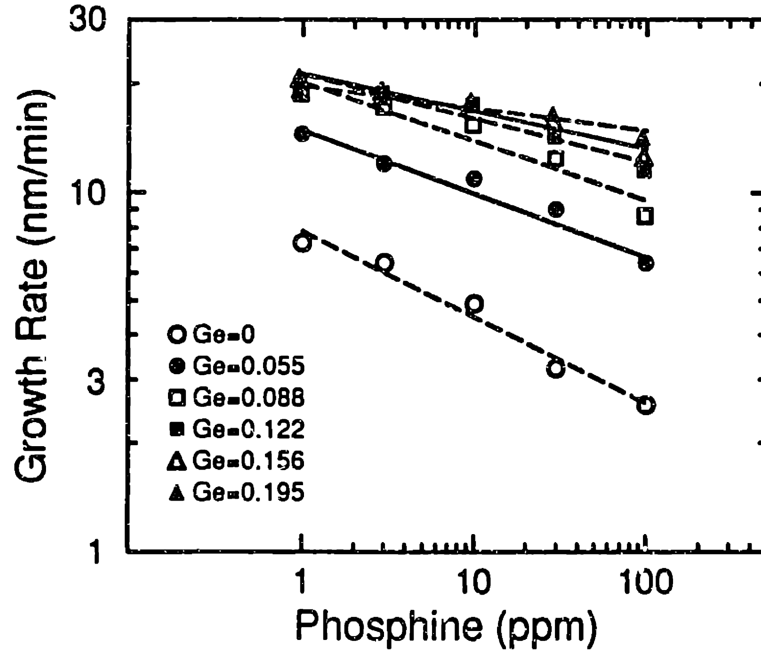

Figure 6.9: Growth rate as a function of gas-phase phosphine fraction for varied germanium content.

dopant dependency of growth rate could be defined as

$$R = B[DG]^{-b}, \tag{6.2}$$

where R is growth rate, B and b are constants.

6.4 Discussion

6.4.1 Boron Doping

In Fig. 6.6, we found that boron incorporation is best described by equation (6.1) with $a \sim 1$ and A = 2. Thus, the effective segregation coefficient defined as [120]

$$k_{eff} = \frac{[DS]}{[DG]} \tag{6.3}$$

gives k_{eff} of 2, implying the value of k_{eff} is no longer limited to the maximum value of 1 and the equilibrium conditions may be violated [119]. Interestingly, we found

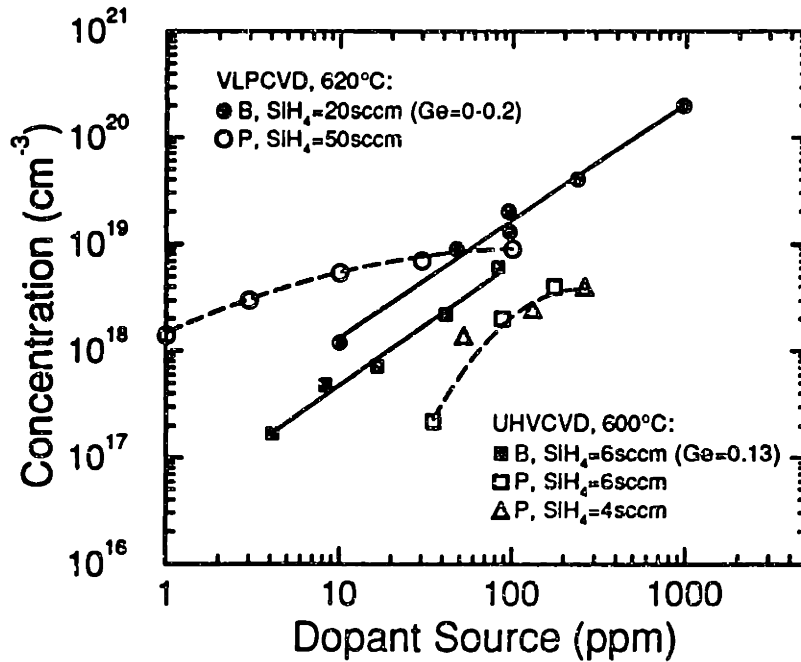

Figure 6.10: Comparison of boron and phosphorus incorporation in VLPCVD at 620°C and UHVCVD at 600°C.

the linear relationship of dopant incorporation and dopant partial pressure is also valid for boron doping in $Si_{1-x}Ge_x$ deposition with UHVCVD [111]. Figure 6.10 compares the *in situ* boron doping in VLPCVD and UHVCVD. In both studies boron concentration was measured by SIMS, and the amount of boron doped into $Si_{1-x}Ge_x$ layer in UHVCVD is lower by half-order of magnitude compared to VLPCVD. The measured boron incorporations in both VLPCVD and UHVCVD are found to approach to, and in some cases exceed, the solid solubility of boron in silicon at the deposition temperatures [121]. This suggests boron incorporation at or below very low pressure is kinetically, rather than thermodynamically, controlled.

From Fig. 6.8, no change in the growth rate of $Si_{0.87}Ge_{0.13}$ by introducing diborane was observed. The independency of $Si_{1-x}Ge_x$ growth rate on diborane has also been mentioned in a report on UHVCVD employing the same processing

gases [111]. In a study of doping reaction of diborane with (100) silicon surface, diborane was reported to have a very small sticking coefficient ($< 10^{-4}$) and the coverage is low and further accumulation of boron failed [118]. No thermal desorption of boron was observed and the desorption of hydrogen opened more sites for adsorption, leading to a more efficient way to deposit boron on silicon. Hence, a stable growth took place and very flat doping profile was realized, as demonstrated in Fig. 6.3 (a). However, though the turn-on transient of boron incorporation in Fig. 6.3 (a) appears sharp, indicating accurate control of box-like, symmetrical profile is hindered by the remnant boron in the nominally undoped silicon capping layer. Compared to the relatively sharp upward doping transient, the slow downward doping transient that never recovered to the original level was believed, in a previous work on B doped Si epitaxy using the same VLPCVD reactor, to be due primarily to the presence of a significant virtual leak for diborane in the gas delivery system [119]. However, it is still problematic even after we upgrade the mass flow controller, and; therefore, we speculate that the major contribution to the undersired turn-off transient is a result of gas-phase autodoping within the reaction chamber, rather than a leakage problem. Desorption of boron from deposited layer on inner walls of chamber might give rise to residual doping. This supposition can be further supported by the measured interfacial boron and germanium peaks at the Si/Si-substrate interface, indicating that autodoping owing to desorption from chamber surface during bakeout becomes a concern in VLPCVD. Fortunately, the interfacial peaks resulted from memory effect in VLPCVD can be reduced by coating the chamber walls and susceptor between two runs.

6.4.2 Arsenic and Phosphorus Doping

The results of doping with arsine and phosphine during silicon and $Si_{1-x}Ge_x$ epitaxial growth exhibited in Fig. 6.6 – 6.9 are much more complicated than the doping with diborane. Previous reported arsenic doping data from VLPCVd films that

implied a saturation of arsenic incorporation beyond arsine fraction of 50 ppm is questionable [89], because the arsenic signal generated in SIMS measurement was obscured by germanium of the same mass. The arsenic mass was acquired by monitoring the $AsSi^{-1}$ molecular ion, and unfortunately several GeSi molecular ions occurred at the same mass. Thus, the arsenic signal has had the germanium signal subtracted from it to correct for this interference, and the accuracy of arsenic concentration is in doubt. Measurement of phosphorus incorporation did not suffer from this interference and is more reliable.

Figure 6.7 indicates the value of a in equation (6.1) is less than 1, but is approaching to 1 as germanium content increases. The magnitude of A is about 1.6 and is approximately independent on germanium. The effective segregation coefficient k_{eff} in Fig. 6.7 was found to far exceed 1, and it is taken as evidence that phosphorus incorporation is not under equilibrium conditions at very low pressure at 620°C.

Figure 6.10 compares the incorporated phosphorus concentration in epitaxial silicon grown by VLPCVD and UHVCVD. The UHVCVD data was obtained by $C(V)$ measurement on metal-oxide-semiconductor capacitor, therefore represents the concentration of ionized dopants. Since the percentage of ionized phosphorus is not available, direct comparison of chemical concentration of dopant between these two reactors is difficult. Nevertheless, it is interesting to note that the incorporation trends in both cases differ from boron doping, where both VLPCVD and UHVCVD show similar behaviors, and wider range of phosphorus dopant is given by UHVCVD. It is possible that under ultrahigh vacuum phosphorus coverage is lower and the block of surface sites is less severe; therefore, more phosphorus dopants can be incorporated as discussed later.

The observed growth-rate reduction of silicon layer decreased by phosphine observed in both VLPCVD and UHVCVD are presented in Fig. 6.11. The value of b in equation (6.2) is measured to be 0.24 and ~ 0.34 for VLPCVD and UHVCVD,

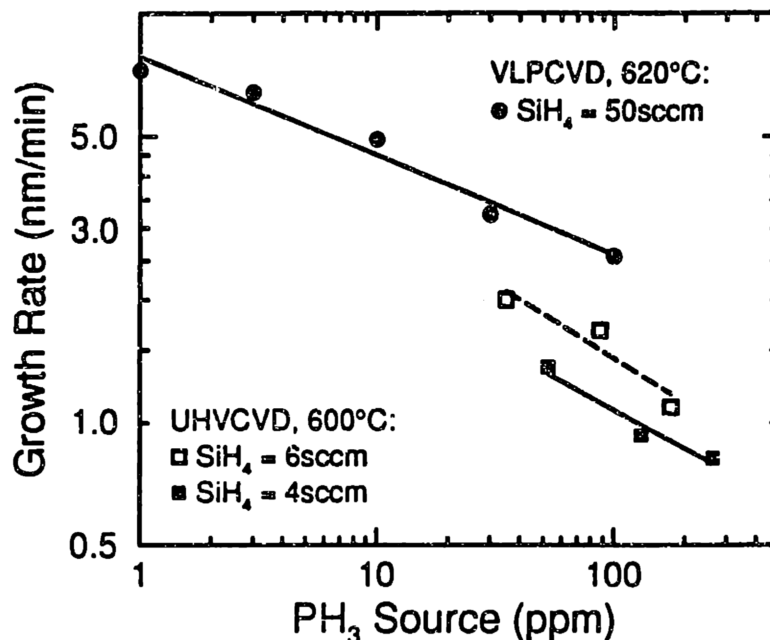

Figure 6.11: Comparison of phosphorus-doped silicon growth rate in VLPCVD at 620°C and UHVCVD at 600°C.

respectively. The different phosphine dependency of growth rate may imply different growth mechanism. In VLPCVD, systematic studies were conducted and the magnitude of b was found to change with the addition of germanium, as shown in Fig. 6.9. In this section, we shall briefly review the reported mechanisms accounting for the inhibited arsenic and phosphorus dopant incorporation and associated growth rate. We focus on the enhanced process of phosphorus doping by germanium addition, since more data are available for comparing the proposed model and experimental results.

The surface reaction of phosphine on silicon (100) surface has been studied by surface analytical techniques [118]. It was reported that phosphine chemisorbs readily either nondissociatively at room temperature or dissociatively with the formation of silicon-hydrogen bonds at elevated temperatures. In contrast to diborane adsorption, phosphine has very high sticking coefficient in the order of unity

and is stable once adsorbed on silicon surface. The preferential adsorption of phosphine on the silicon surface inhibits the adsorption and subsequent decomposition of silane. At 400°C and above, hydrogen is desorbed from the adsorbed overlayer, leaving phosphorus adatoms on the surface. The thermal desorption of hydrogen opens up some available silicon sites on surface for further phosphine adsorption. Upon further heating, hydrogen continues to evolve and the saturation phosphorus coverage increases until ~ 550°C at which point the coverage of phosphorus is close to the density of silicon surface atoms and a complete monolayer of adsorbed phosphorus forms. At temperatures above 550°C, thermal desorption of the adsorbed phosphorus atoms start to occur, primarily as P_2 molecules. This desorption slowly reduces the surface coverage of phosphorus, but even at 800°C the coverage can be very high. The blocking of silicon surface by phosphorus atoms was thought to inhibit the silane molecule from reacting with the silicon surface, leading to the severe reduction of the silicon growth rate in a CVD reactor when introducing small amount of phosphine in the silane flow.

In a report on electronic and atomic structure of arsenic terminated silicon (100), a comparison between angle resolved photoemission data and *ab initio* pseudopotential calculations demonstrated that the 2×1 reconstruction of the silicon(100):arsenic surface is caused by As-As dimerization whose bond length is predicted to be 2.55$\AA$ [123]. In this model, arsenic atoms form symmetrical dimers on top of the silicon surface. Each arsenic atom bonds to twp silicon atoms and to the other arsenic atom of the dimer. This leaves the arsenic atoms with a doubly occupied long-pair state making the arsenic atoms fully coordinated. Because of the full coordination, the arsenic adatoms act as a passivation layer and adsorption of other hydrides is highly hindered. The formation of dimer and its implications on growth and incorporation processes was further interpreted in an investigation of arsenic doping in VLPCVD [117]. In that study, it was proposed that only monatomic adsorbed arsenic can be incorporated and, therefore, the measured

dopant concentration in the layer is much lower than the surface concentration of arsenic adatoms, which exist mostly in the dimer form, and becomes saturated as the gas-phase concentration is increased. It was speculated further that, since these dimers cannot be directly incorporated, they may also serve as pinning sites for step-flow growth process and thus be responsible for the morphological aberrations observed on arsenic-doped epitaxial silicon layer. Arsenic doping enhanced by plasma was contributed to ion-bombardment-induced disruption of As-As dimerization, leading to more atomic arsenic, which will be readily incorporated into the layer growth process. In addition, the surface passivation caused by high surface coverage of As-As dimers is greatly reduced, and continuous layer-by-layer growth is not disturbed by arsenic dimers on the surface. As a result, the breakup of arsenic dimers dramatically promoted arsenic incorporation, and improved surface morphology and the growth rate.

Because of their chemical similarity, the As-As dimer model may be applicable to phosphine-silane mixtures. This is supported by the observation that P_2 is the major species probed during desorption from a highly saturated surface. Note that the dimers are expected to present when the surface coverage of arsenic or phosphorus atoms is high. The desorption of monatomic P has been reported as well [112], and it was suggested, though not conclusively, that desorption of P is more abundance than P_2 in UHVCVD because of lower surface coverage of phosphorus. Physically, when the fraction of phosphorus adatoms is small, there will be little chance for interaction of phosphorus atoms to form P-P dimer and desorbed as P_2. The desorption rate of P_2 would be small for low phosphorus coverage and increase rapidly as the coverage increases.

In this work the observed enhancement for phosphorus-doped epitaxial growth due to germanium addition may be associated with the suppression of P-P dimerization. It is very possible that germanium modifies the electronic and atomic structure of phosphorus-covered $Si_{1-x}Ge_x$ surface surface and affects the doping

behaviors of phosphorus. For example, since the chemical potential of silicon may be related to the Fermi level within the semiconductor surface and corresponding band bending at the surface, which influences the adsorption of dopant gas [117], changes in the electronic nature of the surface and silicon bulk owing to germanium incorporation could have significant implications with regard to adsorption of phosphorus and their formation of dimers. In addition, the unequal atomic sizes of silicon and germanium and the tetragonal structure of strained $Si_{1-x}Ge_x$ layer could impose more restrictions on the symmetrical P-P dimerization. Moreover, similar to the accelerated hydrogen desorption caused by germanium desorption of phosphorus may be promoted as well, hence reducing the chance for P-P interaction to form stable dimers. Though in the absence of direct surface analysis, suggested by the results that arsenic and phosphorus did not incur surface roughness in previous [89] and this VLPCVD work, we believe the dimerization of surface phosphorus atoms are depressed. When the P-P dimerization is eliminated, successful epitaxial growth was achieved by continuous two dimensional growth. The supposition that Ge depresses P-P dimerization or reduces surface coverage of phosphorus and accelerates P desorption could be supported by the the observation that germanium also dramatically improved the phosphorus dopant profile, as demonstrated in Fig. 6.5 (b). The presence of Ge is thought to reduce the coverage of P on the substrate, susceptor, quartz wall, and electroplates within the chamber. Therefore, when phosphine is switched off, the residual concentration of P adsorbed on chamber surfaces is lower after $Si_{1-x}Ge_x$ deposition than after Si deposition. Consequently, because of the rapid desorption of P encouraged by Ge after phosphine is terminated, the persistence effect and corresponding autodoping of P in a subsequent deposition diminishes, and a more abrupt dopant profile in $Si_{1-x}Ge_x$ is attained.

Since the majority of phosphorus atoms on the surface may exist in monoatomic form due to germanium incorporation, they will be readily incorporated into the

growing layer, leaving more available silicon sites for subsequent adsorption of silicon and phosphorus hydrides. However, it should be noted that, the catalysted phosphorus desorption by germanium, though inhibits P-P dimer formation and generates more vacant sites, will somehow reduce the population of surface phosphorus on the surface. Thus, the possible dual roles of germanium which (i) increases the density of monatomic phosphorus by hindering P-P dimerization and (ii) decreases the coverage fraction of phosphorus by enhancing phosphorus desorption, have opposite effects on the germanium dependency of phosphorus incorporation and complicates the understanding of the Ge dependency of P incorporation. For example, Fig. 6.7 shows $Si_{0.945}Ge_{0.055}$ has a higher phosphorus incorporation than $Si_{0.805}Ge_{0.195}$ with 1 ppm PH_3, while the reverse is true as phosphine is increased up to 100 ppm. It seems likely that when phosphine flow or phosphorus coverage is low, desorption of phosphorus is more dominant in the incorporation process and the phosphorus concentration is lower in the layer with more germanium. As phosphine fraction or surface coverage increases, the interaction of surface phosphorus becomes significant and the increased germanium will mainly contribute to disrupt the formation of P-P dimer. As a result, more phosphorus atoms were found in $Si_{1-x}Ge_x$ containing more germanium. Although the magnitude of phosphorus incorporation has complicated relationship with germanium composition, it was observed that the value of a in equation (6.1) increases consistently with germanium content, as shown in Fig. 6.13, suggesting the incorporation is more phosphine dependent as germanium content increases.

Note that even though germanium may simultaneously have opposing effects on phosphorus incorporation, both roles germanium play will open up more vacant sites on the silicon surface. Thus, it is expected that the growth rate of phosphorus-doped $Si_{1-x}Ge_x$ will increase with increasing germanium content. Combining the deposition rate of silicon epitaxial layer, we replot Fig. 6.9 for $Si_{1-x}Ge_x$ growth rate as a function of germanium, as shown in Fig. 6.12, and find

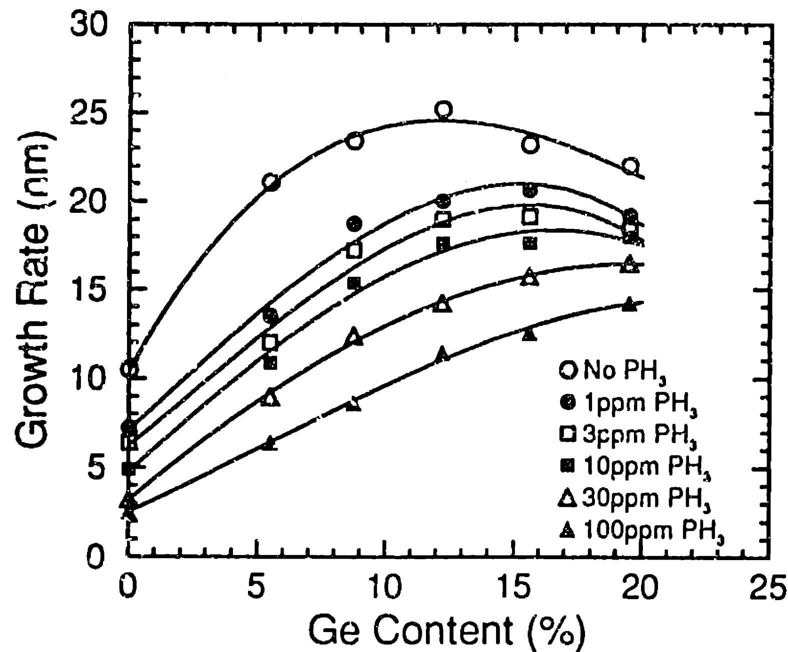

Figure 6.12: $Si_{1-x}Ge_x$ growth expressed as a function of germanium composition for varied phosphine gas-phase fraction. The position of growth-rate peak changes with phosphine fraction.

that with higher phosphine fraction the measured growth rate indeed increases monotonically as germanium content increases. The observed falloff of growth rate with less phosphine flow is believed to be a result of decreasing sticking probabilities of reaction hydrides which becomes determining when surface coverage is no longer the rate-limiting step, as discussed in the preceding paper. Therefore, Fig. 6.12 can be looked as the evidence supporting our speculation that germanium reduces the surface coverage of phosphorus. When phosphorus coverage is reduced by germanium, the growth rate increases with increasing germanium. When the limit of phosphorus coverage on growth rate is relaxed by adding more germanium, the decreased reaction probabilities caused by germanium content become determining and reduce the growth rate. For lower phosphine flow, germanium can easily recover the reactive surface, while more germanium is required to restore the surface reactivity as phosphine fraction is increased. Thus, the peak in growth

rate appears to be a function of phosphine fraction.

Based on the above discussion, we further analyze the process of phosphorus doping by considering the following reactions:

$$PH_{3(g)} + 4_ \xrightarrow{k_1} \underline{P} + 3\underline{H}, \tag{6.4}$$

$$n\underline{P} \xrightarrow{k_2} P_{n(g)} + n_, \tag{6.5}$$

and

$$\underline{P} \xrightarrow{k_3} P_{(ss)} + _, \tag{6.6}$$

where _ refers to the open site coverage. Reaction (6.4) is written for dissociative adsorption of phosphine which require four silicon surface sites. Reaction (6.5) represents desorption of $P_{n(g)}$ and, as mentioned above, we assume n=2 and 1 for high and low surface coverage of phosphorus. The incorporation of monatomic phosphorus, P_{ss} is described in equation (6.6). Under steady-state conditions the net rate of phosphorus coverage, θ_P, can be written as

$$\frac{d\theta_P}{dt} = k_1[PH_3]\theta^4 - k_2\theta_P^n - k_3\theta_P = 0, \tag{6.7}$$

where $[PH_3]$ is the gas-phase phosphine fraction or partial pressure and θ the fraction of vacant sites.

In the case of silicon epitaxial growth, it is recognized that the surface is passivated by P-P dimers and θ_P is close to 1 or saturates at a certain value. In consequence, equation (6.7) gives $\theta \propto [PH_3]^{-0.25}$. Since the growth rate of epitaxial silicon is proportional to θ^2 as shown in the preceding paper, R $\propto {\theta_P}^{-0.5}$, which contrasts the data presented in Fig. 6.13, where R was found to be associated with $[PH_3]^{-0.24}$ for phosphorus doped silicon epitaxy. A possible reason for the discrepancy stems from the different surface sites requirements for silane adsorption under different surface coverage. In a report on decomposition of silane on silicon (111)-(7×7) and silicon (100)-(2×1) surfaces below 500°C, it was surprisingly observed

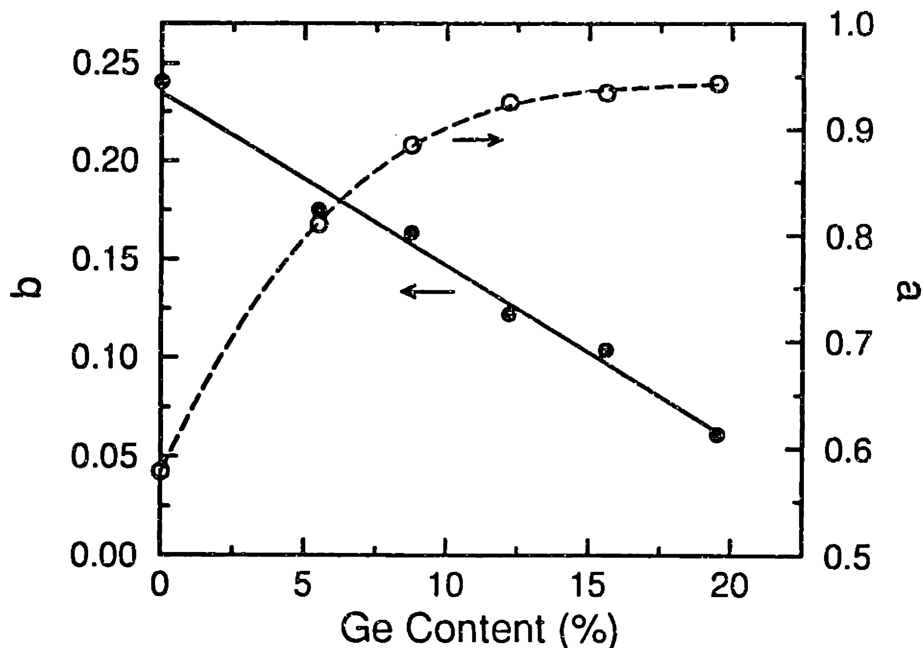

Figure 6.13: The exponent factors of a and b in Eq. (6.1) and (6.2) expressed as functions of germanium composition for phosphorus doping.

that such requirement was not stringent; either isolated or paired dangling bonds can be active adsorption sites depending on the surface conditions [122]. For silane adsorption on silicon (111) surface, because adjacent dangling bonds are separated as far as $\sim 7\AA$, a process of silane adsorption requiring only one dangling bond was proposed. Similar mechanism might occur on highly phosphorus covered surface when two neighboring vacant sites are not available. Consequently, the growth rate of silicon becomes proportional to θ or R $\propto [PH_3]^{-0.25}$, which is consistent with our observation. In UHVCVD, the growth rate of silicon layer is approximately proportional to $[PH_3]^{-0.33}$, indicating that both mechanisms of silane adsorption, requiring two or one surface site, might be operative.

As germanium composition is increased and surface coverage becomes low, θ_P is expected to be directly proportional to the phosphine flux or $[PH_3]$. As a result, equation (6.7) with n = 1 suggests that θ is phosphine independent and

the $Si_{1-x}Ge_x$ deposition rate is not affected by phosphine. This conclusion appears to agree with the observed germanium dependency of b shown in Fig. 6.13: as germanium content increases, the $Si_{1-x}Ge_x$ deposition rate is less phosphine dependent.

6.5 Conclusion

At conclusion, we have grown and characterized Si/p^+-$Si_{0.89}Ge_{0.13}/Si$, Si/n^+-$Si_{0.87}Ge_{0.13}/Si$ and p^+-$Si_{0.80}Ge_{0.20}/Si$ multilayer structures. Very hnigh boron (2×10^{20} cm^{-3}) and arsenic (5×10^{19} cm^{-3}) concentrations have been achieved using 1000 ppm B_2H_6 and AsH_3 without degrading film quality. The amount of boron atoms incorporated into $Si_{1-x}Ge_x$ layer is independent of germanium composition. No change in $Si_{1-x}Ge_x$ growth rate due to boron incorporation was measured. For n-type doping, we observed that the germanium content is not affected by the presence of phosphine. However, germanium plays an important role in phosphorus incorporation. The introduced germanium appear to enhance phosphorus incorporation. In addition, a dramatic improvement of phosphorus depth profil` was measured and the magnitude of growth rate inhibition due to n-type doping was found to decrease with increasing germanium content.

The observed phosphorus doping process greatly enhanced by germanium addition is thought to be a result of reduced surface passivation. We suggest that germanium might have two important effects on the doping process: the disruption of P-P dimerization and the enhancement of P desorption. Both effects lead to more vacant sites for the adsorption of other hydrides, which allow continuous growth with smoother morphology and less growth rate degradation, and eliminate the residual phosphorus doping after phosphine is terminated, which allows abrupt phosphorus dopant profile. However, though the suppressed formation of P-P dimers results in more monatomic phosphorus readily for incorporation into the

growing layer, the enhanced phosphorus desorption (in P_2 or P form) might reduce the population of phosphorus atoms on the surface and complicate the germanium dependency of phosphorus incorporation. Finally, a simple model based on the assumption that germanium reduces surface coverage of phosphorus is proposed and found consistent with the measured growth rate data.

Chapter 7

Critical Thickness and Thermal Stability of $Si_{1-x}Ge_x$

7.1 Introduction

It has been well demonstrated that, at low temperatures, $Si_{1-x}Ge_x$ strained layer can be grown to a thickness far exceeding the criterion of thermodynamic equilibrium theories without strain relaxation by using kinetically controlled growth techniques such as molecular beam epitaxy or chemical vapor deposition. These encouraging results that allow the growth of $Si_{1-x}Ge_x$ strained films with useful thicknesses for device application is due to the existence of kinetic barrier, i.e. Peierls stress opposing dislocation glide, to strain relaxation at low temperatures. However, since device fabrication routinely involves high temperature cycles, the metastable $Si_{1-x}Ge_x$ strained films may relax in subsequent processing and degrade device performance via misfit dislocation formation and/or via Ge diffusion. Since useful $Si_{1-x}Ge_x$ strained films are usually thicker than the equilibrium critical thickness [125], [126] and integrated circuit processing routinely involves high temperature steps, the metastable strained layer may relax during elevated temperature exposure and degrade device performance. In order that high-quality films can be maintained through device fabrication, it is of practi-

cal importance to understand the thermal stability of $Si_{1-x}Ge_x$ strained films, especially of $Si/Si_{1-x}Ge_x/Si$ heterostructures that have shown great promises for Si-based bipolar heterojunction transistor to operate at high speeds previously achieved with III-V semiconductors.

In this chapter, we explore the critical thickness and thermal stability of VLKPCVD $Si_{1-x}Ge_x$ strained layers.

7.2 Experiments

The samples used for this study of critical thickness and thermal stability of VLPCVD films were grown at 750°C and 620°C. The detailed growth procedures were described in Chapters 3 and 4, respectively. Structural characterization (XTEM) of some as-grown samples presented in this chapter has been shown in previous chapters. Thermal stability study was conducted for two different $Si_{1-x}Ge_x/Si$ heterostructures: uncapped and capped $Si_{1-x}Ge_x$ strained layers. The uncapped $Si_{1-x}Ge_x$ layers include 1240Å $Si_{0.92}Ge_{0.08}$ and 600Å $Si_{0.87}Ge_{0.13}$ grown at 750°C. While the $Si_{1-x}Ge_x$ strained layers capped with a $\sim$ 1400Å Si have Ge compositions of 0.09, 0.13, and 0.16 grown at 620°C, and their thickness is 710, 550, and 520Å, respectively.

The as-grown samples were annealed at temperatures ranging from 750 to 900°C (uncapped $Si_{1-x}Ge_x$) and from 800 to 1100°C (capped $Si_{1-x}Ge_x$) for 30 minutes in furnace under a flowing N_2 gas ambient. The misfit dislocations generated with strain relaxation were characterized using plan-view TEM. The TEM samples thinned in the [100] direction were prepared by mechanical polishing and ion milling, which allow the observation of dislocation structure in larger electron-transparent area of usually greater than $100 \times 100\ \mu m^2$. Strain relief in $Si/Si_{1-x}Ge_x/Si$ after thermal annealing was also measured by DCD. Ge diffusion profile after 30 min annealing at temperatures $\geq$ 900°C was probed by SIMS.

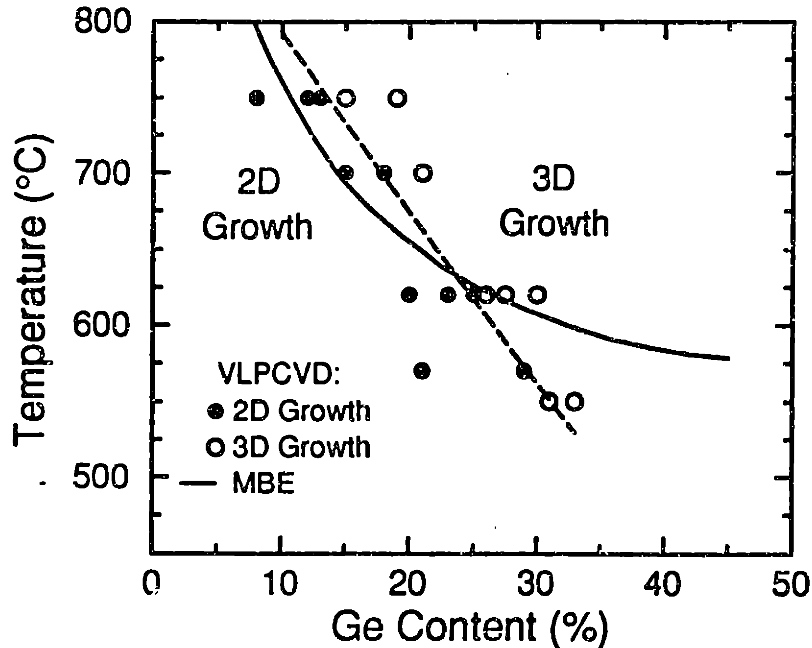

Figure 7.1: Comparisons of growth mode of $Si_{1-x}Ge_x$ heteroepitaxy in VLPCVD and MBE.

7.3 Critical Thickness of $Si_{1-x}Ge_x$

It has been shown that the growth mode, i.e., two-dimensional and three-dimensional growth, is very important to the surface morphology and crystalline quality of $Si_{1-x}Ge_x$ layers [13]. For $Si_{1-x}Ge_x$ layer to be useful, it is necessary to achieve two-dimensional growth, good morphology, and good crystalline quality. Investigation of $Si_{1-x}Ge_x$ growth mode in VLPCVD has been performed and some examples are shown in Chapters 3 and 4. In Fig. 7.1, we summarize the range of two/three-dimensional growth observed from VLPCVD $Si_{1-x}Ge_x$ layers as functions of temperature and Ge composition. Similar trends have been found between VLPCVD and MBE at deposition temperatures > 620°C. However, compared to MBE, three-dimensional growth becomes severe in VLPCVD at temperatures below 620°C. A possible explanation is the serious contamination of carbon and oxygen in VLPCVD at lower temperatures, as discussed in Chapter 4.

In addition to two-dimensional growth, another important parameter which determines the usefulness of the strained $Si_{1-x}Ge_x$ layers for a particular application is the critical thickness. The changes introduced in the band structure by strain may be large and are useful for several device applications. Misfit dislocation reduce the strain and degrade the properties of heteroepitaxial layers for several device applications [127]. Thus, it is important to determine the critical thickness of $Si_{1-x}Ge_x$ films, which might depend on deposition techniques.

The first study of critical thickness for heteroepitaxial growth was conducted by Frank and van der Merwe about 50 years ago [16, 17], who considered the stresses and the energies at the interface to be bicrystal grown as an epitaxial layer on a lattice-matched substrate. These workers discussed a one-dimensional model, which was extended to two dimensions by Jesser and Kuhlmann-Wilsdorf [124]. The work has been extended, compared with experiments and reviewed by van der Merwe and several other authors [128, 127]. These studies show that if the lattice mismatch is small and the thickness of the epilayer is not large, the atoms on the two sides of the interface are in perfect register and the mismatch is accommodated entirely by the elastic strain in the epitaxial layer; the growth of the epilayer is then said to be coherent, pseudomorphic or commensurate. If the thickness increases beyond a critical thickness, the epitaxial layer relaxes by the introduction of misfit dislocations. In the next few paragraphs, we will discuss the the equilibrium theories based on van der Merwe's model from the reviews by Jain et al. [128, 127], and based on Matthews' model from his original articles [20, 129].

According to van der Merwe, the energy E_h associated with the superimposed homogeneous strain and the energy E_d associated with the misfit dislocations are additive. The condition of equilibrium is obtained by minizing the total energy E_t

$$E_t = E_h + nE_d = minimum, \tag{7.1}$$

where n is the number of dislocation sets. When the layer is deposited on a (100) surface of a diamond structure semiconductor, there are two sets of misfit dislocations running perpendicular to each other and the value of n is 2 [130]. The elastic energy E_h for heteroepitaxial grown on (100) Si has been derived by Kasper et al. [79] as

$$E_h = 2\mu\frac{1+\nu}{1-\nu}\epsilon^2 h, \tag{7.2}$$

where μ is the shear modulus, ν is Poisson's ratio, ϵ is the elastic or misfit strain and h is the thickness of the heteroepitaxial layer. For a diamond structure, the energy E^{∞}_{ds} of a single dislocation is given by [79, 131]

$$E^{\infty}_{ds} = \frac{\mu b^2}{4\pi(1-\nu)}(1+ln\frac{h}{q'}) \tag{7.3}$$

where q' is the inner cut-off radius of the dislocation and is estimated as about $6\mathring{A}$ by Kasper [130]. The subscript ∞ on E indicates that the distance between neighboring dislocations is assumed to be so large that there is no interaction between them. The total energy due to 1/p dislocations per unit length is

$$E^{\infty}_{d} = E^{\infty}_{ds}/p. \tag{7.4}$$

Using Eq. 7.1 and n=2, the conditions for minimum total energy can be written as

$$\frac{\partial E_t}{\partial \epsilon} = \frac{\partial E_h}{\partial \epsilon} + 2\frac{\partial E_d}{\partial p}\frac{\partial p}{\partial \epsilon} = 0. \tag{7.5}$$

The critical thickness is determined by the additional conditions

$$p \to \infty, \frac{\partial E_{ds}}{\partial p} \to 0, \epsilon = f, \tag{7.6}$$

when $h=h_c$. Thus, the critical thickness for the growth on the (100) surface of a crystal of diamond structure is

$$h_c = \frac{b}{8\pi(1+\nu)f}[1+ln(\frac{2h_c}{q'})]. \tag{7.7}$$

Substituting numerical values suggested by Kasper et al. [131], we obtain

$$h_c(nm) = \frac{1.175 \times 10^{-2}}{f} ln[8.9 h_c(nm)] \quad (7.8)$$

for $Si_{1-x}Ge_x$-Si system.

Matthews and Blakeslee [20, 129] used a somewhat different approach, suggesting that the misfit dislocations are introduced through the glide of threading dislocations. Consider the forces acting on the dislocations lines including

1. The force exerted by the misfit strain.
2. The line tension in the misfit dislocation.
3. The tension in the surface step created by the moving dislocation.
4. The tension in the stacking fault (if the moving dislocation is nit perfect).
5. The interaction between the moving dislocation and other defects in its vicinity. Examples of defects that may be important are other threading dislocation, stacking faults, twins, grain boundaries, precipitates, and impurities.
6. The Peiers-Nabarro stress.

If the misfit is isotropic, then (a) is

$$F_\epsilon = \frac{2\mu(1+\nu)}{(1-\nu)} bh\epsilon cos\lambda, \quad (7.9)$$

where λ is the angle between the slip direction and that direction in the interface which is perpendicular to the line of intersection of the slip plane and the interface. (2) is approximately

$$F_l = \frac{\mu b^2}{4\pi(1-\nu)}(1-\nu cos^2\theta)(ln\frac{h}{b}+1), \quad (7.10)$$

where θ is the angle between the dislocation line and its Burgers vector. (3) is

$$F_s = \sigma b sin\theta, \quad (7.11)$$

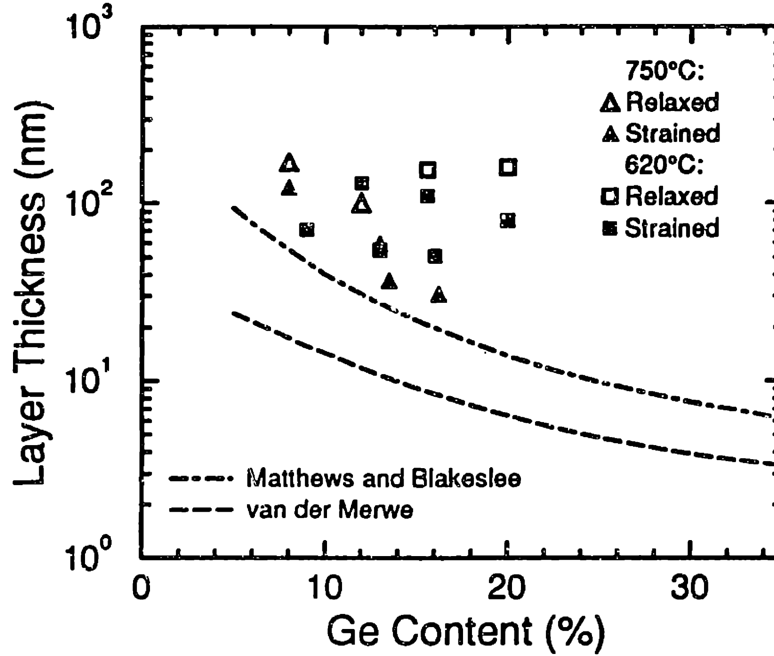

Figure 7.2: Critical thickness of VLPCVD $Si_{1-x}Ge_x$ grown at 750 and 620°C.

where σ is surface tension of the film. (4) is

$$F_\gamma = \gamma h / cos\phi, \tag{7.12}$$

γ is stacking fault energy, and ϕ is the angle between the film surface and the normal to the slip plane. (5) depends on many factors and is expected to vary with samples. The effect of (6) is small in metals but may be important in semiconductor. Matthews considered the most important forces, F_ϵ, F_l, F_s, and F_γ, and if F_ϵ is equated to the sum of other forces, then h_c is obtained as

$$h_c = \frac{\mu b^2/[4\pi(1-\nu)] \cdot (1-\nu cos^2\theta)[ln(h_c/b)+1] + \sigma b sin\theta}{2\mu(1+\nu)/(1-\nu) \cdot f b cos\lambda - (\gamma/cos\phi)}. \tag{7.13}$$

In Fig. 7.2, we present the Ge composition and $Si_{1-x}Ge_x$ thickness of some VLPCVD films grown at 750°C and 620°C, as well as their structure quality, i.e., strained or relaxed. The equilibrium critical thickness predicted by van der Merwe and Matthews (with ignored F_s and F_γ) are also indicated in Fig. 7.2 The critical

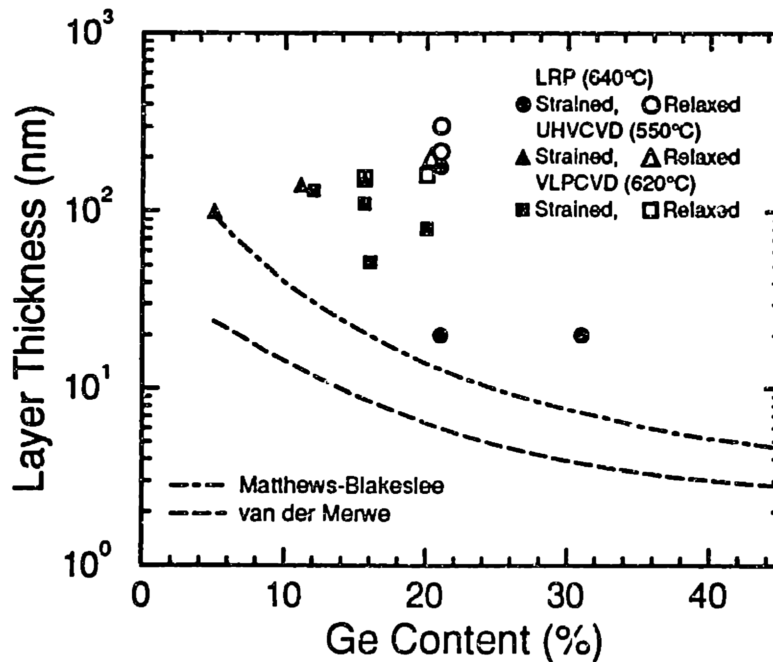

Figure 7.3: Comparison of critical thickness of VLPCVD, LRP, and UHVCVD $Si_{1-x}Ge_x$ strained layers.

thickness of 620°C VLPCVD films have been compared with other CVD techniques such as LRP and UHVCVD, as shown in Fig. 7.3. No significant difference was observed in critical thickness of $Si_{1-x}Ge_x$ strained layers produced by these different CVD reactors. Note that the critical thickness of $Si_{1-x}Ge_x$ strained layer grown at 640°C (LRP), 620°C (VLPCVD), and 550°C (UHVCVD) is well beyond the equilibrium criteria, indicating their metastable nature. Moreover, from Fig. 7.2, we see that the metastable critical thickness, i.e., the critical thickness beyond the equilibrium limit, is temperature dependent. The critical thickness of $Si_{1-x}Ge_x$ strained layer grown by VLPCVD at 750°C is less than at 620°C.

Among the conditions presented in Fig 7.2, the relaxation of $Si_{0.80}Ge_{0.20}$ when exceeding the equilibrium criteria has been more systematically studied. Figure 7.4 shows the Raman spectra of the VLPCVD $Si_{0.80}Ge_{0.20}$ samples with thicknesses of 0.08μm, 0.16μm, 0.40μm, and 0.80μm. Two strong peaks appear at

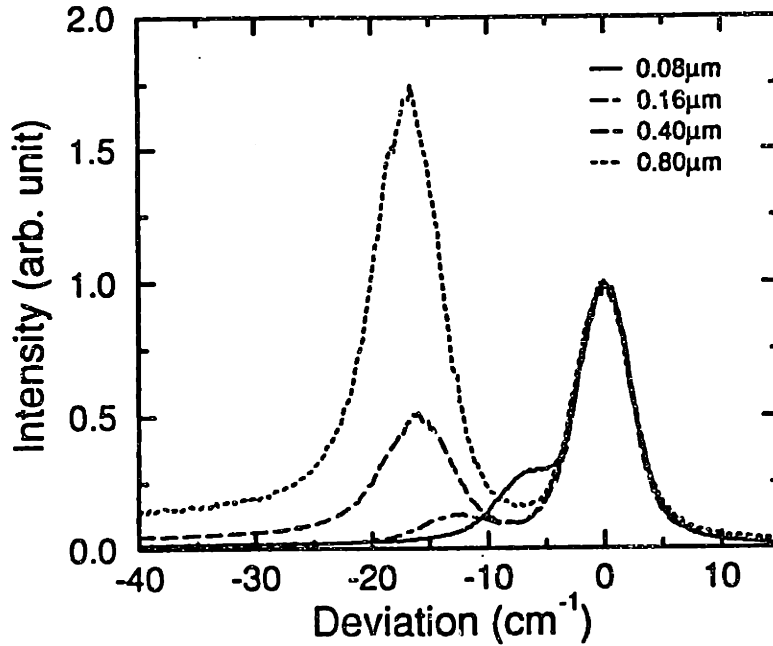

Figure 7.4: Raman spectra of $Si_{0.80}Ge_{0.20}$ on Si as a function of layer thickness.

521 and about 505 cm^{-1}; these are due to the Si phonon modes of the substrate and of the $Si_{1-x}Ge_x$ layers. The strain is related to the Si phonon mode from $Si_{1-x}Ge_x$. Dr. Nakano have measured the change of the peak position and found that the 0.4μm and 0.80μm-thick samples have almost the same positions at 505cm^{-1}. Since the value is the same as that in the $Si_{1-x}Ge_x$ bulk crystal observed by Byra [143], it was concluded that these two layers are totally relaxed. On the other hand, no dislocation was observed in the 0.08μm-thick $Si_{0.80}Ge_{0.20}$ by TEM (not shown). Because the peak of Si phonon from 0.16μm $Si_{0.80}Ge_{0.20}$ is different from that of 0.08μm sample, it is expected to be partially relaxed, and the degree of relaxation can be estimated using

$$\delta\omega = \frac{C_1}{2\omega_0}\epsilon_\perp + \frac{C_2}{\omega_0}\epsilon_\| = C_3(S_{11} + S_{12})\tau, \tag{7.14}$$

where C_1, C_2, and C_3 are phenomenological material parameters, S_{11} and S_{12} are the alloy compliances, and τ the built-in interfacial biaxial stress. Using the data of

the Raman peak shift for a stress for pure Si, $0.4cm^{-1}/kbar$ [144], a stress of about 24 kbar is generated in the $0.08\mu m$-thick layer. Since the peak shift is proportional to the stress in Eq. 7.14, the magnitude of the stress relaxation of the $0.26\mu m$-thick layer is determined to be 36%. Thus, the critical thickness of VLPCVD $Si_{0.80}Ge_{0.20}$ was determined to be between 0.08 and 0.16 μm.

Figure 7.2 also shows the effect of deposition temperature on critical thickness and the observed metastable critical thickness at lower deposition temperatures can be realized from the Peierls-Nabarro stress that is important in semiconductors. Fox and Jesser have recently presented a critical-thickness model in an attempt to provide a physical basis for the discrepancy between the observed and calculated critical thickness in diamond structure based on force balance and a Volterra description of the dislocation line tension with frictional forces including Peierls barriers and dislocation atmospheres [145]. The effect of the frictional forces, which is exponential temperature dependence, is to shift the critical thickness to a larger value and to produce a residual elastic strain which persists for larger thicknesses. The frictional barriers are low in face-centered-cubic metals and produce minor changes from the previous equilibrium theories, but it may be high and produce a substantial increase in the predicted critical thickness. Similar to that presented by Matthews [126], the governing equation for the calculation of critical thickness is a force balance between the driving force for generating a misfit dislocation (F_ϵ) and the sum of the frictional force (F_f) and the line tension (F_l), both of which resist the bending over of a threading dislocation to form a misfit dislocation. The governing force balance at the critical thickness is

$$F_\epsilon - F_f - F_l = 0. \tag{7.15}$$

In the previous equilibrium calculation by Matthews, the friction force is ignored. Fox et al. derived the frictional force as

$$F_f = Ahexp(\frac{U_i}{kT}) + vBhexp(\frac{Q_i}{kT}) + F_0, \tag{7.16}$$

where v is the dislocation velocity, U_i and Q_i are "activation energies" for the motion of particular dislocation i, F_0 is the resistive forces due to obstacles such as dislocation atmosphere or other dislocations. Although some parameters remained uncertain in Eq. 7.16, it is obvious that, due to the existence of frictional force, the critical thickness is changed. At low temperatures, the frictional force is large and leads to a increased critical thickness. However, at higher temperatures, the frictional force is reduced and the critical thickness becomes smaller. Thus it explains why we observed greater critical thickness at 620°C. It is important to point out that the frictional force or the difference of driving force and dislocation line tension can be looked as a "effective force" that remains in the strained layer. This effective force has been interpreted as a driving force for strain relaxation by Dodson [59] and Houghton et al. [55] When the thickness exceeds the equilibrium criteria (strained energy is too high) or when the metastable $Si_{1-x}Ge_x$ strained layer is exposed to thermal treatment (sufficient thermal energy is provided for strain relaxation), this force will encourage the generation and movement of misfit dislocations.

7.4 Thermal Stability of $Si_{1-x}Ge_x$

7.4.1 Misfit Dislocation

$Si_{1-x}Ge_x$/Si Structures

Thermal stability of uncapped 1240Å $Si_{0.92}Ge_{0.08}$ and 600Å $Si_{0.87}Ge_{0.13}$ have been investigated using plan-view TEM. Figures 7.5 and 7.6 (a) - (f) show the TEM micrographs obtained from the $Si_{1-x}Ge_x$ as-grown samples and the samples after receiving 30 min annealing at 750 - 950°C. It is clear that the as-grown samples have very good quality; with dislocation density under the detection limit of TEM. However, post-annealed films were found dislocated, suggesting strain relief occurred during the 30 min thermal exposure. These misfit dislocations were iden-

(a)

(b)

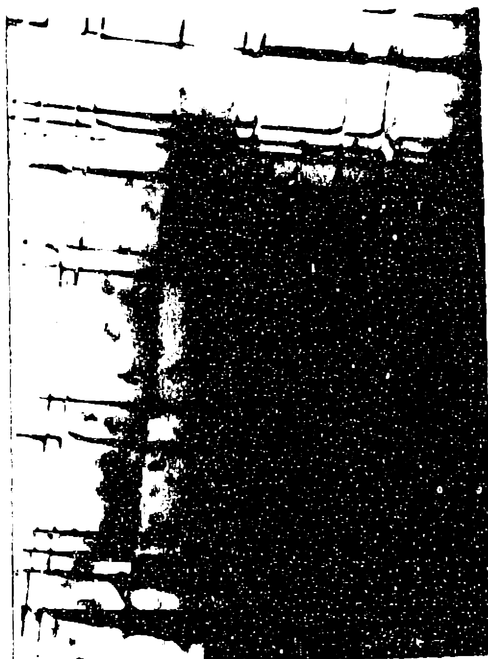

(c)

(d)

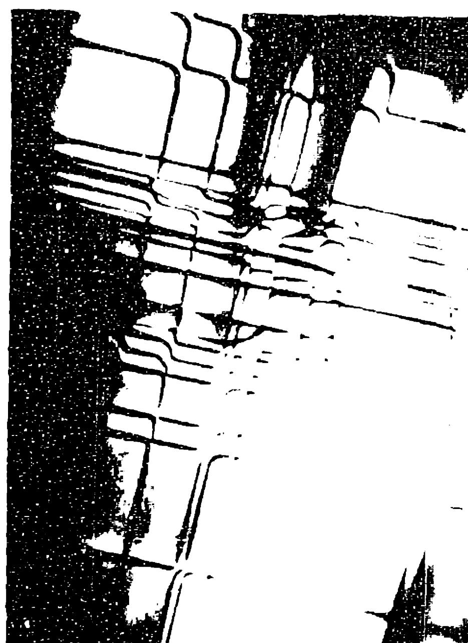

(e) (f)

Figure 7.5: Plan-view TEM micrographs of 1240 Å $Si_{0.92}Ge_{0.08}$ (as-grown sample shown in (a)) annealed for 30 min at (b) 750°C, (c) 800°C, (d) 850°C, and (e) 900°C. (f) 950°C. (12,000X)

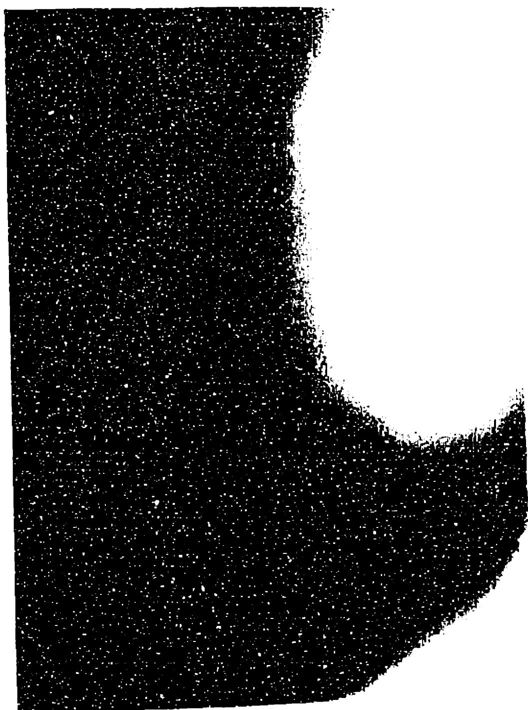

(a)

(b)

(c)

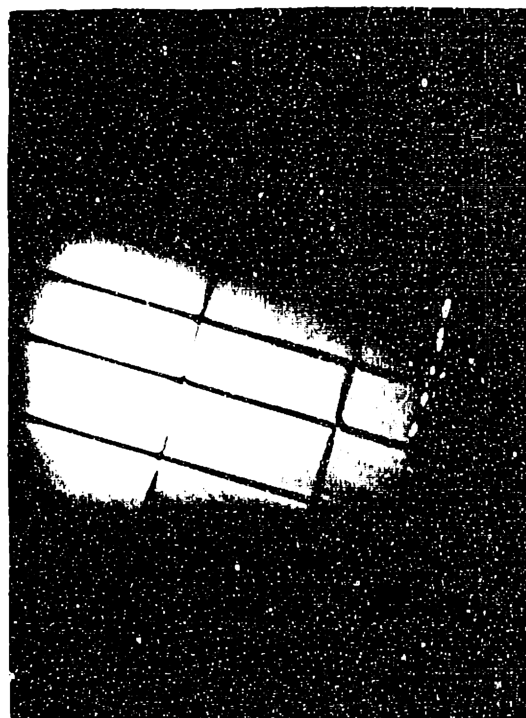

(d)

(e)

(f)

Figure 7.6: Plan-view TEM micrographs of 1240 Å $Si_{0.87}Ge_{0.13}$ (as-grown sample shown in (a)) annealed for 30 min at (b) 750°C, (c) 800°C, (d) 850°C, and (e) 900°C. (f) 950°C. (14,000X)

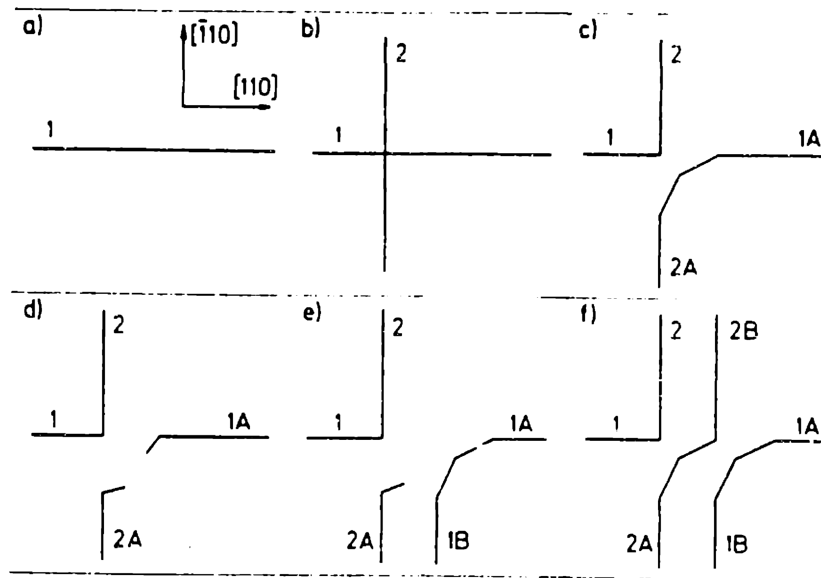

Figure 7.7: Schematic of the Hagen-strunk dislocation multiplication mechanism [141].

tified to be typical <110>-type, as widely reported in $Si_{1-x}Ge_x$-Si systems. It is interesting to that, as indicated by arrows in some annealed samples, the Hagen-Strunk dislocation multiplication mechanism were in operation. Figure 7.7 shows the schematic diagram of the Hagen-Strunk mechanism [141].

Hagen and Strunk consider two misfit dislocations with the same Burgers vectors, i.e., <110>, crossing at right angle in the (100) plane (Fig 7.7 (b)). At the intersection point, annihilation reaction yields the formation of two angular dislocations in an asymmetrical configuration ((Fig 7.7 (c)). The dislocation line 1-2 shows a sharp 90° edge (tip may be rounded due to local climb). The other dislocation line 1A-2A reveals two transition segments which are inclined to the growth plane. The transition segments frequently reach the layer surface to form two individual dislocation segments (1A and 2A in Fig 7.7 (d)), especially in thin layers ($\leq 0.5\mu m$). The dislocations 1A and 2A may elongate by glide under the acting misfit stress; however, their glide possibilities are restricted by the presence

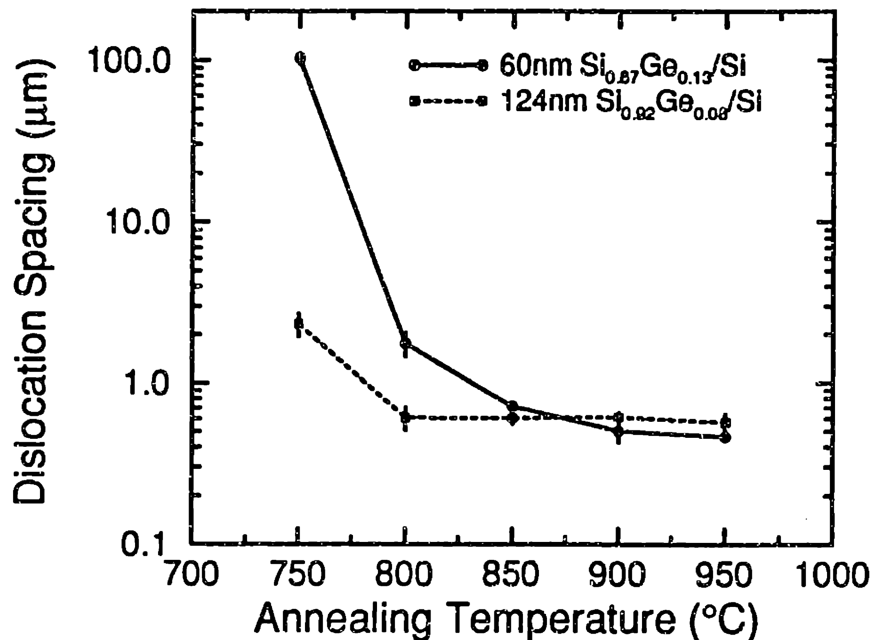

Figure 7.8: Measured spacing between misfit dislocations in relaxed 1240Å $Si_{0.92}Ge_{0.08}$ and 600Å $Si_{0.87}Ge_{0.13}$ annealed at 750 – 950°C for 30 min.

of the adjacent dislocations. Hagen and Strunk suggested that the most probable elongation mechanism is depicted in Fig. 7.7 (e) and (f). The segment attached to dislocation 1A cross-slips and glides on its second {111} glide plane. The tip of the newly formed angular dislocation 1A-1B may again exhibit two inclined transition segments due to the image forces (Fig. 7.7 (e). The segment of dislocation 1-2 and 1A-1B by double cross-slip leading to the formation of a new misfit dislocation parallel to dislocation 2 (Fig. 7.7 (f)). This mechanism may be repeated, if the new transition segments of dislocation 1A-1B reach the surface [141].

The TEM micrographys shown in Fig 7.5 and 7.6 allow the determination of dislocation density in the relaxed $Si_{1-x}Ge_x$ layers. Figure 7.8 summaries the measured dislocation spacing between misfit dislocations. Note that the data represented for 750°C annealed $Si_{0.87}Ge_{0.13}$ was obtained from chemical etching because only one misfit dislocation was detected in an area of about 90 × 90 μm

by TEM and defect etching was used to reveal lower dislocation density in a larger area. From Fig. 7.8, we observe that both 1240Å $Si_{0.92}Ge_{0.08}$ and 600Å $Si_{0.87}Ge_{0.13}$ relaxed very rapidly upon 30 min annealing at temperatures lower than 800°C. Moreover, though these samples were deposited at 750°C, a 30 min (which is much longer compared to the deposition times of 2 and 4 minutes) annealing at 750°C also led to significant strain relief, indicating that the deposition time at 750°C may play an important role in the critical thickness. As the growth temperature is increased, the limit of critical thickness becomes tight.

Another important feature we see from Fig. 7.8 is the almost constant dislocation spacing or saturated dislocation density at the annealing temperatures above 850°C. For a $Si_{1-x}Ge_x$ layer grown on (100) Si substrates, the in-parallel strain (the strain in the direction in parallel to the $Si_{1-x}Ge_x$/Si interface) is

$$\epsilon_{\parallel} = f - \frac{b}{2p}, \tag{7.17}$$

where f is lattice mismatch between $Si_{1-x}Ge_x$ and Si, $0.042x$, p is the dislocation spacing and b the Burgers vector of <100> misfit dislocation, i.e., 4Å. Thus, the relieved strain due to the generation of misfit dislocation can be estimated by

$$\triangle\, \epsilon_{\parallel} = \triangle \frac{b}{2p}. \tag{7.18}$$

From Fig. 7.8, we calculated the relieved strain at the saturated dislocation density to be $\sim 4\times10^{-4}$ for both $Si_{0.92}Ge_{0.08}$ and $Si_{0.87}Ge_{0.13}$, which is less than the original strain ($\epsilon_{\parallel} = f = 0.042x$) of 3.66×10^{-3} for x=0.08 and 5.46×10^{-2} for x=0.13. Apparently, the annealed $Si_{1-x}Ge_x$ films are not totally relaxed though the dislocation density becomes saturated. Thus, we speculate that there is an equilibrium between the misfit stress, which encourages the movement of misfit dislocation, and the repulsive stress among dislocations, which inhibits the movement of dislocation. As a recult, the dislocation density did not further increase even by elevating temperature when the misfit stress and repulsive stress are in balance.

$Si/Si_{1-x}Ge_x/Si$ Structures

The great potential of Si-based heterojunction bipolar transistors has been demonstrated by recent work using $Si_{1-x}Ge_x$ as a base, and a very high cutoff frequency of 75 GHz has been achieved [132]. In recent years, the thermal stability of $Si_{1-x}Ge_x$ with Si capping layers has been intensively studied [55, 53],[133]-[136],[137],[138]-[140]. The relaxation processes dominated by misfit dislocations are structure dependent, and possible mechanisms including double-kink (paired dislocation), which is frequently observed, and single-kink (single dislocation) models have been proposed to characterize strain relaxation [134, 137, 53]. Recently, the thermal stability of $Si_{1-x}Ge_x$ ($\leq$1000Å with various Ge compositional profiles) capped with a relatively thin Si layer of $\leq$ 500Å deposited by ultra-high vacuum chemical vapor deposition has been reported [140]. In all cases, relaxation due to 30 min furnace anneal at 950°C accomplished via single-kink dislocation nucleation and glide was mentioned. In this section, we report the thermal stability of very low pressure chemical vapor deposition (VLPCVD) [78]. $Si/Si_{1-x}Ge_x/Si$ heterostructures throughout the temperature range of 800°C – 1100°C. We concentrated on very thin $Si_{1-x}Ge_x$ ($\leq$700Å) with box-like Ge profile capped with a $\sim$ 1400Å Si layer, which is suitable for heterojunction bipolar transistors, and found that the single-kink mechanism also became important in these structures during annealing. The quantitatively measured strain and the corresponding misfit dislocation mechanisms as a function of temperature are presented.

In this work, we have studied the thermal stability of three strained $Si_{1-x}Ge_x$ sandwiched structures indicated by cross symbol in Fig. 7.9. Strain relief upon annealing in $\sim$1400ÅSi/520–700Å$Si_{1-x}Ge_x/Si$ structures with Ge compositions of 0.09, 0.13, and 0.16, have been measured by DCD and shown in Fig. 7.9. To examine the relaxation process, in all cases, samples receiving 30 min annealing at 800, 900, 1000, and 1100°C have been characterized by plan-vew TEM.

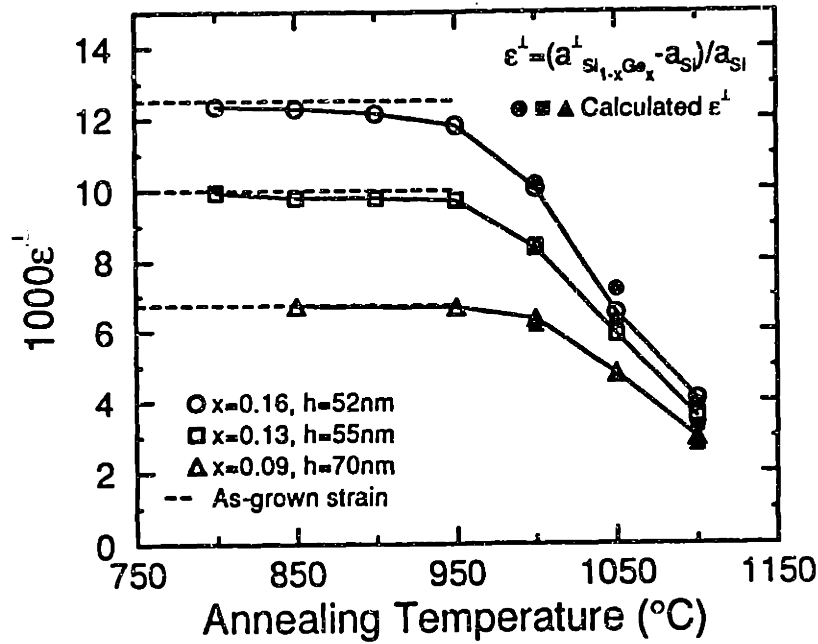

Figure 7.9: Perpendicular mismatch of $Si_{1-x}Ge_x$ in Si/$Si_{1-x}Ge_x$/Si heterostructures (x=0.09, 0.13, and 0.16) annealed at 800 – 1100°C for 30 min in a N_2 flow.

In Fig. 7.9 we show results of DCD characterization of $Si_{1-x}Ge_x$ films with Ge compositions of 0.09, 0.13, and 0.16, and the thicknesses of $Si_{1-x}Ge_x$, which is buried by a $\sim$ 1400Å-thick Si capping layer, are 710, 550, and 520Å, respectively. The perpendicular lattice parameters of $Si_{1-x}Ge_x$, $a^{\perp}_{SiGe}$, was obtained from (400) rocking curves and the strain $\epsilon^{\perp}_{SiGe}$ is given by

$$\epsilon^{\perp}_{SiGe} = \frac{a^{\perp}_{SiGe} - a_{Si}}{a_{Si}}, \tag{7.19}$$

where a_{Si} is the lattice parameter of Si. Upon relaxation $Si_{1-x}Ge_x$ film loses its coherency with Si substrate and $a^{\perp}_{SiGe}$ (i.e. $\epsilon^{\perp}_{SiGe}$) decreases as strain relaxation proceeds. From Fig. 7.9 we observe that relaxation takes place relatively gradually at temperatures < 950°C, but rapidly at T > 950°C, showing a transition in the relaxation process.

To examine the process, $Si_{0.91}Ge_{0.09}$, $Si_{0.87}Ge_{0.13}$, and $Si_{0.84}Ge_{0.16}$ films were characterized by plan-view TEM after receiving 30 min annealing at various tem-

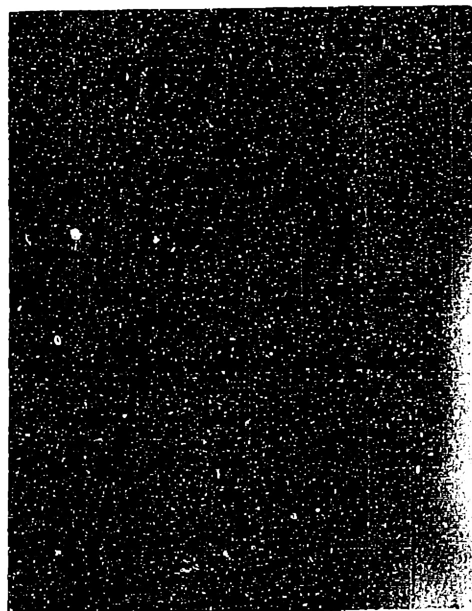

(a)

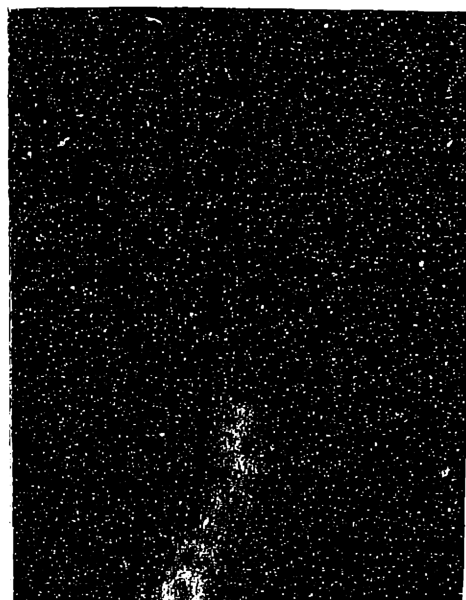

(b)

(c)

Figure 7.10: Plan-view TEM micrographs of Si/700 Å $Si_{0.91}Ge_{0.09}$/Si annealed for 30 min at (a) 900°C, (b) 1000°C, and (c) 1100°C. (11,000X)

(a)

(b)

(c)

(d)

Figure 7.11: Plan-view TEM micrographs of Si/550 Å $Si_{0.87}Ge_{0.13}$/Si annealed for 30 min at (a) 800°C, (b) 900°C, and (c) 1000°C, and (d) 1100°C. (11,000X)

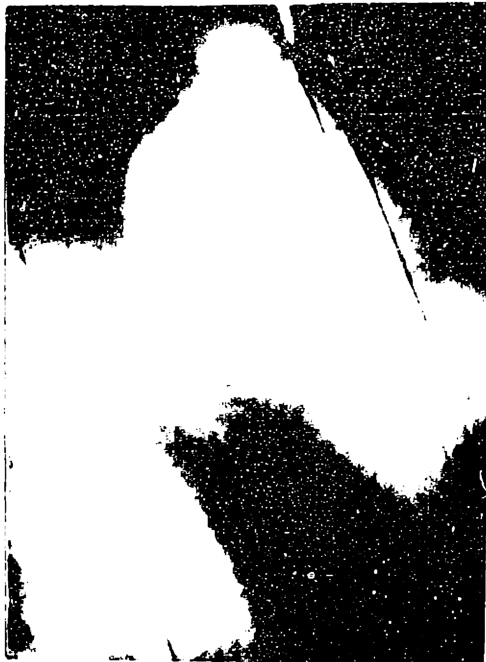

(a)

(b)

(c)

(d)

Figure 7.12: Plan-view TEM micrographs of Si/550 Å $Si_{0.84}Ge_{0.16}$/Si annealed for 30 min at (a) 800°C, (b) 900°C, (c) 1000°C, and (d) 1100°C. (13,000X)

peratures, as shown in Fig. 7.10, Fig. 7.11, and Fig. 7.12. It is apparent that in $Si/Si_{0.87}Ge_{0.13}/Si$ (Fig. 7.11) structure misfit dislocations retain a single-kink or two-segment configuration with dislocations created only at the interface between $Si_{0.87}Ge_{0.13}$ and the underlying Si, and no misfit dislocation resulted at the Si cap/$Si_{0.87}Ge_{0.13}$ interface. To realize the dislocation mechanism, following Houghton [137], who further modified Matthews' idea, we compare the unbalanced force, i.e. effective stress τ_{eff}, driving 60° type misfit dislocation for single-kink (single dislocation, τ^S_{eff}) and double-kink (paired dislocation, τ^P_{eff}) mechanisms in strained $Si_{1-x}Ge_x$ buried-layer using

$$\tau^S_{eff} = 2\mu cos\psi\frac{1+\nu}{1-\nu}[\frac{h}{h+H}fcos\lambda - \frac{b(1-\nu cos^2\theta)}{8\pi(1+\nu)(h+H)}ln\frac{4(h+H)}{b}] \qquad (7.20)$$

and

$$\tau^P_{eff} = 2\mu cos\psi\frac{1+\nu}{1-\nu}[fcos\lambda - \frac{b(1-\nu cos^2\theta)}{8\pi(1+\nu)h}\times(ln\frac{4(h+H)}{b} + ln\frac{4H}{b} + 2ln\frac{h}{h+H})], \qquad (7.21)$$

where, for 60° mixed a/2< 110 > dislocations, ψ=35° is the angle between the strained interface normal and the slip plane, θ=60° is the angle between the Burgers vector (b=4$\mathring{A}$) and the dislocation line, λ=60° is the angle between the Burgers vector and the direction in the interface, normal to the dislocation line, ν=0.28 is the Poisson's ratio, f=0.042x is the lattice mismatch between Si and $Si_{1-x}Ge_x$, h is the $Si_{1-x}Ge_x$ layer thickness, H the thickness of Si capping layer, and μ the shear modulus of $Si_{1-x}Ge_x$. The calculated effective stresses (τ^S_{eff} and τ^P_{eff}) for strain relief by single and paired dislocation in the $Si/Si_{1-x}Ge_x/Si$ heterostructures have been calculated. The greater driving force for the movement of single-kink dislocation in $Si_{0.87}Ge_{0.13}/Si$ was confirmed by plan-view TEM results and only single dislocations were observed. Moreover, distinct dislocation structures were seen after the samples exposed to different thermal cycles. For example, discrete dislocation segments are observed after 800°C anneal. At 900°C, the sample exhibits

more relaxation and the misfit dislocation lines extend up to at least 100μm running in one <110> direction, while at 1000°C the interactions of two orthogonal misfit dislocations with the same Burgers vector are evident. As temperature was elevated up to 1100°C, complicated misfit dislocation arrangement formed. The presence of angular dislocations was thought to be a result of dislocation climb activated by sufficient thermal energy, and the nodes generated by dislocation interactions was observed.

Similar to the case of 1100°C annealed $Si_{1-x}Ge_x$ with $x = 0.13$, $Si_{0.84}Ge_{0.16}$ reveals dislocation configurations consisting of . angular dislocations. However, both single- and double-kink dislocations were observed in the $Si/Si_{0.84}Ge_{0.16}/Si$ heterostructures, even though $\tau_{eff}^P > \tau_{eff}^S$. An explanation of the inconsistence may require the consideration of τ_{eff} in the dynamic process. The effective stress in Eq. 7.20 and 7.21 is determined by the inbalance between the resolved shear stress acting on the misfit dislocation slip system and the line tension in the dislocation, and the former is dominated by the misfit strain between $Si_{1-x}Ge_x$ and silicon, f. Upon relaxation, misfit dislocations are introduced and the lattice parameter of $Si_{1-x}Ge_x$ is changed, thereby the actual misfit between relaxed $Si_{1-x}Ge_x$ and underlying silicon is reduced to $\sim$ f - b/2p, where p is the dislocation spacing. In consequence, the effective stress is decreased by the magnitude of

$$\triangle\, \tau_{eff}^S = 2\mu cos\psi cos\lambda \frac{1+\nu}{1-\nu}\frac{hb}{2p(h+H)} \tag{7.22}$$

and

$$\triangle\, \tau_{eff}^P = 2\mu cos\psi cos\lambda \frac{1+\nu}{1-\nu}\frac{b}{2p} \tag{7.23}$$

for single-kink and double-kink dislocation, respectively. It is evident that the reduction of τ_{eff}^P owing to dislocation generation is more severe compared to τ_{eff}^S by a factor of (H+h)/h because of the diluting effect of silicon capping layer on τ_{eff}^S. Inspecting Eq. 7.22 and 7.23, in this case, strain relief of about 0.0005 or dislocation density of about 6×10^{8} cm^{-2} is required to make $\tau_{eff}^S > \tau_{eff}^P$ to

generate single-kink dislocation. Such magnitude appears to be slightly higher than the TEM data obtained from 800 and 900°C annealed films exhibited in Fig 7.12 (a) and (b); however, it is close enough and it would not be unreasonable to say that the appearance of both paired and single dislocation was due to the operation of double-kink mechanism and single-kink mechanism, and The latter became important as τ^S_{eff} became greater than τ^D_{eff} during strain relaxation.

From TEM micrographs we are able to count the dislocation density and the amount of relaxed perpendicular strain led by the injection of misfit dislocation can be estimated by

$$\triangle \epsilon^{\perp}_{SiGe} \sim \frac{1+\nu}{1-\nu} \triangle \frac{b}{2p} \tag{7.24}$$

where p is the dislocation spacing, and in this study we find that $b/2p$ is on the order of 10^{-4} or less, which is consistent with the observed sluggish relaxation by DCD at T < 950°C. However, since strain relief is much greater than 10^{-4} at T > 950°C, the formation of dislocation is not sufficient to explain the significant relaxation at higher temperatures. Moreover, excess relaxation

$$a^{\perp}_{SiGe} < a^{total\ relax}_{SiGe} = x a_{Ge} + (1-x) a_{Si} \tag{7.25}$$

was measured at 1000°C - 1100°C. This suggests that a new mechanism differing from dislocation generation is in operation as annealing temperature increases. This is supported by the fact that no misfit dislocation was found by plan-view TEM in $Si_{0.81}Ge_{0.09}$ after 800 - 1100°C 30 min anneal, though serious strain relaxation was measured by DCD at elevated temperatures (> 950°C). A likely mechanism to account for this phenomenon is the interdiffusion of silicon and germanium, which has been reported to be a competing process compared to dislocation generation at high temperatures for relieving the misfit stress at the interface and is particularly significant for thin layers [47].

7.4.2 Ge Diffusion

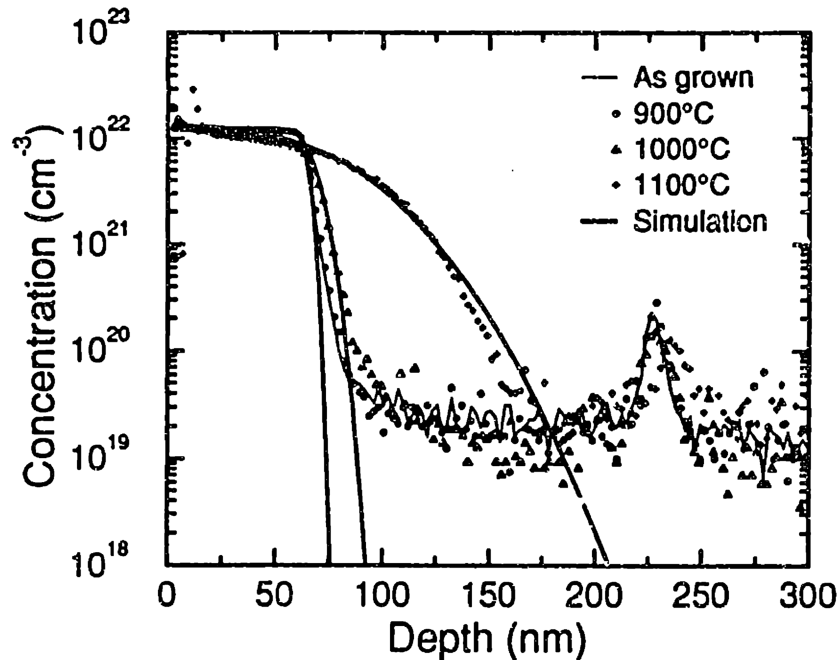

Figure 7.13: Ge diffusion profiles in a $Si_{0.80}Ge_{0.20}/Si$ structure after 30 min annealing at 900 - 1100°C.

To understand the effect of Ge diffusion on the relaxation of $Si_{1-x}Ge_x$ strained layers, we have measured the Ge diffusivity at temperatures > 900°C. Figure 7.13 shows the Ge diffusion profiles in a $Si_{0.80}Ge_{0.20}/Si$ heterostructures after 30 min anneal at 800 - 1100°C. Data of Ge diffusivities were extracted from the simulation of Ge profiles using Error functions, which will be shown later. In addition, to examine the effect of Ge content (x=0.20 vs. x=0.16) on diffusion and to quantitatively relate the Ge diffusion profile to the measured DCD data shown in Fig. 7.9, SIMS was also performed to determine the Ge diffusivities in the annealed $Si/Si_{0.84}Ge_{0.16}/Si$ heterostructures whose TEM results are presented in Fig. 7.12. Figure 7.14 exhibits the diffusion profile of Ge as a function of annealing temperature. Similar to that demonstrated in Fig. 7.14, Ge diffusion becomes significant at temperatures above 950°C and is consistent with the observed rapid relaxation of $Si/Si_{1-x}Ge_x/Si$ heterostructures at temperatures > 950°C. From Fig. 7.13 and

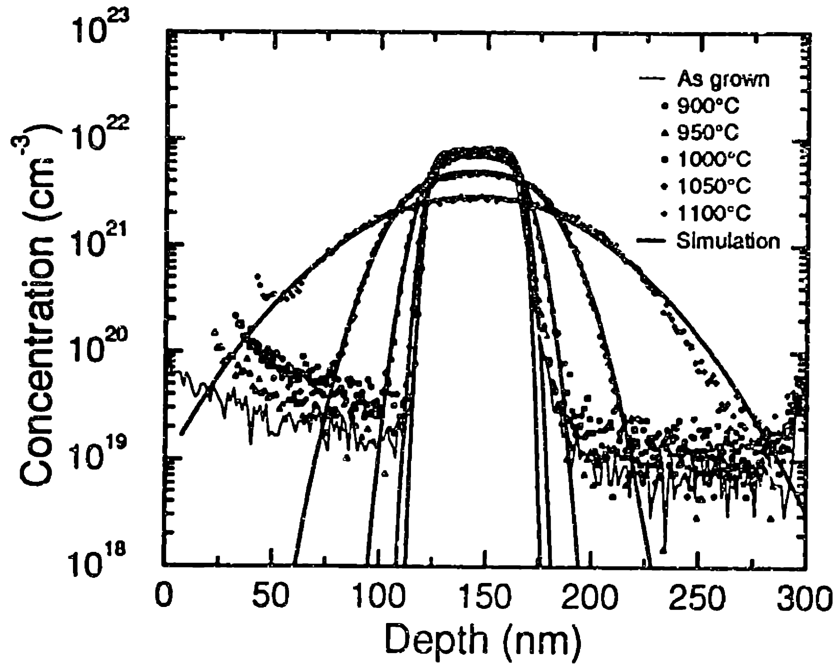

Figure 7.14: Ge diffusion profiles in a $Si/Si_{0.84}Ge_{0.16}/Si$ structures after 30 min annealing at 900 - 1100°C.

7.14, we extract the Ge diffusivities and plot them in Fig. 7.15. Shown also in Fig. 7.15 are the diffusion coefficients of Ge measured by other groups. Excellent agreements were observed at higher temperatures (T > 1000°C) for Ge compositions of 0.15 - 0.20, but slight discrepancies exist at lower temperatures, which might be due to the greater errors in measurement or due to the strain effect on Ge diffusion.

Since dislocation-induced relaxation is far less than the measured DCD data at high temperatures, the strain is mainly determined by Si-Ge interdiffusion and the perpendicular strain $\epsilon^{\perp}$ might be estimated by

$$\epsilon^{\perp} = \frac{1+\nu}{1-\nu}\overline{f} = \frac{1+\nu}{1-\nu} \times \frac{0.042}{h_{eff}} \int_{-h_{eff}/2}^{h_{eff}/2} x(z)dz \sim \frac{1+\nu}{1-\nu} \times \frac{0.042 x_0 h}{h_{eff}} \qquad (7.26)$$

where $\overline{f}$ is the average mismatch, $x(z)$ is the Ge profile modulated by diffusion, and h_{eff} the effective layer thickness of $Si_{1-x}Ge_x$ with Ge confined in the region

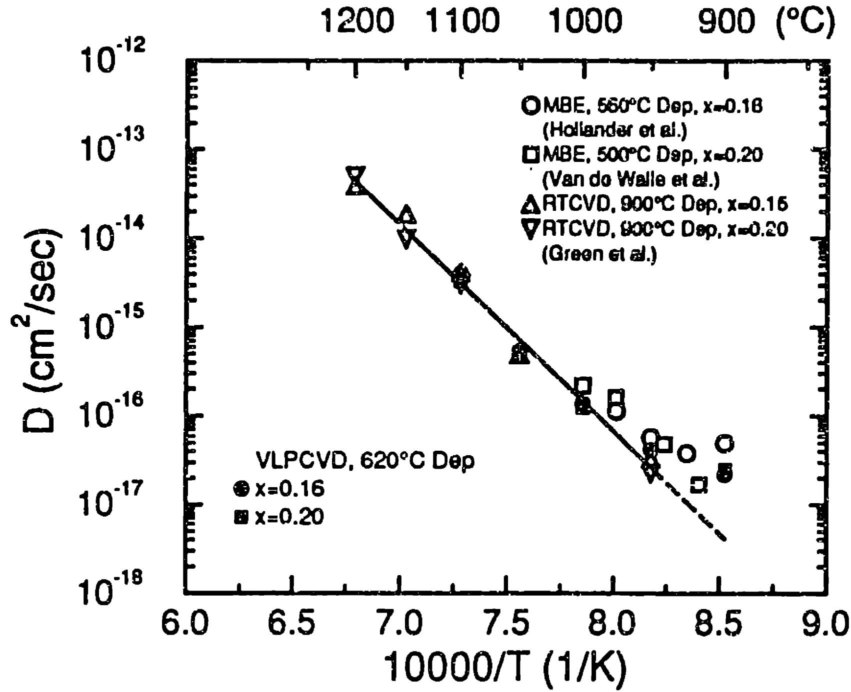

Figure 7.15: The measured Ge diffusivity as a function of temperature.

$$\frac{-h_{eff}}{2} \leq z \leq \frac{h_{eff}}{2}. \tag{7.27}$$

Prior to annealing, h_{eff} is the original $Si_{1-x}Ge_x$ thickness (h) and x_0 the original Ge composition. $\overline{f}$ can be written as $0.042x_0h/h_{eff}$ if Ge atoms at $z > h_{eff}/2$ and $z < -h_{eff}/2$ are negligible. To estimate h_{eff} we consider the finite-thickness solution to the Fick's second law for Ge diffusion into Si,

$$x(z) = \frac{x_0}{2} \times [erf(\frac{z+h/2}{2\sqrt{Dt}}) - erf(\frac{z-h/2}{2\sqrt{Dt}})], \tag{7.28}$$

using the measured Si-Ge interdiffusion coefficients for $x = 0.15 - 0.20$, as shown in Fig. 7.15. Since $\sqrt{Dt}$ at 950°C equals 23Å, diffusion phenomenon can be considered negligible at temperatures below 950°C. Assuming that the effective diffusion length of Ge into Si is about $\sqrt{2Dt} \sim 2\sqrt{Dt}$, which consists of $\sim$ 95% Ge atoms within h_{eff}, we calculate $\epsilon_\perp$ using Eq. 7.26 and find the calculated and measured values are in good agreement as indicated in Fig. 7.9. Clearly, the dominant

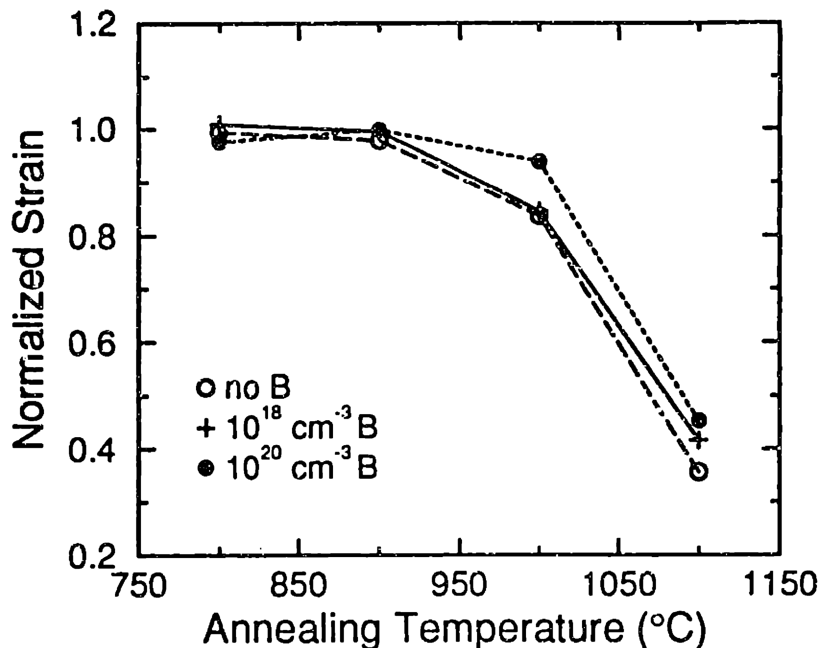

Figure 7.16: Measured strain in Si/B-doped $Si_{0.88}Ge_{0.12}$/Si heterostructures for various B dopant concentration: 0, 10^{18}, and 10^{20} cm^{-3}.

mechanism at T > 950°C is with Si-Ge interdiffusion and the residual strain after high-temperature annealing is determined by the diffused Ge profile.

7.4.3 Dopant Effects

The effects of B dopant on the thermal stability of $Si_{1-x}Ge_x$ strained layers have been investigated and are shown in Fig. 7.16. It is evident that the residual strain in highly B doped $Si_{1-x}Ge_x$ layer is higher than that in undoped $Si_{1-x}Ge_x$. This observation is also confirmed by TEM results from other samples. Figure 7.17 shows that fewer dislocations appeared in the B doped layers, suggesting more stable nature. A possible reason for the B doped $Si_{1-x}Ge_x$ to be more stable is that the stress is compensated by B doping, since B atoms are much smaller than Si and Ge.

(a)

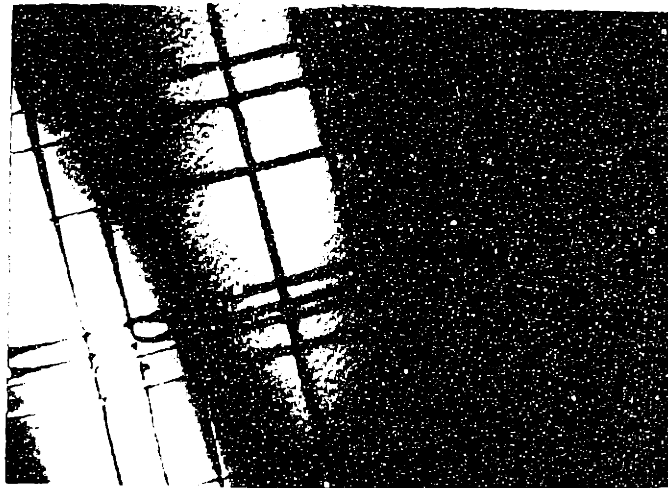

(b)

Figure 7.17: TEM micrographs of (a) undoped $Si_{0.80}Ge_{0.20}$, and (b) B doped (2×10^{19} cm^{-3}) $Si_{0.80}Ge_{0.20}$, after receiving 30 min anneals at 900°C. (9,200X)

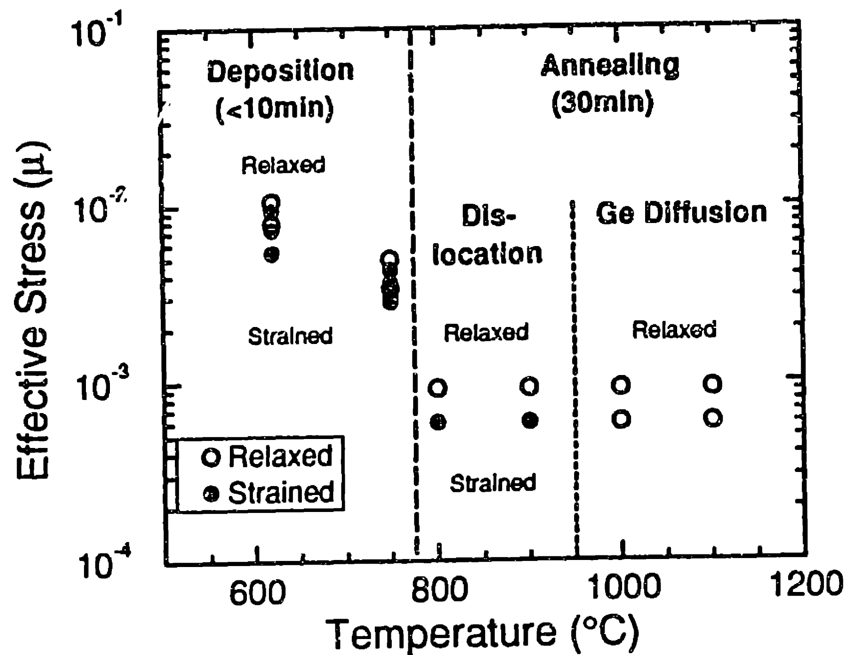

Figure 7.18: Thermal budget for the deposition and annealing of VLPCVD $Si_{1-x}Ge_x$ layers.

7.5 Therm-l Budget for VLPCVD $Si_{1-x}Ge_x$ Deposition and Annealing

The results of the as-grown and annealed $Si_{1-x}Ge_x$ layers exhibited in Fig. 7.2, Fig. 7.8, and Fig. 7.9 allow us to predict a safe thermal budget for deposition and annealing without introducing strain relaxation. We used the effective stress modified by Houghton, as shown in previous section, to estimate the stress within $Si_{1-x}Ge_x$ strained and relaxed layers. Figure 7.18 presents the range of effective stress in which we have seen strained and relaxed layers from the as-grown (temperature $\leq$ 750°C and time < 10 min) and annealed (temperature $\geq$ 750°C and time = 30 min) samples. Once the effective stress is kept below the boundary, $Si_{1-x}Ge_x$ layers are expected to remain strain. However, when the annealing temperature is too high, $Si_{1-x}Ge_x$ will relax by Ge diffusion though the layer may be

dislocation free.

7.6 Conclusion

In summary, we have measured the critical thickness of VLPCVd $Si_{1-x}Ge_x$ strained layers grown at 750 and 620°C. Layers grown at 620°C have greater critical thickness compared to that grown at 750°C. The dislocation density of in uncapped 1240Å-thick $Si_{0.92}Ge_{0.08}$ and 600Å-thick $Si_{0.87}Ge_{0.13}$ after receiving 30 min anneals at 750 – 950°C have been measured. It was found that misfit strain in these samples relieved very fast at 750 – 800°C and approached a saturated density at temperatures > 850°C, which did not lead to total relaxation, indicating a force balance existed between the driving force and the repulsive force of dislocations. Strain relaxation in annealed ~1400Å Si/520-700Å $Si_{1-x}Ge_x$/Si heterostructures (x=0.09 – 0.16) have been quantitatively measured and the corresponding misfit dislocation structures for x=0.13 and x=0.16 are discussed with respect to single-kink and double-kink dislocation mechanisms, which are characterized by the effective stress (τ_{eff}) for the propagation of single and paired misfit dislocations. A transition from partially relaxation to fully and excess relaxation is revealed by DCD. The two region of relaxation behaviors were investigated by the observation of misfit dislocations and the measurement of Ge diffusion. Our experimental observations and calculations indicate that in these Si/$Si_{1-x}Ge_x$/Si structures, the sluggish relaxation observed at T < 950°C is dominated by misfit dislocations, and the rapid relaxation at T > 950°C is associated with Si-Ge interdiffusion. We also studied the effect of B dopant on the thermal stability of $Si_{1-x}Ge_x$ and found that the heavily B-doped films appeared to be more stable.

Lastly, a thermal budget for the deposition (temperature $\leq$ 750°C and time < 10 min) and annealing (temperature $\geq$ 750°C and time = 30 min) of VLPCVD $Si_{1-x}Ge_x$ strained layers has been mapped out based on the calculations of effective

stresses for both strained and relaxed layers.

Chapter 8

Summary and Suggestions

8.1 Summary

This thesis has examined the deposition limitations and developed a procedure for growing $Si_{1-x}Ge_x$ strained layers using a VLPVCVD reactor. The deposition kinetics of undoped and *in situ* doped $Si_{1-x}Ge_x$ has also been explored. In order to implement the VLPCVD films into device fabrication, the post-deposition properties of the as-grown $Si_{1-x}Ge_x$ strained layers have been studied. We investigated strain relaxation, which involves defect generation and Ge diffusion, in $Si_{1-x}Ge_x$/Si and Si/$Si_{1-x}Ge_x$/Si structures, and proposed a process window for thermal treatment without degrading the layer quality.

The major results of this thesis work are summarized as follows:

8.1.1 Deposition of $Si_{1-x}Ge_x$

- High structural quality strained layers of $Si_{1-x}Ge_x$, both single layers and multiple layers, on Si were grown at 620 – 750°C with Ge contents up to 20%.

- The concentrations of oxygen and carbon were found to increase rapidly at T < 620 – 650°C at very low pressures, which severely degrade the film quality

and surface morphology.

- The range of Ge composition and temperature for smooth morphology has been mapped out for VLPCVD. The range of Ge for two-dimensional growth in VLPCVD is similar to that observed in molecular beam epitaxy at temperatures $\geq 620°C$. At temperatures $< 620°C$, the Ge range for two-dimensional growth appears smaller, probably due to serious carbon and oxygen contamination which accelerate three-dimension nucleation.

- The critical thickness of $Si_{1-x}Ge_x$ layers grown by VLPCVD has been determined, which is temperature dependent and is similar to that by UHVCVD and LRP at temperatures of 550 - 640°C.

- Selective growth of $Si_{0.86}Ge_{0.14}$ has been achieved with thickness up to 800$\AA$ at 675°C.

- $Si_{1-x}Ge_x$ layers grown on LOCOS patterned substrates were observed to have greater critical thickness than that grown on plasma-etching patterned substrates.

8.1.2 Growth Kinetics of $Si_{1-x}Ge_x$

- By comparing the results obtained from VLPCVD, UHVCVD, and LPCVD, we found that germanium incorporation is weakly dependent on deposition temperature and total deposition pressure using SiH_4 and GeH_4 at 550 - 750°C and at 1 - 100 mTorr.

- The incorporation of germanium was also found weakly dependent on the pressure of hydrogen carrier gas.

- At 620°C, the growth rate of $Si_{1-x}Ge_x$ was found independent of the size of epitaxial window at very low pressures.

- The growth rates of $Si_{1-x}Ge_x$ show different dependencies on germanium at different temperatures between 570°C and 750°C; the growth rate increases with the increase of Ge contents at 570°C, but decreases as germanium content increases at 700 and 750°C. At intermediate temperatures, a peak in growth rate was observed.

- The activation energy of $Si_{1-x}Ge_x$ growth rate is decreased by the increase of germanium content, suggesting that the growth kinetics is modified by germanium incorporation.

- The observed peak in $Si_{1-x}Ge_x$ growth rate was dependent on the total deposition pressure. The peak shifts to higher germanium contents as the the total deposition pressure is raised. This helps to explain the reported discrepancies of $Si_{1-x}Ge_x$ growth behaviors using different reactors which are operated at different pressures.

- Consistent with the ideas proposed by Meyerson et al. e[27] and Robbins et al. [36], our experimental data and more detailed kinetic model also suggests that the growth rate of $Si_{1-x}Ge_x$ is limited by H_2 desorption at low Ge and low T, but is dominated by the decreased sticking probabilities of SiH_4 and GeH_4 at high germanium and high temperature.

- For a given GeH_4/SiH_4 gas ratio, we observed that the amount of incorporated germanium atoms was decreased by increasing plasma power, but the growth rate was enhanced by plasma excitement.

8.1.3 In-Situ Doping of $Si_{1-x}Ge_x$

- Very high boron (2×10^{20} cm^{-3}) and arsenic (5×10^{19} cm^{-3}) concentrations have been achieved in $Si_{0.87}Ge_{0.13}$ using 1000 ppm diborane and arsine without degrading film quality.

- Boron concentration increases linearly with B_2H_6 and the amount of incorporated B atoms is independent of germanium content.
- Arsenic incorporation for n-type doping is saturated at 5×10^{19} cm^{-3} for AsH_3 concentrations in excess of 50 ppm.
- The saturation of phosphorus dopant concentration was not observed with PH_3 gas-phase fraction up to 100 ppm, and the amount of incorporated phosphorus atoms was found enhanced by germanium.
- A dramatic improvement of phosphorus dopant profile was observed by the addition of germanium.
- The measured $Si_{1-x}Ge_x$ growth rate is unaffected by the addition of B_2H_6, but is degraded by AsH_3 and PH_3 incorporation.
- Germanium was observed to reduce the degradation of $Si_{1-x}Ge_x$ growth rate due to arsenic and phosphorus doping.
- The observation of enhanced phosphorus dopant profile and $Si_{1-x}Ge_x$ growth rate due to germanium addition is speculated as a result of reduced surface passivation of phosphorus. A simple model, which is consistent with the measured data, has been proposed to explain the germanium enhanced doping process.

8.1.4 Thermal Stability of $Si_{1-x}Ge_x$

- 1240Å $Si_{0.92}Ge_{0.08}$/Si and 600Å $Si_{0.87}Ge_{0.13}$/Si strained layers were found to relax after 30min annealing at $T \geq 750°C$, and the dislocation density becomes saturated at $T \geq 850$ –900°C.
- It is found that strain in ~1400Å Si/520-700Å $Si_{1-x}Ge_x$/Si structures with Ge contents of 0.09 – 0.16 relax gradually at temperatures < 950°C but

relax rapidly at temperatures > 950°C. Possible relaxation mechanisms, involving misfit dislocation generation as well as germanium diffusion, have been examined and quantitatively compared with the measured strain.

- By examining dislocation generation and Ge diffusion, we determined that the strain relaxation in 520-700Å $Si_{1-x}Ge_x$ (x=0.09-0.16) is caused by misfit dislocations at T < 950°C and by Ge diffusion at T > 950°C.

- Boron doped $Si_{1-x}Ge_x$ strained layers were found more stable than undoped layers.

- A thermal budget for $Si_{1-x}Ge_x$ deposition and annealing without strain relaxation has been proposed.

8.2 Suggestions

Several proposals are given in this section for future studies:

8.2.1 Deposition of $Si_{1-x}Ge_x$

A problem we have encountered in growing $Si_{1-x}Ge_x$ using our VLPCVD reactor is the accuracy of germane flow rate. Because a mass flow controller for the flow range of 0 – 10 sccm was installed for germane whose optimum flow rate is 0 – 1.25 sccm, experimental errors are unavoidable. Although the mass flow controller is calibrated on a year basis and the measured variation of germanium is found to be within an acceptable range, i.e., ± 1.5%, a mass flow controller for narrower range is recommended for more precise process control.

Another concern related to deposition is the accuracy of temperature which affects the deposition rate. Yearly calibration shows that the errors of wafer temperature within ±5°C and is acceptable. To provide a DC bias for plasma cleaning and to improve the temperature uniformity across the wafer, a SiC coated graphite

susceptor is used to support the wafer, that unfortunately increase the time for the wafer to cool from 775°C (cleaning temperature) to the desired lower deposition temperature, and surface recontamination resulted. Therefore, a thinner susceptor with higher thermal mass is suggested.

In this work we have mapped out a range for two-dimensional growth under the normal deposition conditions. In addition to the factors of temperature and germanium which have already been explored, the growth rate of $Si_{1-x}Ge_x$ also plays an important role in the surface morphology by affecting the growth kinetics and impurity contamination. Since the $Si_{1-x}Ge_x$ growth rate is functions of both germanium content and temperature, to fix the growth rate at different temperatures and germanium contents appears difficult. However, at our most interested temperatures, for example, 620 and 675°C, it might be worthy to do more experiments to examine how $Si_{1-x}Ge_x$ flow rate affects the transition of two- and three-dimensional growth.

Besides growth rate, a more complicated effect on the growth mode comes from plasma-enhanced deposition. Since plasma-enhanced deposition causes serious coating in the chamber walls and requires frequent tube change, due to the limit of reactor user time, only few runs have been performed in this work. It can be expected that the enhancement of growth rate by plasma should have similar effects on surface morphology as the increase of flow rate; however, the increased mobility of reactive species on surface and the impingement of ion flux on the three-dimensional clusters may have significant impact on the deposition behavior. Though tube changing is time consuming and is a torture, I believe there will be a lot gains behind the pains.

8.2.2 Growth Kinetics of $Si_{1-x}Ge_x$

In this work, the deposition pressure dependency of $Si_{1-x}Ge_x$ growth rate has been studied and the obtained data has been used for examining the growth kinetics.

Though the measured data supports the speculation that hydrogen desorption is the rate-limiting step at low germanium and low temperature, and, when it is enhanced and becomes unimportant by increasing germanium, the growth rate is limited by the reduced reaction probabilities, the effect of hydrogen pressure on growth rate is still clear. Because of the limitation of hydrogen flow rates (0 – 150 sccm), the attempt in this research to understand whether hydrogen desorption is critical at low germanium and low temperature and not important at high germanium and high temperature is not very successful. To clarify the role of hydrogen, a much wider range of hydrogen flow is required to see significant variation in $Si_{1-x}Ge_x$ growth rate. Therefore, a new mass flow controller is recommended. Furthermore, the increase of hydrogen flow rate may also allow to increase the incubation time of both polycrystalline $Si_{1-x}Ge_x$ and silicon on oxide and the maximum thickness of selective epitaxial layers.

8.2.3 In-Situ Doping of $Si_{1-x}Ge_x$

Although we have observed that germanium served to reduce the residual doping of phosphorus and greatly improve the dopant profile, similar studies were not performed for As doping of $Si_{1-x}Ge_x$ and Si. Even similar effects are expected, it would be interesting to compare the interaction of germanium and phosphorus and that of germanium and arsenic to determine which dopant source is more controllable. Furthermore, since the residual doping of arsenic or phosphorus is not totally removed, as suggested by the degraded growth rate of silicon cap layer, strategies should be developed to reduce the residual doping for more flexible device design. Perhaps, increasing the purge time between two successive depositions or employing plasma to sputter/remove the sticking dopant gas in the chamber before next deposition will help.

8.2.4 Thermal Stability of $Si_{1-x}Ge_x$

There are many parameters associated with the thermal stability of $Si_{1-x}Ge_x$ strained layers, such as germanium composition and profiles, $Si_{1-x}Ge_x$ thickness, number of $Si_{1-x}Ge_x$ and Si layers, pattern of epitaxial layers, background contamination, annealing temperature and time, and annealing ambient. The studies performed here are just few of possible cases and we tried to explore the general cases which yield useful information for our device fabrication. Focusing on $Si/Si_{1-x}Ge_x/Si$ heterostructures for our npn $Si_{1-x}Ge_x$-base HBTs, the most important issue to be studied is the rapid thermal annealing of $Si_{1-x}Ge_x$, because of its importance in minimizing thermal budget which is not only crucial to the strain relaxation of $Si_{1-x}Ge_x$ but also to the diffusion of boron dopant. The rapid heating and cooling rates may lead to unwanted thermal stress and enhance strain relaxation. Thus, the study of defect generation and strain relaxation due to rapid thermal annealing is suggested.

The effect of boron dopant on the thermal stability of p-$Si_{1-x}Ge_x$ is another interesting topic to study, especially for highly doped $Si_{1-x}Ge_x$ base. Our preliminary results suggests that boron dopant improves the stability of $Si_{1-x}Ge_x$, but the detailed mechanisms is still unclear. Also, it would be interesting to look into the impact of ion implantation on the strain relaxation of $Si_{1-x}Ge_x$, the implantation may introduce defects and enhance the relaxation. Furthermore, the outdiffusion of boron-doped base is also an important problem in device fabrication. Though it has been suggested that germanium retards the diffusion of boron, the data concerning boron diffusion in $Si_{1-x}Ge_x$ is not widely reported. It is therefore of practical interest to measure the boron diffusivity as functions of temperature and germanium contents.

Since the thermal stability of $Si_{1-x}Ge_x$ strained layer also depends on window size, to have a thermal budget directly related to our device fabrication, the

investigation of strain relaxation in windows with the dimensions similar to that of active device area is also suggested.

Bibliography

[1] S.M. Sze ed., VLSI Technology, McGraw-Hill, New York (1988).

[2] S. Wolf and R.N. Tauber, Silicon Processing for the VLSI Era, Vol 1, Lattice Press, CA (1986).

[3] S.M. Sze, Physics of Semiconductor Devices, 2nd ed., Wiely, New York (1981).

[4] J.C. Bean, Physics Today, October, 36 (1986).

[5] J.C. Bean, Science, October, 127 (1985).

[6] S.S. Iyer, G.L. Patton, J.M.C. Stork, B.S. Meyerson, and D.L. Harame, IEEE Transactions on Electron Devices, **36**, 2043 (1989) and references therein.

[7] R. People, IEEE J. Quantum Electronics, **QE-22**, 1696 (1986).

[8] E. Kasper, in Heterostructures on Silicon : One Step Further with Silicon, NATO series, Kluwer Academic Publishers, The Netherlands (1989).

[9] R. Kern, G. Le Lay, and J.J. Metois, in Current Topics in Material Science, Vol **3**, North Holland, Amsterdam (1979).

[10] J.A. Venables, G.D.T. Spillers, and M. Hanbucken, Rep. Prog. Phys. **47**, 399 (1984).

[11] E. Bauer and J.H. van der Merwe, Phys. Rev. **B33**, 3657 (1986).

[12] M. Wortis, in Fundamental Problems in Statistical Mechanics, Vol **6**, North Holland, Amsterdam (1985).

[13] J.C. Bean, L.C. Feldman, A.T. Fiory, S. Nakahara, and I.K. Robinson, J. Vac. Sci. Tech. **A2**, 436 (1984).

[14] J.C. Bean, T.T Sheng, L.C. Feldman, A.T. Fiory, and R.T. Lynch, Appl. Phys. Lett. **44**, 102 (1984).

[15] A.G. Cullis and G.R. Booker, J. Crystal Growth, **19**, 132 (1972).

[16] F.C. Frank, J.H. van der Merwe, Proc. Roy. Soc. London Ser. A. **198**, 205 (1949).

[17] F.C. Frank, J.H. van der Merwe, Proc. Roy. Soc. London Ser. A. **198**, 216 (1949).

[18] J.H. van der Merwe, J. Appl. Phys. **34**, 123 (1963).

[19] J.W. Matthews, S. Mader, and T.B. Light, J. Appl. Phys. **41**, 3800 (1970).

[20] J.W. Matthews and A.E. Blakeslee, J. Crystal Growth, **27**, 118 (1974).

[21] J.W. Matthews, J. Vac. Sci. Tech. **12**, 126 (1975).

[22] E. Kasper, H. J. Herzog, and H. Kibbel, Appl. Phys. **8**, 199 (1975).

[23] M.M. Manasevit, I.S. Gergis, and A.B. Jones, Appl. Phys. Lett. **41**, 464 (1982).

[24] A.T. Fiory, J.C. Bean, L.C. Feldman, and I.K. Robinson, J. Appl. Phys. **56**, 1227 (1984).

[25] R. People and J.C. Bean, Appl. Phys. Lett. **47**, 322 (1985).

[26] C.M. Gronet, C.A. King, W. Opyd, J.F. Gibbons, S.D. Wilson, and R. Hull, J. Appl. Phys. 61, 2407 (1987).

[27] B.S. Meyerson, K.J. Uram, and F.K. LeGoues, Appl. Phys. Letter. **53**, 2555 (1988).

[28] T. Karasawa, K. Fujinaga, and I. Kawashima, Extended Abstracts of the 21st Conference on Solid State Devices and Materials, Tokyo, 377 (1989).

[29] P.M. Garone, J.C. Sturm, P.V. Schwartz, S.A. Schwartz, and B.J. Wilkens, Appl. Phys. Lett. **56**, 1275 (1990).

[30] M. Racanelli and D.W. Greve, Appl. Phys. Lett. **56**, 2524 (1990).

[31] K.H. Jung, Y.M. Kim, and D.L. Kwong, Appl. Phys. Lett. **56**, 1775 (1990).

[32] P.D. Agnello and T.D. Sedgwick, Topical Symposium on Silicon Based Heterostructure, Tronto, Canada, 46 (1990).

[33] Y. Zhong, M.C. Ozturk, D.T. Grider, J.J. Wortman, and M.A. Littlejohn, Appl. Phys. Lett. **57**, 2092 (1990).

[34] F. Namavar, J.M. Manke, E.P. Kvam, M.M. Sanfacon, C.H. Perry, and N.M. Kalkhoran, Mat. Res. Soc. Symp. Proc. **220**, 285 (1991).

[35] M.L. Green, B.E. Weir, D. Brasen, Y.F. Hsieh, G. Higashi, A. Feygenson, L.C. Feldman, and R.L. Headrick, J. Appl. Phys. **69**, 745 (1991).

[36] D.J. Robbins, J.L. Glasper, A.G. Cullis, and W.Y. Leong, J. Appl. Phys. **69**, 3729 (1991).

[37] W.B. de Boer and D.J. Meyer, Appl. Phys. Lett. **58**, 1286 (1991).

[38] T.I. Kamins and D.J. Meyer, Appl. Phys. Lett. **59**, 178 (1991).

[39] J.F. Gibbons, C.M. Gronet, and K.E. Williams, Appl. Phys. Lett. **47**, 721 (1985).

[40] P.K. Tedrow, V. Ilderem, and R. Reif, Appl. Phys. Lett. **46**, 189 (1985).

[41] R. Reif and C.G. Fonstad, U.S. Patent No. 4 659 401.

[42] M.L. Green, D. Brasen, H. Luftman, and V.C. Kanan, J. Appl. Phys. **65**, 2558 (1989).

[43] B.S. Meyerson, Appl. Phys. Lett. **48**, 797 (1986).

[44] ASM Epitaxy, Phoenix, AZ.

[45] P.D. Agnello, T.O. Sedgwick, M.S. Goorsky, J. Ott, T.S. Kuan, and G. Scilla, Appl. Phys. Lett. **59**, 1479 (1991).

[46] J.L. Hoyt, C.A. King, D.B. Nobel, C.M. Gronet, J.F. Gibbons, M.P. Scott, S.S. Laderman, S.J. Rossner, K. Nauka, J. Turner, and T.I. Kamins, Thin Solid Films **184**, 93 (1990).

[47] A.T. Fiory, J.C. Bean, R. Hull, and S. Nakahara, Phys. Rev. **B31**, 4063 (1985).

[48] F.K. LeGoues, S.S. Iyer, K.N. Tu, and S.L. Delage, Mat. Res. Soc. Symp. Proc. Vol **103**, 185 (1987).

[49] Y. Fukuda, Y. Kohama, M. Seki, and Y. Ohmachi, Japnese J. Appl. Phys. **27**, 1593 (1988).

[50] R.J. Hauenstein, B.M. Clemens, R.H. Miles, O.J. Marsh, E.T. Croke, and T.C. McGill, J. Vac. Sic. Technol. **B7**, 767 (1989).

[51] C.G. Tuppen and C.J. Gibbings, Thin Solid Films, **183**, 133 (1989).

[52] D.D. Perovic, G.C. Weatherly, J.M. Baribeau, and D.C. Houghton, Thin Solid Films, **183**, 141 (1989).

[53] C.G. Tuppen and C.J. Gibbings, J. Appl. Phys. **68**, 1526 (1990).

[54] D.C. Houghton, D.D. Perovic, J.M. Baribeau, and G.C. Weatherly, J. Appl. Phys. **67**, 1850 (1990).

[55] D.C. Houghton, Appl. Phys. Lett. **57**, 1434 (1990).

[56] R. Hull and J.C. Bean, J. Vac. Sci. Technol. **A7**, 2580 (1989).

[57] R. Hull and J.C. Bean, Appl. Phys. Lett. **54**, 925 (1989).

[58] R. Hull, J.C. Bean, and C. Buescher, J. Appl. Phys. **66**, 5837 (1989).

[59] B.W. Dodson and J.Y. Tsao, Appl. Phys. Lett. **53**, 2498 (1988).

[60] B.W. Dodson, Appl. Phys. Lett. **53**, 394 (1988).

[61] H. Kroemer, Proc. IRE **45**, 1535 (1957).

[62] H. Kroemer, Proc. IEEE **70**, 13 (1982).

[63] H. Barber, Can. J. Phys. **63**, 683 (1985).

[64] 6.771 Lectures, EECS, MIT (1991).

[65] P.M. Asbeck, IEDM Tech. Dig., **65** (1988).

[66] P. Asbeck, Proc. IEEE, **65** (1989).

[67] See reviews: A.Y. Cho and J.R. Authur, Prog. Solid State Chem. **10**, 157 (1975).

[68] See reviews: R.D. Dupuis, L.A. Moudy and P.D. Dapkus, Inst. Phys. Conf. ser. **45**, 1 (1979).

[69] T. Ishibashi et al., IEDM Tech. Dig., 826 (1988)

[70] M. Takahashi, M. Tabe, and Y. Sakakibara, IEEE Electron Device Lett., EDL-8, 475 (1987).

[71] T. Sugii et al., IEEE Electron Device Lett. **EDL-9**, 471 (1988).

[72] J. Symons et al., Solid-State Electronics **30**, 1143 (1987).

[73] H. Fujioka et al., IEDM Tech. Dig., 574 (1988)

[74] C. T. Sah, Proc. IEEE, **76**, 1280 (1988).

[75] T.P. Pearsall, CRC Critical Reviews in Solid-State and Materials Sciences, **15**, 551 (1989).

[76] R. People, J.C. Bean, D.V. Lang, A.M. Sergent, H.L. Stormer, K.W. Wecht, R.T. Lynch, and K. Baldwin, Appl. Phys. Lett. **45**, 1231 (1984).

[77] H. Jorke and H.J. Herzog, Proc. 1st Int. Symp. on Si MBE, J.C. Bean Ed. Electrochemical Soc., Pennington, N.J. (1985).

[78] J.H. Comfort, L.M. Garverick, and R. Reif, J. Appl. Phys. **62**, 3388 (1987).

[79] E. Kasper and H.J. Herzog, Thin Solid Films, **44**, 357 (1977).

[80] G.L. Patton, S.S. Iyer, S.L. Delage, S. Tiwari, and J.M.C. Stork, IEEE Electron Device Letters EDL-9, **165** (1988).

[81] T. Tatsumi, H. Hirayama, and N. Aizaki, Appl. Phys. Lett. **52**, 895 (1988).

[82] D.X Xu, G.D. Shen, M. Willander, W.X. Ni, and G.V. Hansson, Appl. Phys. Lett. **52**, 2239 (1988).

[83] H. Daembkes, H.-J. Herzog, J. Jorke, H. Kibbel, and E. Kasper, IEEE Trans. Electron Devices, **ED-33**, 633 (1986).

[84] H. Temkin, T.P. Pearsall, J.C. Bean, R.A. Logan, and S. Luryi, Appl. Phys. Lett. **48**, 963 (1986).

[85] C.A. King, J.L. Hoyt, C.M. Gronet, J.F. Gibbons, M.P. Scott, and J. Turner, IEEE Electron Device Lett. **EDL-10**, 52 (1989).

[86] G.L. Patton, D.L. Harame, J.M.C. Stork, B.S. Meyerson, G.L. Scilla, and E. Ganin, IEEE Electron Device Lett. **EDL-10**, 534 (1989).

[87] S. Suzuki and T. Itoh, J. Appl. Phys. **54**, 6385, (1983).

[88] J.H. Comfort and R. Reif, J. Electrochem. Soc. **136**, 2398 (1989).

[89] C. Tsai, S.M. Jang, J. Tsai, and R. Reif, J. Appl. Phys. **69**, 8158 (1991)

[90] J.L. Hoyt, C.A. King, D.B. Nobel, C.M. Gronet, J.F. Gibbons, M.P. Scott, S.S. Laderman, S.J. Rossner, K. Nauka, J. Turner, and T.I. Kamins, Thin Solid Films **184**, 93 (1990)

[91] L.M. Garverick, J.H. Comfort, T.R. Yew, and R. Reif, J. Appl. Phys. *62*, 3398 (1987).

[92] D.B. Noble, J.L.Hoyt, W.D. Nix, J.F. Gibbons, S.S. Laderman, J.E. Turner, and M.P. Scott, Appl. Phys. Lett. **58**, 1526 (1991).

[93] T.R. Yew and R. Reif, J. Appl. Phys. **68**, 4681 (1990).

[94] T.R. Yew and R. Reif, Appl. Phys. Lett. **55**, 1014 (1989).

[95] M. Racanelli and D.W. Greve, Appl. Phys. Lett. **58**, 2096 (1991).

[96] Y. Takahasi, H. Ishii, and K. Fujinaga, Appl. Phys. lett. **57**, 599 (1990).

[97] T.R. Yew and R. Reif, J. Appl. Phys. **65**, 2500 (1989).

[98] J. Murota, N. Nakamura, and N. Mikoshiba, Appl. Phys. Lett. **54**, 1007 (1989).

[99] A. Nishida, K. Nakagawa, E. Murakami, and M. Miyao, J. Appl. Phys. **71**, 5913 (1992).

[100] S.M. Jang, C. Tsai, and R. Reif, J. Electron. Mat. **20**, 91 (1991).

[101] S.M. Jang and R. Reif, Appl. Phys. Lett. **59**, 3162 (1991).

[102] S.M. Jang and R. Reif, Appl. Phys. Lett. **60**, 707 (1992).

[103] T.I. Kamins and D.J. Meyer, Appl. Phys. Lett. **61**, 90 (1992).

[104] J.H. Comfort and R. Reif, J. Electrochem. Soc. **136**, 2386 (1989).

[105] T.R. Yew, MIT PhD Thesis (1990).

[106] S.M. Gates, C.M. Greenlief, S.K. Kulkarni, and H.H. Sawin, J. Vac. Sci. Technol. **A8**, 2965 (1990).

[107] P. Gupta, V.L. Colvin, S.M. George, Physical Review B, **37**, 8234 (1988).

[108] K. Sinniah, M.G. Sherman, L.B. Lewis, W.H. Weinberg, J.T. Yates, Jr., and K.C. Janda, Physical Review Letters, **62**, 567 (1989).

[109] M.A. Morris, M. Bowker, and D.A. King, in Kinetics of Adsorption, Desorption and Diffusion at Metal Surfaces, Comprehensive Chemical Kinetics, Vol. 19, Elsevier, Amsterdam (1984).

[110] B.M.H. Ning and J.E. Crowell, Appl. Phys. Lett. **60**, 2914 (1992).

[111] M. Racanelli and D.W. Greve, J. Vac. Sci. Technol. **B9**, 2017 (1991).

[112] D.W. Greve and M. Racanelli, J. Electrochem. Soc. **138**, 1744 (1991).

[113] K.H. Jung, T.Y. Hsieh, D.L. Kwong, H.Y. Liu, and R. Brennan, Appl. Phys. Lett. **60**, 724 (1992).

[114] W.H. Liu, J.D. Leighton, and S.A. Campell, Appl. Phys. Lett. **61**, 1676 (1992).

[115] S.M. Jang, K. Liao, and R. Reif, submitted to Appl. Phys. Lett.

[116] S.M. Jang, H.W. Kim, and R. Reif, Appl. Phys. Lett. **61**, 315 (1992).

[117] J.H. Comfort and R. Reif, J. Appl. Phys. **65**, 1053 (1989).

[118] M.L. Yu, D.J. Vitkavage, and B.S. Meyerson, J. Appl. Phys. **59**, 4032 (1986).

[119] J.H. Comfort and R. Reif, J. Appl. Phys. **65**, 1071 (1989).

[120] L.J. Giling and J. Bloem, J. Crystal Growth, **31**, 317 (1975).

[121] G.L. Vick and K.M. Whittle, J. Electrochem. Soc. **116**, 1142 (1969).

[122] S.M. Gates, C.M. Greenlief, D.B. Beach, and P.A. Holbert, J. Chem. Phys. **92**, 3144 (1990).

[123] R.I.G. Uhrberg, R.D. Bringans, R.Z. Bachrach, and J.E. Northrup, J. Vac. Sci. Technol. A **4**, 1259 (1986).

[124] W.A. Jesser and D. Kuhlmann-Wilsdorf, Phys. Stat. Sol. **19**, 95 (1967).

[125] J.H. van der Merwe and C.A.B. Ball, in *Epitaxial Growth, Part B*, edited by J. W. Matthews (Academic, New York, 1975), pp. 560-610.

[126] J.W. Matthews, J. Vac. Sci. Technol. **12** 126 (1975).

[127] S.C. Jain and W. Hayes, Semicond. Sci. Tech. **6**, 547 (1991), and references therein for reviews.

[128] S.C. Jain, J.R. Willis, and R. Bullough, F.R.S., Advances in Physics, **39**, 127 (1990), and references therein for reviews.

[129] J.W. Matthews and A.E. Blakeslee, J. Crystal Growth, **29**, 273 (1975).

[130] E. Kasper, Surface Science, **174**, 630 (1986).

[131] E. Kasper, H. J. Herzog, H. Daembkes, and G. Abstreiter, Layered Structure and Epitaxy vol. 56, ed. J.M. Gibson et al., Materials Research Society, 347 (1986).

[132] G.L. Patton, J.H. Comfort, B.S. Meyerson, E.F. Crabbé, G.J. Scilla, E. de Frésart, J.M.C. Stork, J.Y.-C. Sun, and D.L. Harame, and J.N. Burghartz, IEEE Electron Device Lett. **11**, 171 (1990).

[133] R. Hull, J.C. Bean, D.J. Eaglesham, J.M. Bonar, and C. Buescher, Thin Solid Films **183**, 117 (1989).

[134] R. Hull, J.C. Bean, D. Bahnck, L.J. Peticolas, Jr. K. T. Short, and F.C. Unterwald, J. Appl. Phys. **70**, 2052 (1991).

[135] D.B. Noble, J.L. Hoyt, J.F. Gibbons, M.P. Scott, S.S. Laderman, S.J. Rosner, and T.I. Kamins, Appl. Phys. Lett. **55**, 1978 (1989).

[136] D.C. Houghton, C.J. Gibbings, C.G. Tuppen, M.H. Lyons, and M.A.G. Halliwell, Thin Solid Films **183**, 171 (1990).

[137] D.C. Houghton, J. Appl. Phys. **70**, 2136 (1991).

[138] C.G. Tuppen and C.J. Gibbings, J. Electron. Mater. **19**, 1101 (1990).

[139] G.F.A. van de Walle, L.J. Ijzendoorn, A.A. van Gorkum, R.A. van den Heuvel, A.M.L. Theunissen, and D.J. Gravesteijn, Thin Solid Films **183**, 183 (1990).

[140] S.R. Stiffler, J.H. Comfort, C.L. Stanis, D.L. Harame, E. de Fresart, and B.S. Meyerson, J. Appl. Phys. **70**, 1416 (1991).

[141] W. Hagen and H. Strunk, Appl. Phys. **17**, 85 (1978).

[142] P. Haasen, Acta. Met. **5**, 598 (1957).

[143] W.J. Byra, Solid State Commun. **12**, 253 (1973).

[144] M. Chandrasekharr, J.B. Renucci, and M. Cardona, Phys. Rev. B **17**, 1623 (1978).

[145] B.A. Fox and W.A. Jesser, J. Appl. Phys. **68**, 2801 (1990).

Appendix A Process Traveler of LOCOS Patterned Wafers

:07 1992 trav.tex Page 1

PROCESS TRAVELER of LOCOS Patterned Wafers &Revision 1.0

LOT ID : jang01
LOT OWNER : Syun-Ming Jang

Start Date: End Date:
Layer Growth Date: Layer Growth completed:

STEP #	STEP DESCRIPTION	STATUS
0	Starting material Ziti Incorporated, Prime, 1/18/91 Cust PO# GGR166148 <100> 100mm, Phos, 1-10 ohm-cm	Number wafers: 50
1	Stress Relief Oxide dsro430.set	Number wafers ______ Opset start ______ Opset finish ______
2	LPCVD Silicon Nitride dnit1.5k.set	Number wafers ______ Opset start ______ Opset finish ______
3	Locos Pattern phlocos.set	Number wafers ______ Opset start ______ Opset finish ______
4	Nitride Plasma Etch Front plnit1.5k.set	Number wafers ______ Opset start ______ Opset finish ______
5	Resist Ash ash.set	Number wafers ______ Opset start ______ Opset finish ______
6	Field Oxidation dfield5.1k.set	Number wafers ______ Opset start ______ Opset finish ______
7	Nitride Wet Etch wnit1.5k.set	Number wafers ______ Opset start ______ Opset finish ______

Appendix B Process Traveler of Plasma-Etched Patterned Wafers

PROCESS TRAVELER of Plasma-Etched Patterned Wafers &Revision 1.0

LOT ID : jang02
LOT OWNER : Hyun-Ming Jang

Start Date: End Date:
Layer Growth Date: Layer Growth completed:

STEP #	STEP DESCRIPTION	STATUS
0	Starting material <100> 100mm, Phos, 1-10 ohm-cm	Number wafers: 50
1	Field Oxidation dfield5.1k.set	Number wafers ______ Opset start ______ Opset finish ______
2	Field Oxide Pattern phfield.set	Number wafers ______ Opset start ______ Opset finish ______
3	Plasma Etch ploxide5.1k.set	Number wafers ______ Opset start ______ Opset finish ______
4	Resist Ash ash.set	Number wafers ______ Opset start ______ Opset finish ______
5	Gate Oxidation dgate220.set	Number wafers ______ Opset start ______ Opset finish ______
6	RCA clean (TRL)	Number wafers ______ Opset start ______ Opset finish ______
7	Strip Gate Oxide (TRL) stripox220.set	Number wafers ______ Opset start ______ Opset finish ______
8	Si and SiGe Growth (TRL) vlpcvd.set	Number wafers ______ Opset start ______ Opset finish ______
9	Wafer scribe scribew.set (2cm x 2cm)	Number wafers ______ Opset start ______ Opset finish ______
10	RCA clean (TRL) square samples (2cmx2cm) with special sample holder	Number wafers ______ Opset start ______ Opset finish ______
11	Furnace Anneals (TRL) anneal.set	Number wafers ______ Opset start ______ Opset finish ______